

SAPIENZA UNIVERSITÀ DI ROMA

DIPARTIMENTO DI FISICA

PHD THESIS

Measurement of the Bhabha scattering cross section at the PADME Experiment

Author:
Elizabeth LONG
Matricola: 1891962

Supervisor:
Prof. Mauro RAGGI

External supervisor:
Dott. Tommaso SPADARO

4th September 2023



Acknowledgements

I would like to thank several groups of people, without whose help this work would never have been possible.

Firstly, I want to thank my supervisor Mauro Raggi, who took a chance on me when he'd only known me for a few months. I am extremely grateful to have had the opportunity to do my PhD here, and with this wonderful group of people, and none of that would have been possible if Mauro had not had faith in me at the very beginning. Mauro's continued support through the whole process has been extremely important, and I'm very appreciative of all of the opportunities he has given me, encouraging me to go to conferences and schools and to present in informal and formal settings.

I would also like to thank Tommaso Spadaro, whose contributions to my analysis, and whose patience with my unending questions, were vital to the success of the measurement in this thesis. I've learned a huge amount from you, and I'm so grateful for all of the time that you've given me through the analysis process.

A huge vote of thanks must also go to the PADME collaboration in all its forms through these years. Paola Gianotti helped me with so much of the bureaucracy that has accompanied my PhD, and I am so grateful to her for that. Venelin Kozhuharov gave me my first start in PADME. I will never forget how you found the scholarship for me, translated all of my application documents for me, and took me all around Sofia to complete all of the bureaucratic processes I had to do. Emanuele Leonardi's help with the software was also very much appreciated, and Paolo Valente's support with missions and other INFN things was invaluable.

I'm also extremely grateful to the "Giovini Scienziati" who gave me so much of their time so graciously when I was new. Clara, you're an inspiration to me. You've been extremely kind and a very good friend to me and I will always remember your generosity - giving me cake to take home to my parents, keeping my plants alive for me, helping me with the Target reconstruction and with software problems, and encouraging me when the going got tough. Isabella, you helped me practice my talk for the SIF about 100 times over and were nothing but encouraging and supportive. Fede O, you spent a lot of time passing on your knowledge about the Target and trying to help us solve the reconstruction problems. You also helped me greatly understanding the Vetos, and have been a good friend to me over the 4+ years I've known you. Fede G, you were a great office mate and very helpful in explaining theory concepts to me. Gabriele, your support in the template for the neural network studies was fundamental. You also gave me so much of your time helping with programming problems when I was starting out, and have been generally of great moral support. This group of people is the main reason I stayed in PADME to do my PhD. You gave me so much time without ever making me feel like I was a burden. I hope some day I'll be able to pay that favour forward with the same grace and kindness.

Thanks to the other seminar organisers: Beatrice, Elena, Giovanni, Giuseppe, Graziella, Julia, Loris, Lucas, Michele and Stefano. I think the project saved my mental health during my PhD, but it was only possible because of our teamwork. Thank you for continuing in the group despite my pushiness! Equally, thank you to all of our seminar regulars. Without an audience the project would never have got off the ground.

Thank you to the members of the Gender Balance Working Group: Caja, Claudia, Elena, Giulia, Lorenzo, Karolina, Matteo and Sabina. Thank you for creating a space for activism and for learning. Elisa can't not be mentioned here, thank you to her for, well, everything. Both the seminars and the GBWG owe so much to the groundwork that you'd already done in this department. The department misses you and will be happy to see you back some day!

Thank you to my closest physics friends in Rome: Elena, Lorenzo, Rafa, Rodrigo and Viri. You all belong to at least one other category already listed, but your support stopped me from going mad with the frustrations of academic life in Rome. Elena, you're someone I can and do talk to about everything. You've been so welcoming to me and I'm so grateful for our friendship (and your food recommendations!) Lorenzo, you're someone I can always count on to listen without judging me. You always just seem to understand and you're always up for anything. Rafa, thank you for listening to me during my PhD submission process and encouraging me to press the final "submit" button. I always enjoy sharing a beer with you and discussing how confusing Italy is! Rodrigo, hanging out with you is always a fun time, whether it's in the presence of turtles or watching films extremely silently. Maybe one day I'll even be able to communicate with your mum... Viri, you're an incredibly strong, independent woman and I have so much respect for you. You're also incredibly fun to be around, and you always know the right supportive comment to give at the right time.

Thank you to my closest friends in the U.K.: Alice, Becky, Charlotte, Chloe, George and Sam. Knowing that you were still there for me and I could still pick up where I left off with you, even when we didn't see each other for a year or more, makes being in a foreign country seem a bit less far away. Alice, being able to swap stories about living abroad has made me feel less isolated when things have been difficult. Becky, you're one of the most supportive people in the world and I always know I can go to you when I need a compliment for making a popular culture reference. Charlotte, I would never have been able to get through Uni without you, meaning I would never have got here. You've always been very supportive to me and I'm so grateful that when I text you it's always as if no time has passed. Chloe, I'm glad we've got closer over the last couple of years, your adventurous spirit is something I admire greatly. George, I'm so happy to have one friend who's actually interested in what I do! Thank you for being someone I can talk to about both work and life, while also enjoying good food and a good time! Sam, you've also been a wonderful friend to me ever since we first met at Uni. Thank you for always making time for me when I'm back in the UK, I always appreciate how easy it is to catch up with you when we get together.

Lastly but not leastly, thank you to the goats, the bears, the crabs, the snakes and all of the other various members of both noddle and menagerie. Your unwavering support and confidence in me have made the biggest difference to who I am today of any interactions I've ever had. Special mentions go to Dad, who got me into this mess and then continued to get me out, Mum who's always been of moral and practical support sorting anything I needed in the UK and always sending me tea when I've needed it, Pix for supporting when I needed a sister and fellow young researcher to vent to, and Joel for always being on my side. I love you all more than I can say, and I'm so incredibly grateful for all of your support.

Contents

1	Dark matter and the dark sector	2
1.1	Historical evidence of dark matter	2
1.2	Modern evidence for dark matter	5
1.2.1	Gravitational lensing	5
1.2.2	Cosmic microwave background	5
1.3	WIMP models	6
1.4	ALP models and constraints	7
1.5	Dark sector models and constraints	9
1.6	Protophobic models: ATOMKI anomaly and the X17	12
2	Bhabha Scattering in the Standard Model	13
2.1	Comparison of Geant4 physics libraries	15
2.2	Cross section calculations at next-to-leading-order	15
2.3	Bhabha scattering in the literature	16
2.3.1	Low energy measurements	16
2.3.2	Measurements at PADME energy scales	17
2.4	Measurements at higher energies	18
3	The PADME Experiment	20
3.1	Experimental Hall and Beam Setup	20
3.2	The PADME Detector	23
3.2.1	Active diamond Target	23
3.2.2	Electromagnetic calorimeter	25
3.2.3	Small Angle Calorimeter	26
3.2.4	The PADME dipole magnet	26
3.2.5	Charged Particle Vetoes	28
3.2.6	Timepix based Beam Monitor	29
3.2.7	Charged Particle Tagger	30
3.3	Trigger and Data Acquisition	31
3.4	Data Taking at the PADME Experiment	31
3.4.1	Data-Taking Run 1	32
3.4.2	Data-taking Run 2	33
3.4.3	Run 3: X17-dedicated data-taking run	35
3.4.4	Online Monitoring System	35
4	Charged Particle Detector Reconstruction	37
4.1	Overview of the PADME veto detectors	38
4.2	Hit Reconstruction	39
4.2.1	Signal processing	40
4.2.2	TSpectrum hit finding	41
4.2.3	Gain Equalisation	42
4.2.4	Tail correction	45
4.2.5	Time synchronisation	47
4.2.6	Validating the calibration	52

4.3	Cluster Reconstruction	52
4.4	Bremsstrahlung reconstruction	53
5	Neural network based veto reconstruction	56
5.1	Signal simulation: Toy MC signals	58
5.2	Signal simulation: Data-averaged signals	60
5.3	Multi-hit reconstruction using a convolutional neural network	61
5.4	Standard signals	62
5.5	Signals with 5ns rise time	63
5.6	Signals with 10ns rise time	64
5.7	Signals with amplitude fixed at 50mV	65
5.8	Model trained on signals with mean 5 hits per event	65
5.8.1	Signals with mean 5 hits per event	65
5.8.2	Signals with mean 3 hits per event	66
5.9	Model trained on signals with uniformly distributed hits per event	67
5.9.1	Signals with uniformly distributed hits per event	67
5.9.2	Signals with mean 5 hits per event	67
5.9.3	Signals with mean 3 hits per event	68
5.10	Signals with exponential rise time	69
5.11	Uncalibrated signal sample	69
5.12	Model trained on signals from data-averaged signals	70
5.12.1	Signals from mix of templates	70
5.12.2	Signals from Channel 0 Template	71
5.12.3	Signals from Channel 1 Template	72
5.12.4	Signals from Channel 2 Template	72
5.13	Conclusion	73
6	Bhabha scattering in PADME Run 2	74
6.1	Topology of Bhabha scattering at PADME	74
6.1.1	S-Channel Bhabha Scattering	76
6.1.2	T-Channel Bhabha Scattering	78
6.1.3	Combined S- and T-Channel	81
6.2	Pile-up and Veto occupancy rates	84
6.3	Bhabha time of flight correction	86
6.4	NPoT and Data Quality	92
6.5	Backgrounds at PADME	95
6.5.1	Photon annihilation background	95
6.5.2	Beam background	95
6.5.3	Bremsstrahlung background	97
6.6	Background subtraction	100
6.7	Results and cross checks	103
6.8	Cross-section calculation	105
6.9	Systematic uncertainties	105
7	Dark sector interpretations of Bhabha scattering	108
8	Conclusion	111

Introduction

Speculation around the distribution and velocities of massive bodies in the Universe dates back as far as the late 19th century. In 1884, Lord Kelvin wrote in a lecture to Johns Hopkins University: “Many of our supposed thousand million stars, perhaps a great majority of them, may be dark bodies”. He reached this conclusion after the discussion of a star known as “1830 Groombridge”, the velocity of which was considered anomalously high [1, p. 274]. Interest in stellar velocities and their relationships to cosmic mass distributions continued throughout the last century, and they still intrigue scientists to this day. Importantly, however, evidence exists at many different scales for the presence of a new type of matter which doesn’t interact through any of the four known forces, except gravity. This range of sources of evidence reinforces the problem and gives enhanced credibility to Dark Matter being the solution.

Detailed astronomical observations have led to the Standard Model of Cosmology, in which dark matter makes up 27% of the energy content and 85% of the matter content of the Universe. The fact that such a large fraction of the contents of our Universe is still unaccounted for reflects the difficulty of studying a type of matter which, if it exists, interacts only extremely weakly with Standard Model particles. One explanation for the weakness of the interactions is that dark matter exists in a secluded “Dark Sector”, which only interacts with the Standard Model through a new interaction mediated by a new particle. This class of theories are known as “Dark Sector” theories, and the mediator particle would provide a “portal” to interactions between Standard Model and Dark Sector particles. The mediator particle can have different quantum numbers depending on the structure of the theory in question, however, in a certain class of theories in which the portal interaction has a U(1) structure, the mediator particle can undergo kinetic mixing with the Standard Model photon. This theoretical connection between Dark Sector and Standard Model particles gives rise to the name “Dark Photon” for the portal particle.

This is the hypothesis that the PADME experiment was designed to test, exploiting the unique positron beam conditions found at the Beam Test Facility at the Laboratori Nazionali di Frascati. An introduction to the Dark Matter Problem can be found in Section 1.1, and the Dark Sector as a solution to the problem is discussed in Section 1.5.

If a Dark Photon (A') exists it must satisfy one of two conditions: either it has mass greater than or equal to twice the electron mass, or it doesn’t. If it is massive enough and if it can be produced at PADME in positron-electron annihilation events then, assuming time-reversal symmetry, it must decay to a positron-electron pair. The full reaction would therefore be, at first order:

$$e^+e^- \rightarrow A' \rightarrow e^+e^-$$

It can be seen here that the initial and final states are identical to those found in Bhabha scattering. For this reason, this thesis is a study of Bhabha scattering at the PADME experiment, with a view to interpreting these results as a potential limit on new physics.

The thesis starts with an introduction to Dark Matter (Chapter 1), then introduces Bhabha scattering in the Standard Model (Chapter 2). It then goes into detail about the experimental setup and the PADME detector (Chapter 3) and the reconstruction of the physical quantities of particles entering the detectors (Chapter 4) and presents a study on how machine learning tools could be used to improve this reconstruction (Chapter 5). Finally, the analysis strategy for Bhabha scattering is presented (Chapter 6), and a preliminary interpretation of a result compatible with the Standard Model within 5% as an exclusion limit on new physics is presented (Chapter 7).

Chapter 1

Dark matter and the dark sector

The nature of the physical phenomenon known as “dark matter” is one of the biggest unsolved questions in modern physics. This chapter will give an overview of the historical evidence for dark matter and how observed cosmological phenomena led to the hypothesis of a new type of matter in the Universe. Other, more recent, sources of evidence for dark matter will then be presented before moving on to a discussion of models in which dark matter is made up of previously undetected particles.

1.1 Historical evidence of dark matter

According to Newton’s law of gravitation, an object travelling in a stable circular orbit at distance r from the centre of the orbit must travel at speed $v(r)$ such that:

$$v(r) = \sqrt{\frac{GM(r)}{r}} \quad (1.1)$$

Where G is the gravitational constant and $M(r)$ is the integrated mass of everything between the centre of the orbit and the orbiting object in question. For stars at the edges of galaxies, and for galaxies at the edges of galaxy clusters, the mass of objects inside their orbit is mostly concentrated within some radius $R < r$, meaning that $M(r)$ can be approximated well by $M(r) \approx M(R) \approx \text{const.}$ In this way, Equation (1.1) reduces to:

$$v(r) \sim \frac{\text{const.}}{\sqrt{r}} \quad (1.2)$$

or, converting to angular velocity:

$$\omega(r) \sim \frac{\text{const.}}{r\sqrt{r}} \quad (1.3)$$

In Fritz Zwicky’s 1930s studies of the Coma cluster of galaxies (then called “nebulae”), he reported that “the masses of such systems, for a given distribution of average angular velocities throughout the system, are highly indeterminate, and vice versa” [2]. This inaccurate mapping between observed mass and rotational velocity of gravitational systems led to Zwicky suggesting that it was the mass measurements which were imperfect and proposing new mass-measurement techniques to try to resolve the problem. One of the proposed techniques was gravitational lensing, a process which is still used as evidence for the existence of dark matter, discussed in more detail in Section 1.2.1. In 1939 Horace Babcock built on Zwicky’s work, producing the first “galaxy rotation curve”. Figure 1.1 shows that the angular velocity of stars in the Andromeda galaxy tends to plateau as the distance from the centre of the galaxy increases [3], instead of decreasing monotonically as expected.

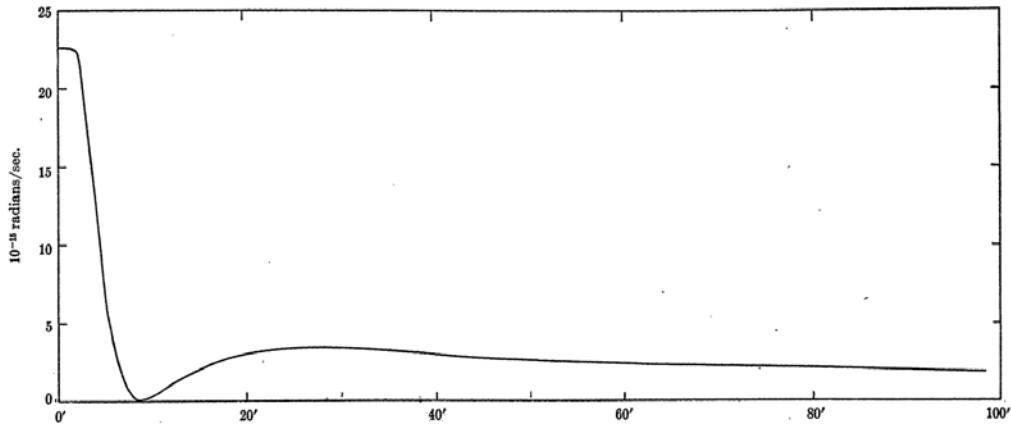


Figure 1.1: Angular velocity in the Andromeda galaxy in units of 10^{-15} radians per second (y-axis), as a function of radius from centre of galaxy in arc minutes (x-axis) [3].

In the 1970s, Vera Rubin and W. Kent Ford performed similar measurements on galaxies including Andromeda [4], publishing an influential paper in 1980 with detailed measurements of the rotation curves of several different galaxies [5]. The results from this paper, shown in Figure 1.2, found a similar effect, with star velocities plateauing instead of falling monotonically as the stars get further from the centre of the galaxy.

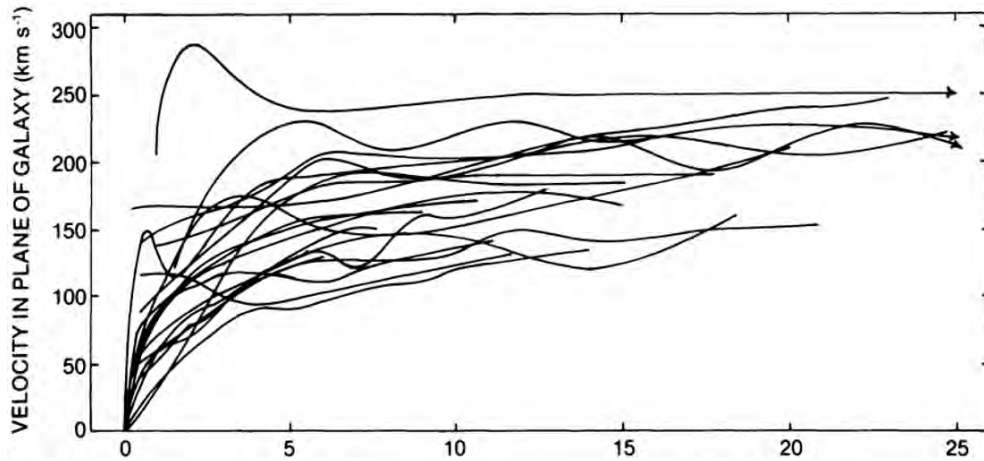


Figure 1.2: Rotation curves showing velocity of stars in galaxy in kms^{-1} (y-axis) as a function of their distance from the galactic nucleus, measured in kpc (x-axis), for 21 galaxies considered in Rubin and Ford's 1980 paper [5].

Analogous studies undertaken in radio astronomy of the Andromeda galaxy had already found agreement with optical data which was beginning to demonstrate tension between observation and classical Newtonian/Keplerian dynamics [6]. Studies using radio telescopes continued in the 1970s, providing a significant body of evidence by 1980 that the mass distribution of galaxies measured from the distribution of stars did not match the rotational curves, both in the optical and the radio spectrum. Important figures from papers in the 1970s can be seen in Figures 1.3 and 1.4, which all confirm the same anomaly [7, 8].

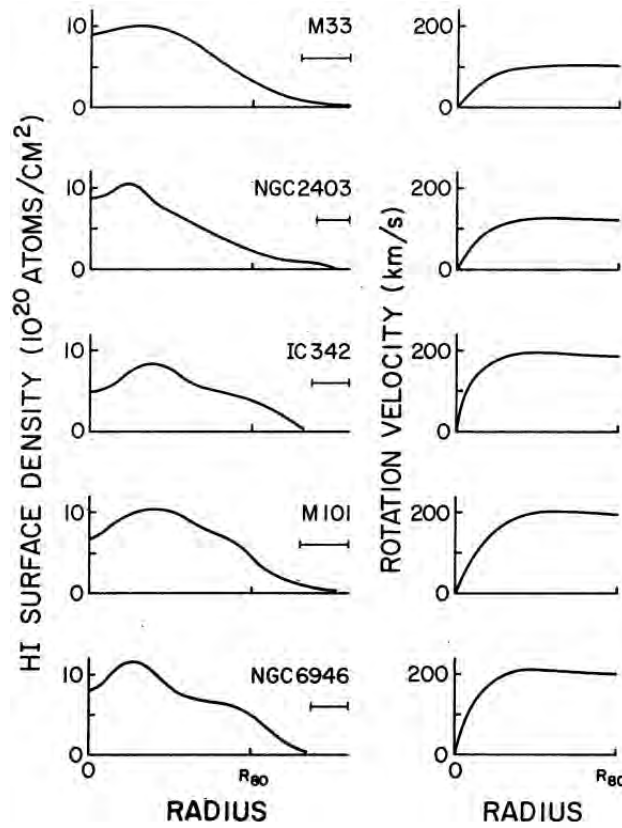


Figure 1.3: Rotation curves from radio telescope measurements of different galaxies, shown next to the distribution of masses in each galaxy. The bars under the galaxy names show average radial beam diameters, the spatial resolution of the measurements. R_{80} is the radius within which 80% of the observed mass is found [7].

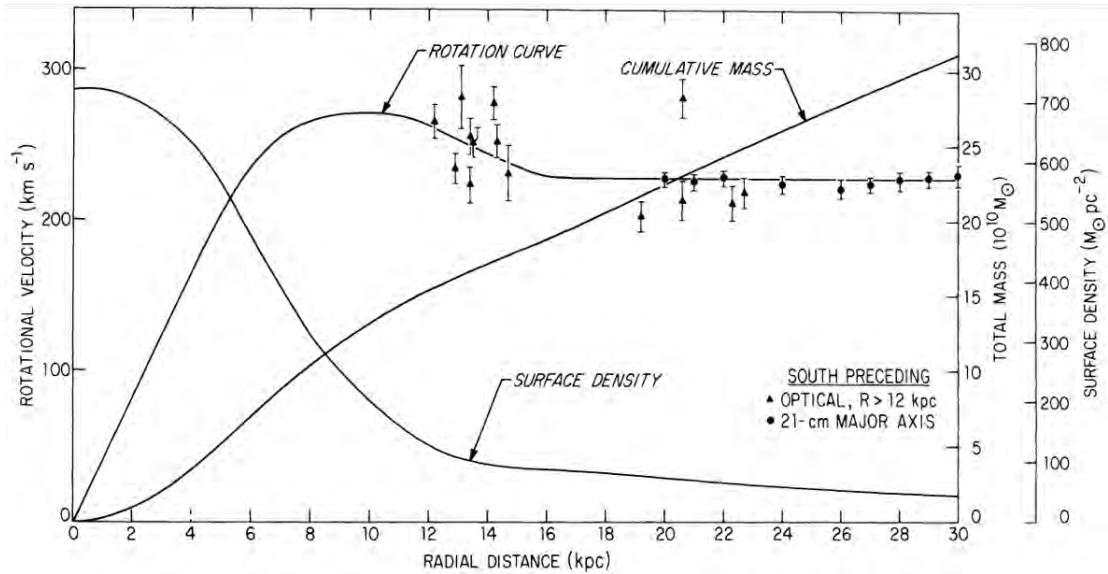


Figure 1.4: Rotation curve of M31 galaxy from Roberts and Whitehurst's radio telescope measurements and Rubin and Ford's optical measurements, shown together with the mass distribution within the galaxy, indicated by "surface density" [8].

1.2 Modern evidence for dark matter

In more recent times, progress in astronomical observation has allowed new evidence for dark matter to be collected from sources other than rotation curves. Some of these sources of evidence are presented here.

1.2.1 Gravitational lensing

General relativity predicts that gravitational fields have an effect on the motion not only of objects with mass, but also of anything which has momentum, including light. This means that very massive objects can act as lenses, bending light passing them. The more massive the object, the more the path of the light passing it is deflected, allowing measurements of the “lensing” effect to be used to study the mass distribution of objects in the Universe.

An excellent summary of gravitation lensing measurements as they relate to dark matter is given in [9], which cites the famous example of the Bullet Cluster as evidence of dark matter. The Bullet Cluster is in fact two different clusters which collided approximately 150 million years ago. In the collision, the galaxies in the two clusters largely continued along their original trajectories since the sparse spatial distribution of the galaxies in the clusters means that the probability of them interacting, their “self-interaction cross section”, is low. The opposite is true for the intracluster dust, shown in pink in Figure 1.5, which is much more uniformly spread throughout the clusters, and therefore has a very high self-interaction cross section. The result is that the gas largely stayed close to the point of interaction of the two clusters. Lensing data of the light from the clusters shows that most of the mass is located 8σ away from the peaks of the gas distributions, and that there is approximately 30-40 times the amount of total mass in the clusters than observed in the galaxies’ stars [9]. This teaches us not only that the stellar matter is not enough to make up the gravitational mass observed in these clusters, but also that any dark matter that exists must interact very weakly with itself.

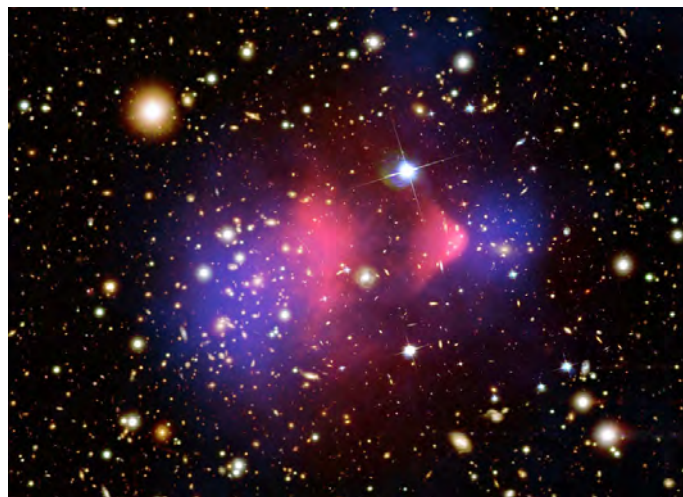


Figure 1.5: The Bullet Cluster, showing X-Ray observations of the gas distribution in pink [10] and lensing data of the mass distribution in purple [11], together with optical images of galaxies in the cluster.

1.2.2 Cosmic microwave background

The cosmic microwave background (CMB) is an almost perfect blackbody spectrum of radiation left over from the period known as “recombination”, when electrons and protons combined to form hydrogen atoms, thus making space transparent to radiation. According to the current Lambda Cold Dark Matter (LCDM) model of cosmology, the existence of stars and galaxies is due to the small anisotropies created in the Universe by weak ripples in the distribution of dark

matter which provided a scaffold upon which other types of mass could congregate. These anisotropies can still be seen in the CMB angular power spectrum. The relative height of the peaks in the angular spectrum shown in Figure 1.6 gives us information about the relative abundance of normal “baryonic” matter compared to dark matter [12].

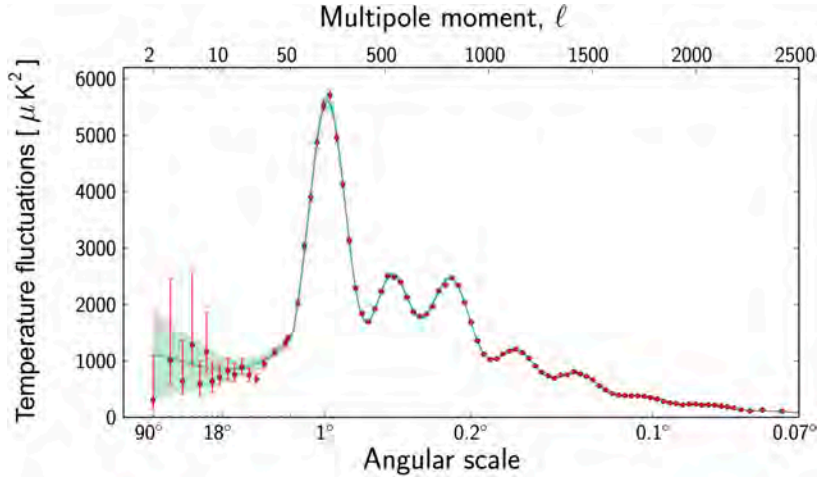


Figure 1.6: Angular power spectrum of the CMB, as measured by the Planck satellite[13].

1.3 WIMP models

One dark matter model which has received a lot of attention from the physics community since the 1980s is based on the idea of Weakly Interacting Massive Particles (WIMPs). These particles would have relatively large masses, usually within the 10 GeV-10 TeV range, and would only interact through gravity and potentially new forces with strengths equivalent to or weaker than the weak nuclear force.

Different techniques can be employed to search for these particles. Indirect detection experiments look for the Standard Model products of WIMP interactions. If WIMPs annihilate or decay into Standard Model particles, they could create an excess of gamma rays or cosmic rays. This type of signal is currently being searched for by telescopes such as VERITAS, MAGIC, Fermi, and H.E.S.S [14–17].

Direct detection experiments for WIMPs look for the interaction of these particles with atomic nuclei. Experiments mostly fall into one of the following categories:

- Cryogenic crystal detectors: experiments such as CDMS, CRESST, CoGeNT, MINER and EDELWEISS search for vibrations in cryogenically cooled crystals due to the interaction of a WIMP with an atomic nucleus [18–22];
- Noble liquid detectors: experiments like XENON, LZ, DEAP and DARKSIDE search for scintillation light in noble liquid detectors, produced when an atom passes through the target material after having gained kinetic energy in an interaction with a WIMP [23–26];
- Crystal scintillators: experiments such as DAMA/LIBRA, ANAIS and IceCube operate on a similar principle to the noble liquid detectors, using solid scintillators in the place of liquid scintillators [27–29].

Collider experiments such as those at the LHC may be sensitive to WIMPs produced directly in collisions between Standard Model particles. The experimental signature of WIMPs at colliders depends strongly on the specific model being considered, but, as discussed in [30], can broadly be classified as:

- Searches with dark matter in the final state;

- Searches without dark matter in the final state

In the first case, a common experimental signature is a so-called “monojet”, where one highly energetic jet is observed leaving the interaction point, potentially in combination with up to two other, less energetic, jets while the missing momentum is carried away in the opposite direction by the dark matter particle.

In the second, searches can focus on distortions in the di-jet invariant mass spectrum and/or in angular correlations between the two jets.

The WIMP hypothesis has attracted a lot of attention in the community over the last 3 decades, and the parameter space available to such models has been very well constrained. Figure 1.7 shows the situation as of 2022, as described in detail in [31]. The lack of observation of WIMPs to date has led to searches being widened and to other theories gaining attention.

1.4 ALP models and constraints

The axion is a hypothetical fundamental particle first proposed as a solution to the “strong CP problem”: although the mechanism by which CP symmetry is broken in the weak sector may be applied to the strong sector, no strong CP violation has been found. In 1977, Roberto Peccei and Helen Quinn suggested a solution to this problem which would add a new, spontaneously broken universal symmetry [32, 33]. In turn, the broken universal symmetry would imply the existence of a new particle [34, 35], which was originally hypothesised to have a very small mass strictly related to its coupling [36].

The theory has since been extended to include other, “axion-like” particles (ALPs), which could be more massive, making them more natural contenders for dark matter [37]. Constraints on the mass and coupling strength of ALPs candidates are shown in Figure 1.8. It should be noted that the mass range available to PADME, up to $O(10^{-2})$ GeV, still includes some uncovered parameter space.

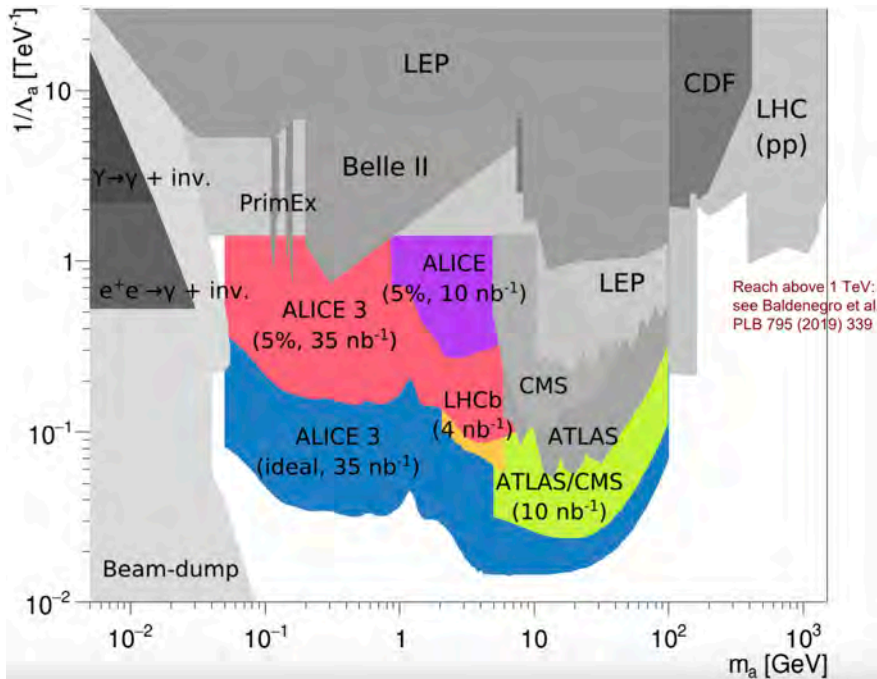
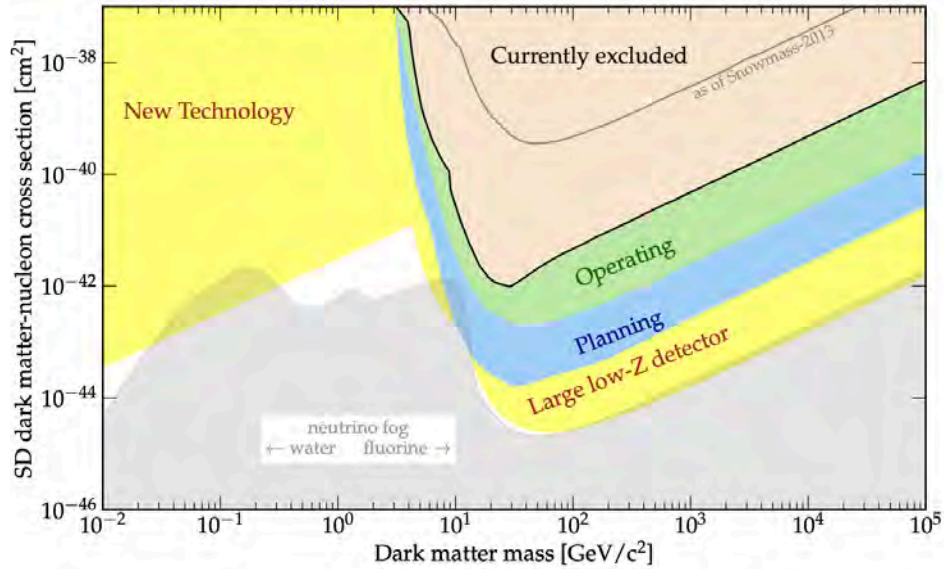
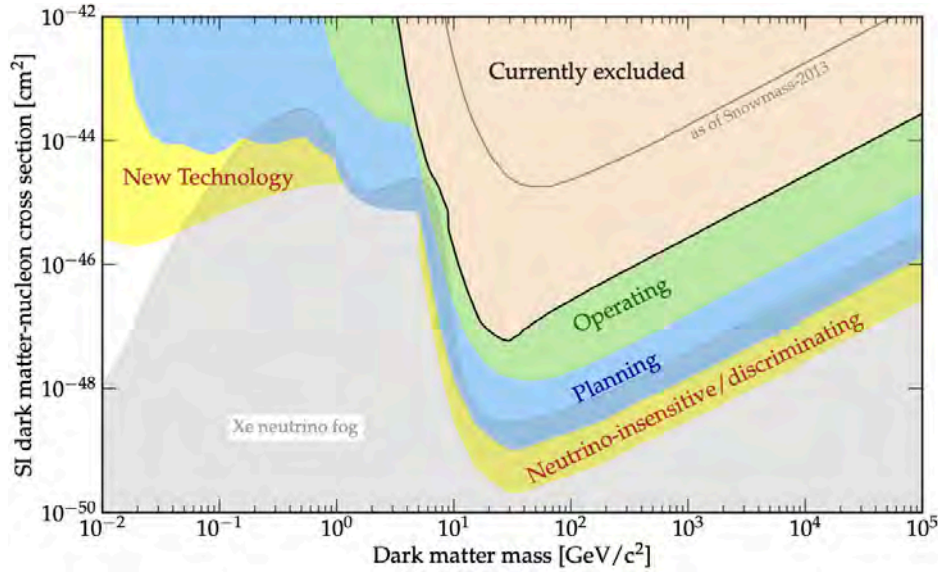


Figure 1.8: ALP parameter space constraints [38]



(a) “Combined Spin-independent dark-matter nucleon scattering cross section space. Current 90% c.l. constraints are shaded beige, while the reach of currently operating experiments are shown in green (LZ, XENONnT, PandaX-4T, SuperCDMS SNOLAB, SBC). Future experiments are shown in blue (SuperCDMS, DarkSide-20k, DarkSide-LowMass, SBC, XLZD, ARGO) and yellow (Snowball and Planned $\times 5$). The neutrino fog for a xenon target is shaded light grey” cit. [31].



(b) “Combined Spin-independent dark-matter nucleon scattering cross section space for scattering with neutrons or protons. Current 90% c.l. constraints are shaded beige, whereas the reach of currently operating experiments are shown in green (LZ, XENONnT). Future experiments are shown in blue (PICO500, XLZD) and yellow (Snowball, PICO-100 ton). The neutrino fog for a water or fluorine target is shaded light grey” cit. [31]

Figure 1.7: Exclusion limits on spin-dependent and spin-independent searches for WIMPs of [31]

1.5 Dark sector models and constraints

While the PADME experiment has sensitivity to certain ALP models, the nominal model which PADME was designed to investigate is that in which dark matter exists in a “dark sector”, which could contain one or more dark matter particles. This dark sector of particles could then interact with Standard Model particles by exchanging a mediator particle. This idea is illustrated schematically in Figure 1.9

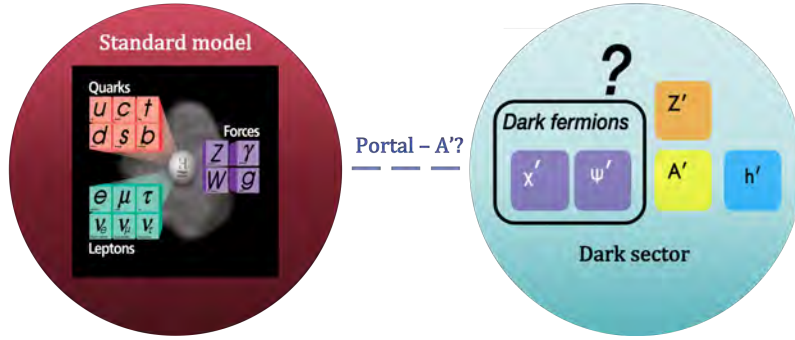


Figure 1.9: Schematic representation of dark sector models.

Dark sector models are based only on the minimal assumptions that dark matter exists and that it interacts with Standard Model particles through the exchange of a mediator particle which mixes kinetically with the Standard Model photon (Figure 1.10). This allows searches to be performed for the mediator in a relatively model-independent way, in contrast to many WIMP searches which rely on increasingly complex models to evade the increasingly constrained region of parameter space.

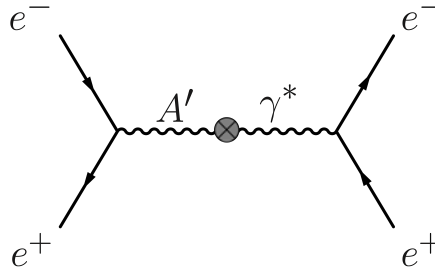


Figure 1.10: Kinetic mixing between Standard Model photon and dark photon

PADME was designed to search for a dark photon, known as A' , in associated production from e^+e^- annihilation events (Figure 1.11c). This model predicts a new vector portal particle connecting the realms of the Standard Model and the dark sector, which would couple to Standard Model fermions through the following Lagrangian:

$$\mathcal{L} = g' q_f \bar{\psi}_f \gamma^\mu \psi_f A'_\mu$$

where γ^μ are the Dirac γ matrices, A' is the effective dark photon current, $(\bar{\psi}_f)\psi_f$ is the (anti)fermion spinor, g' is the universal coupling constant of the new interaction and q_f are the charges of the fermions under this new interaction. The effective coupling ϵ of the dark photon to the fermion in question is given by $\epsilon = g' q_f$. In the basic model, $q_f = 1$, meaning that $\epsilon = g'$. This interaction comes about through the addition of a new U(1) symmetry to the standard model.

As will be discussed in more detail in Section 1.6, not all Standard Model particles need be charged under this new symmetry. Indeed, a portal particle could exist which had couplings to the u and d quarks balanced such that the coupling to the proton vanished. Such a particle

could provide an explanation for the observations of the so-called ‘‘X17’’ particle proposed to explain the recent anomalies found at the ATOMKI institute in Hungary. This type of particle is known as ‘‘protophobic’’. More information about the protophobic X17 particle can be found in Section 1.6.

The kinetic mixing with the Standard Model photon allows the dark photon to be produced in processes which produce a Standard Model photon, shown in Figure 1.11. Since this thesis is on the PADME experiment which uses a positron beam on a fixed target, the relevant diagrams are Figures 1.11b to 1.11d.

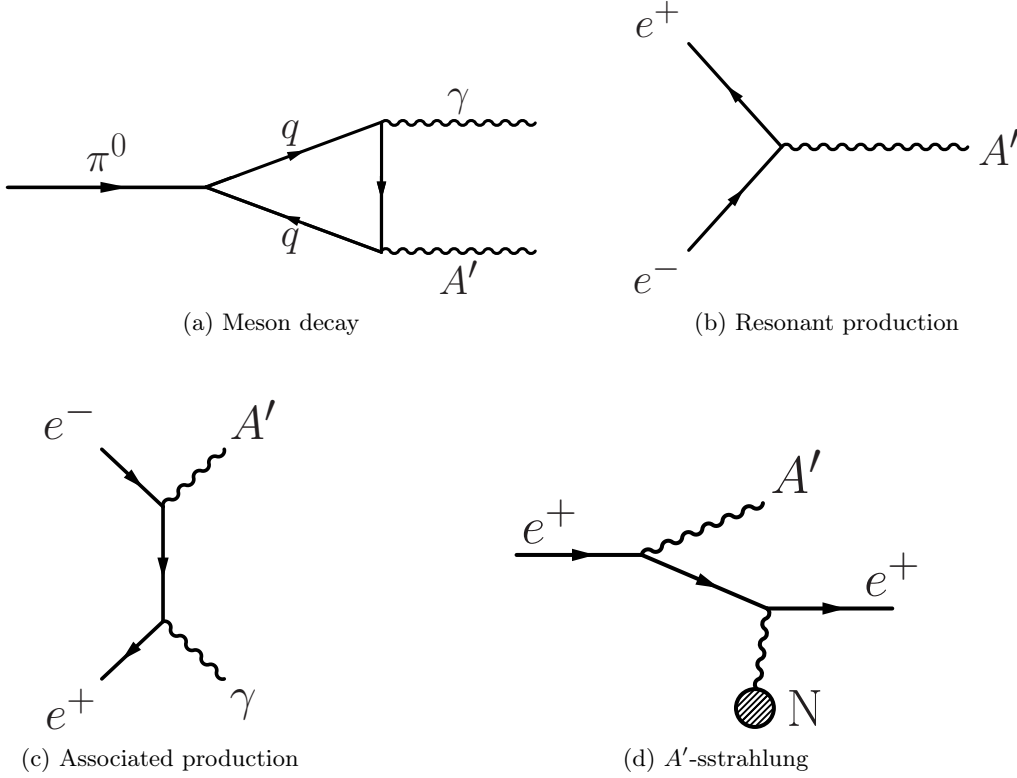


Figure 1.11: Production modes of the dark photon.

If the dark photon produced through kinetic mixing has mass $m_{A'} \geq 2m_e$, it can decay into Standard Model particles through kinetic mixing with the Standard Model photon. This is known as the ‘‘visible’’ decay paradigm and relies on the mass of the dark photon, $m_{A'}$ being at least twice the mass of the electron, the lightest Standard Model particle to couple to the Standard Model photon. If the dark photon mass is lower than this, and if dark sector fermions exist with less than half of the dark photon mass, then the dark photon will only decay ‘‘invisibly’’ into these dark sector particles. In the case where both are true, meaning that the dark photon has mass $m_{A'} \geq 2m_e$ and dark sector fermions in this mass range also exist, the dark photon will decay both visibly and invisibly, however the invisible decay rate would be much greater than the visible decay rate. This is summarised in Figure 1.12. Constraints on visible and invisible decays of the dark photon are shown in Figure 1.13a and Figure 1.13b respectively.

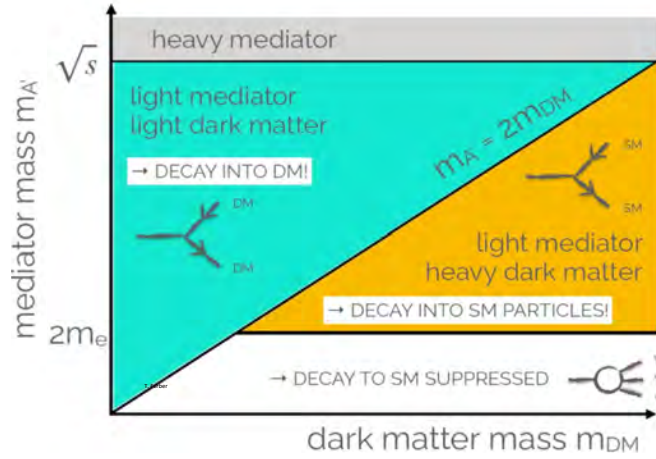
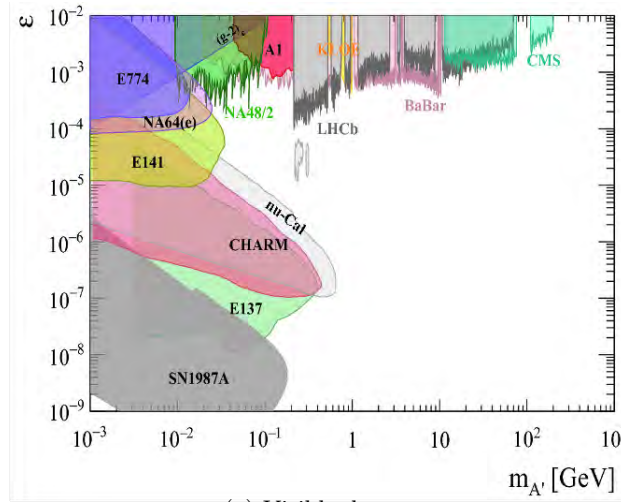
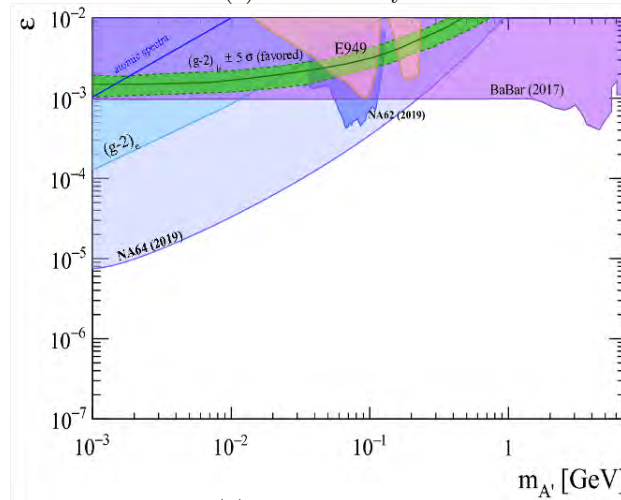


Figure 1.12: Kinematically permitted A' decay processes as a function of $m_{A'}$



(a) Visible decays



(b) Invisible decays

Figure 1.13: Constraints on visible (top) and invisible (bottom) dark photon decays. The x-axis shows the mass of the dark photon while the y-axis gives its mixing with the Standard Model photon, equivalent to its coupling to electrons [39]

1.6 Protophobic models: ATOMKI anomaly and the X17

In 2016, a collaboration from the ATOMKI institute in Debrecen, Hungary found a 6.8σ anomaly in the 18.15 MeV transition via internal pair conversion (IPC) of ^8Be , which was compatible with a new particle of mass $m_X c^2 = 17.03 \pm 0.11(\text{stat}) \pm 0.20(\text{syst})$ MeV [40].

After theoretical input from J. Feng et al. later that year [41], the ATOMKI team repeated the experiment with an improved setup, and reported an anomaly at the same invariant mass in the 17.6 MeV ^8Be decay [42]. Since then the collaboration have repeatedly confirmed the same anomaly at the same invariant mass in the decays of ^4He [43], excited using 3 different beam energies giving significances of 7.3σ , 6.6σ and 8.9σ respectively, and of ^{12}C at 4 different beam energies with significances ranging from 3σ to 8σ [44]. Following a suggestion from Zhang and Miller, the collaboration also found a signal of 4.5σ significance in off-resonance direct proton capture in the $^7\text{Li}(p, e^+e^-)^8\text{Be}$ reaction [45]. It is clear, therefore, that the signal observed by the ATOMKI collaboration is not a statistical fluctuation, and for this reason it has received significant interest from a wider scientific community, both theoretical and experimental. The present status, as of March 2023, of both experimental and theoretical studies of this phenomenon is summarised in [46].

Theoretical explanations of the effect have been proposed which introduce a new protophobic boson to explain the anomaly [41, 47–49]. In these models, the couplings of the new particle to up quarks and to down quarks cancel, in such a way as to make the theories consistent with both the ATOMKI observations and the lack of analogous observations at other experiments such as NA48/2, which performed a precise measurement of $\pi^0 \rightarrow \gamma e^+e^-$ decay [50].

Given that the signature has been observed in IPC, which results in an e^+e^- pair being emitted from an excited atomic nucleus, if the anomaly is due to the decay of a new particle, it must couple to e^+e^- . Assuming time reversal symmetry, if the particle exists it must be possible to produce it in e^+e^- annihilations and search for its decays in $e^+e^- \rightarrow e^+e^-$ events. Given that PADME was designed to produce e^+e^- annihilations and has detectors capable of detecting charged lepton final states, the experiment is a good environment to provide independent confirmation of a particle physics explanation of the anomaly, without the extra complexity and uncertainties introduced in nuclear physics experiments.

Since the experimental signature in this case would be identical to Standard Model Bhabha scattering, the work done in studying Bhabha scattering for this thesis was instrumental in defining the PADME strategy for its Run 3 search for this particle, known as the ‘‘X17’’. As explained in Chapter 8, the difficulties encountered in the analysis of PADME Run 2 data focussing on Bhabha scattering led to the improved experimental setup used in Run 3 to search specifically for the X17.

Chapter 2 gives a detailed overview of Bhabha scattering from a theoretical point of view.

Chapter 2

Bhabha Scattering in the Standard Model

In quantum electrodynamics (QED), e^+e^- scattering, known as Bhabha scattering, is a process where, at tree-level, a positron and an electron scatter off each other through the exchange of either a photon or a Z boson. It is important to note in discussing the theoretical expectations for, and interpretations of, this measurement, that PADME is a fixed target experiment with a positron beam impinging on a diamond target. The beam energy in the data used in this analysis was 430 MeV, giving a centre of mass energy \sqrt{s} of 21 MeV.

Since the \sqrt{s} at PADME is 4000 times lower than the mass of the Z, the scaling of the cross section with \sqrt{s} means that the contribution from Z-exchange is negligible in this context. For this reason, this discussion assumes that the only contributions to the Bhabha scattering cross section come from the exchange of a Standard Model photon. This assumption was validated using CalcHEP, a tool created to perform Feynman diagram calculations [51]. Including only the diagrams with contributions from the Z boson, a leading order cross section of $O(10^{-7})$ pb was obtained, compared with the cross section of the process mediated only by the Standard Model photon, obtained in the same way, which is of $O(10^{11})$ pb.

The tree-level diagrams of interest to PADME are the S-channel “annihilation” process seen in Figure 2.1a and the T-channel “scattering” process shown in Figure 2.1b, and their interference term, which is negative.

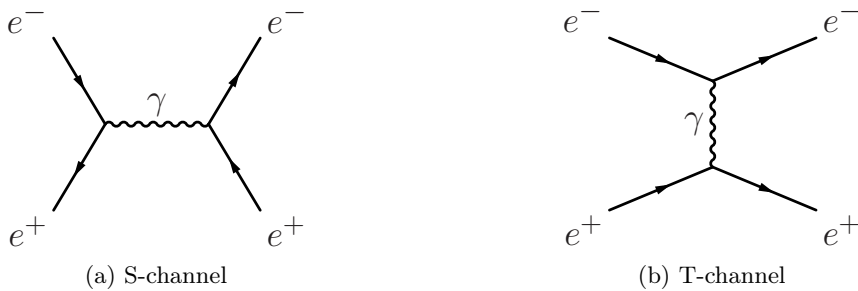


Figure 2.1: Tree level Feynman diagrams of Bhabha scattering processes at PADME energies

The leading order cross sections for the S-channel (σ_{SCh}) and the T-Channel (σ_{TCh}) are given in Equation (2.1) and Equation (2.2) respectively.

$$\sigma_{SCh} = \frac{4\pi\alpha^2}{3s^2} (s + 4m_e^2 + 4\frac{m_e^4}{s}) \quad (2.1)$$

$$\sigma_{TCh} = \frac{4\pi\alpha^2}{s} \left[\frac{1}{2} + \frac{1}{1 - \frac{4m_e^2}{s}} \ln \frac{1 - \cos \theta_R}{2} + \frac{\frac{s^2}{2} + 2m_e^4 - 2sm_e^2}{(\frac{s}{2} - 2m_e^2)^2} \left(\frac{1}{1 - \cos \theta_R} - \frac{1}{2} \right) \right] \quad (2.2)$$

Here, s is the square centre of mass energy, m_e is the electron mass, $\alpha = \frac{e^2}{m_e}$ is the fine structure constant, and θ_R is the scattering angle, that is the opening angle between the two outgoing particles in the lab frame.

The total cross section is dominated by the T-Channel process, while the S-channel cross section is orders of magnitude smaller. To get an estimate of the level of difference between the cross sections for these processes, CalcHEP was used to perform a tree-level calculation in both cases. To simulate the data from PADME Run 2 used in this thesis, the calculation was performed using a positron with incident energy 431.6 MeV and an electron at rest. The results from this calculation are, for the S-Channel:

$$\sigma_{SCh} = (1.97 \pm 0.01) \times 10^8 \text{ pb}$$

and for the T-Channel:

$$\sigma_{TCh} = (5.17 \pm 0.01) \times 10^{11} \text{ pb}$$

Errors here are statistical.

In the T-channel case, the tree-level scattering diagram exhibits infrared divergence at extremely low values of momentum-transfer. To obtain the value given above a cut was placed to give a minimum value of total energy for the final state electron of 1 MeV. Varying this cut it was seen that the value of the cross section obtained is very sensitive to the value of the cut; increasing the cut to 2 MeV produces a cross section value of $\sigma_{TCh} = (1.65 \pm 0.002) \times 10^{11}$ pb. Nevertheless, these numbers act as a useful guide to the expected relative production rates of the two processes in PADME Run 2.

The total cross section measured in nature also includes the interference term, which is negative. The cross section $\sigma_{CalcHEP}$ for the whole process including the interference term calculated using CalcHEP is:

$$\sigma_{CalcHEP} = (5.14 \pm 0.01) \times 10^{11} \text{ pb}$$

Any new massive boson which decays to e^+e^- will have a negligible contribution at energy scales significantly different from its mass. This means that the dominant contribution to new physics coming from decays of this type would have a kinematic profile identical to S-channel Bhabha scattering which, as can be seen in Figure 2.2, is significantly different from that of the T-channel.

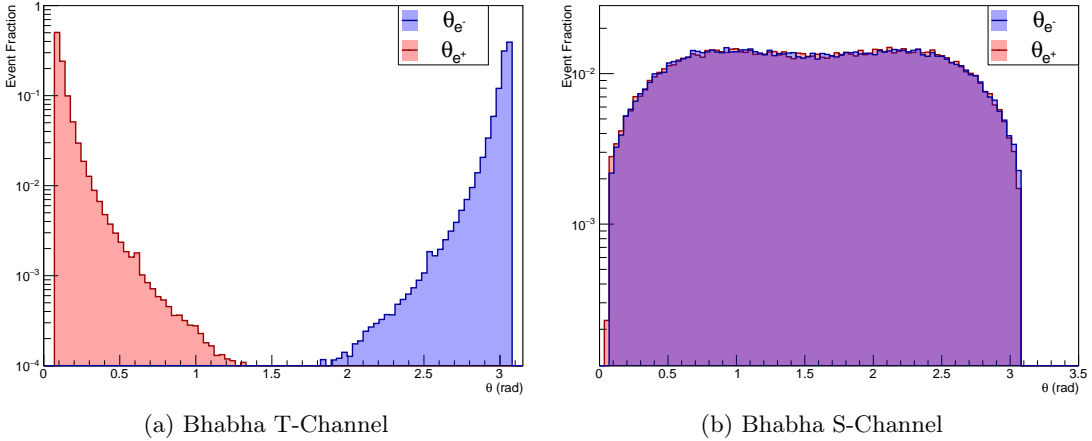


Figure 2.2: Theta: angle to beamline of final state particles beam in centre of mass frame for T-Channel and S-channel Bhabha scattering. The positron is shown in red, the electron in blue. Plots have been normalised to the total number of events simulated.

2.1 Comparison of Geant4 physics libraries

In Geant4, Bhabha scattering is implemented alongside all other ionisation processes in the G4eIonisation class [52]. The value of the cross section of these processes depends on the specific Geant4 physics lists being used.

Geant4 offers different models in its different physics libraries, which are optimised for different needs. The three compared in this analysis were the Standard Electromagnetic Libraries, the Livermore Libraries and the Penelope Libraries [53–55].

The Standard Electromagnetic Libraries provide a simple and computationally efficient calculation of the cross sections of electromagnetic processes. The Livermore Libraries are based on the Livermore physics models [56] and provide a comprehensive set of electromagnetic processes. The Penelope Libraries are based on the Penelope physics models, which are specifically designed for low-energy electromagnetic interactions.

The Penelope models have several advantages in simulating low energy processes. They take into account the atomic shell structure and electronic configuration of the target material allowing for a more realistic simulation of interactions involving specific atomic shells. The Geant4 models have been extensively validated against experimental data for a wide range of low-energy electromagnetic interactions demonstrating a satisfactory agreement at the level of $\sim 5\%$ [57].

The standard PADME Monte Carlo simulations use the Standard Physics Libraries since the computational efficiency was considered the most important feature, given that the simulation needed $\geq 10^{12}$ Positrons on Target (PoT).

Geant4 provides tools specifically to test different physics libraries. In the Extended Electromagnetic Library, "TestEm0" allows the user to print the value of cross section used by the library [58]. This value was extracted from each of the three libraries mentioned above, inserting diamond as the scattering target and introducing a minimal energy cut of 1 MeV for the final state positrons. Using a beam energy of 431.6 MeV, the cross section for Bhabha scattering was found to be identical in all three libraries. On further investigation it was found that the Penelope and Livermore Libraries do not calculate the value of the ionisation cross section but take it directly from the Standard Library. The only significant difference is that the Penelope and Livermore Libraries include Compton scattering, which is not present in the Standard Library, and in the Penelope Library the Bremsstrahlung cross section is 25% higher than the Standard Library. This is probably due to very low energy photons being simulated in the Penelope Library and not in the Standard Library.

This internal consistency gives no information about the true precision of the cross section used in these models. As far as has been established by the author at the time of writing, the calculation of the cross section in the Geant4 libraries is only tree-level. Checking the value given in Geant4 with that produced in CalcHEP it was found that for the same energy cut the cross section was compatible. Geant4 only accepts cuts in kinematic energy, not in total energy which is the case in CalcHEP. Converting a 1 MeV kinematic energy cut in Geant4 to a 1.511 MeV total energy cut in CalcHEP, the cross-sections obtained in these simulations are, from Geant4:

$$\sigma_{Geant4} = 2.47 \times 10^{11} \text{ pb}$$

and from CalcHEP:

$$\sigma_{CalcHEP} = (2.54 \pm 0.01) \times 10^{11} \text{ pb}$$

which agree to within 2.8%.

2.2 Cross section calculations at next-to-leading-order

Since Bhabha scattering implies the presence of charged particles in both the initial and the final state, inserting radiative corrections and next-to-leading-order diagrams into the calculation of the cross section is expected to have an effect on the final cross section of up to several percent. Moreover, radiation in the initial or final states of the process will change the kinematics of the

process and is likely to have a significant effect on the experimental acceptance of the PADME detector. At the time of writing, investigations are ongoing into the use of the BABAYAGA event generator to give a more precise value of the Bhabha scattering cross section and a sample of Monte Carlo events with a more accurate kinematic distribution [59].

2.3 Bhabha scattering in the literature

Bhabha scattering has often been used as a measure of luminosity in e^+e^- collider experiments. Experiments have often measured the number of Bhabha scattering events, using the theoretical cross section of the process to infer the total number of collisions that had taken place [60–63], or else performed measurements comparing the rates of wide-angle and small-angle Bhabha scattering processes in order to probe the internal structure of the electron [64].

An excellent summary of Bhabha scattering and its experimental measurement, as of 1991, can be found in [65]. As is also discussed in that review, the review of the literature performed for this thesis found very few published studies at centre of mass energies $< O(1)$ GeV, and even fewer which provide a direct measurement of the Bhabha scattering cross section.

The literature review presented in this thesis discusses some important historical measurements of Bhabha scattering, from $O(1)$ MeV energies to $O(10)$ GeV energies.

2.3.1 Low energy measurements

The first measurement discussed here was published in 1953 and was intended to validate the e^+e^- scattering cross section formula developed by Bhabha around 20 years earlier [66]. The authors particularly wanted to check that the annihilation term in Bhabha’s formula was accurate, which would imply that electrons and positrons are Dirac particle and antiparticle. The study measured the scattering cross section as a function of energy-transfer at three different incident energy points: 0.6 MeV, 0.8 MeV and 1.0 MeV, where positrons were scattered off a Mylar foil of 0.9 mg/cm² and 1.7 mg/cm² thickness. The article concludes with the plot shown in Figure 2.3 which shows the differential cross section measured at each point compared to the theoretical expectation. The authors comment that “the Bhabha formula is verified [...] to an accuracy of about 10% standard deviation”.

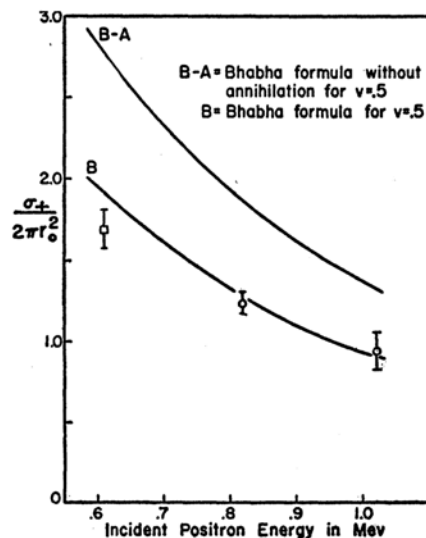


Figure 2.3: “Absolute differential cross section” [sic], at leading order of Bhabha scattering in range 0.6 to 1.0 MeV as found in [66]. The figure shows the value of the Bhabha scattering cross section in units of $2\pi r_0^2$, where $r_0 = e^2/m_e c^2$, as a function of the energy of the incident positron. The line marked as “B” shows the theoretical result expected for fractional momentum transfer $v = 0.5$, assuming that positrons and electrons are Dirac particle and antiparticle, and that the cross section therefore includes e^+e^- annihilation. The line marked “B-A” shows the theoretical expectation assuming no annihilation term. It is unclear from the paper whether this is the total or differential cross section and if it is the differential cross section, exactly what range of angles it covers.

In the 1980s, interest was renewed in this energy range after positron peaks in nuclear decays suggested a potential new particle of 1.8 MeV mass decaying to e^+e^- [67–70]. As discussed in [71], Bhabha scattering provides an excellent method to search for the existence of a particle of this nature. This led to a series of new measurements of Bhabha scattering in the range 1-2 GeV centre of mass energy [72–80]. After years of study, as explained in [81], the solution to the puzzle was that the nuclei were entering excited rotational states, and it was these states which were responsible for the peaks in the positron spectra.

2.3.2 Measurements at PADME energy scales

The other measurement which it is important to mention was published in 1959 and used 200 MeV positrons from the high-energy electron beam from the Stanford Mark III linear accelerator [82]. As in the experiment mentioned in the previous section, this experiment was also designed to test the Dirac nature of electrons and positrons.

In this experiment, electrons were accelerated to 350 MeV and fired onto a $\frac{1}{2}X_0$ Cu target in which positrons were produced in pair production from Bremsstrahlung photons created in the interaction between beam particles and the target nuclei. The resulting particles from the interactions in the target were left to coast along the beamline with no acceleration until they reached the magnet system at the end of the accelerator. A sketch of the beamline can be seen in Figure 2.4.

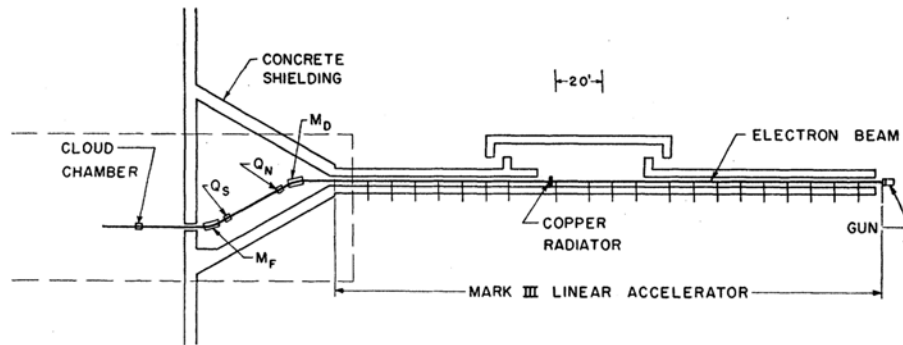


Figure 2.4: Beamline of SLAC Mark III accelerator used for Bhabha scattering measurement in [82]. M_D and M_F are deflecting magnets, while Q_N and Q_S are quadrupole magnets. The copper radiator is the target used for the production of positrons.

After being deflected by the magnet system, the particles left the vacuum of the beampipe through a 0.008 inch Mylar window placed 10 inches before the target, which was made of 1.99 g/cm^2 beryllium. The particle detection system used a cloud chamber placed inside a 5.5 kGauss magnetic field which allowed for the reconstruction of the momentum of tracks which left the target. The number of electrons leaving the target was then counted, and the beam luminosity was also measured by counting the total number of positron tracks to enter the cloud chamber.

The collaboration found that out of $(4.56 \pm 0.07) \times 10^5$ positrons on target, 216 ± 21 Bhabha scattering events were observed, in the range of fractional energy transfer $0.44 \leq \epsilon \leq 1.00$, which corresponds to scattering angles θ in the range $83^\circ \leq \theta \leq 180^\circ$. The authors don't explicitly convert these numbers into a cross section, however they do provide an expected number of events from QED at leading order, which they quote as 243 ± 5 . This leads to a difference between experiment and theory of 13%, corresponding to $\sim 1.1\sigma$. The authors ascribe this discrepancy to radiative corrections which had not been calculated and therefore could not be taken into account.

The conclusions of the article discussed above suggest that at beam energies of $O(100)$ MeV, radiative corrections become extremely important in the calculation of the expected rate of events. This is an important consideration in the context of this thesis since any Monte Carlo event generator which does not consider radiative corrections may produce significantly different results from those observed in nature.

2.4 Measurements at higher energies

Measurements of the Bhabha cross section as obtained by the L3 collaboration at LEP are presented in Table 2.1 [83]. Given that they were taken at more than 3 orders of magnitude higher centre of mass energy than that available at PADME, they are of little relevance to the measurement presented in this thesis.

Table 2.1: Bhabha scattering measurements at LEP [83]. The table presents the number of selected radiative Bhabha scattering events, N_{ee} , as a function of the range \sqrt{s} considered and the average energy in the range considered $\langle\sqrt{s}\rangle$. σ_{ee} gives the measured cross section in the specified range, while σ_{ee}^{Born} gives the Standard Model improved Born level cross sections

\sqrt{s} [GeV]	$\langle\sqrt{s}\rangle$ [GeV]	N_{ee}	$\sigma_{ee} \pm (\text{stat.}) \pm (\text{syst.})$ [pb]	σ_{ee}^{Born} [pb]
< 60	52.0	152	$449.4 \pm 35.1 \pm 20.2$	423.7
60 – 68	64.5	153	$258.3 \pm 23.5 \pm 12.5$	285.1
68 – 76	72.5	335	$231.5 \pm 13.2 \pm 7.4$	238.2
76 – 82	79.2	594	$235.5 \pm 9.3 \pm 5.5$	223.9
82 – 85	83.7	575	$224.0 \pm 10.6 \pm 5.9$	246.0
85 – 87	86.1	622	$300.0 \pm 12.6 \pm 8.1$	297.6
87 – 92	88.3	169	$483.9 \pm 37.1 \pm 13.2$	471.5
92 – 105	96.9	36	$117.6 \pm 16.9 \pm 8.3$	101.4
105 – 130	118.4	68	$76.1 \pm 7.8 \pm 3.7$	63.5
130 – 160	148.2	70	$34.0 \pm 5.0 \pm 2.3$	41.3
160 – 175	167.1	82	$33.5 \pm 3.6 \pm 2.1$	32.5

The luminosity measurement used in the measurements presented in Table 2.1 was based on measuring the number of Bhabha events at small angles to the beam and using QED to calculate the number of e^+e^- interactions that had taken place [84]. This means that the strongest statement that can be applied to these measurements is that, assuming no new physics at small scattering angles, the number of events recorded with large scattering angles also agrees with QED. If there were new physics which affected both the wide-angle and the small-angle scattering processes at the same rate then it would not have been observed at L3.

A Dark Photon or other new massive boson decaying to e^+e^- would have a kinematic spectrum similar to that of S-channel Bhabha scattering, which has a very flat angular distribution in the centre of mass, as seen in Figure 2.2b. This means that if a new boson of this nature exists, the LEP measurements would almost certainly be insensitive to it, meaning that these measurements are not analogous to the Dark Sector searches performed at PADME.

Other experiments such as CELLO at the PETRA machine and TOPAZ also performed the same type of measurement, comparing wide-angle scattering to small-angle scattering [85, 86]. Most of these measurements are also made at very high energies compared to those available at PADME. Apart from the experiment discussed in Section 2.3.2, which in any case did not convert the number of signals found to a cross section, measurements of the Bhabha scattering cross section have not been made either at PADME energy scales, or without using small-angle scattering as a normalisation factor to allow measurement of the wide-angle scattering cross-section. The measurement presented in this thesis is therefore an important addition to the literature, presenting a measurement of the total Bhabha scattering cross section at $\sqrt{20}$ MeV with an independent luminosity monitor.

Chapter 3

The PADME Experiment

The PADME detector, shown schematically in Figure 3.1, was designed to search for a dark photon (A') created in the associated production process $e^+e^- \rightarrow \gamma A'$, as described in Section 3.2 [87]. For this reason the experimental setup originally consisted of an active diamond Target where positrons from the beam annihilate (Section 3.2.1) and an Electromagnetic Calorimeter (ECal) to detect the Standard Model photon in the signal (Section 3.2.2). To reduce background from Bremsstrahlung photons, the angular distribution of which peaks at small angles to the beam, the ECal was built with a central hole and a second, faster calorimeter known as the Small Angle Calorimeter (SAC) was built behind this hole to cover small angles to the beam (Section 3.2.3).

Beam positrons that lose energy through Bremsstrahlung in the Target are deflected by a dipole magnetic field (Section 3.2.4) into the charged particle Veto system (Section 3.2.5). The TIMEPIX pixel detector described in Section 3.2.6 was designed to be used as an online beam-monitoring system.

For better resolution in searches for visible decays of the X17 particle, in PADME Run 3 the magnetic field was turned off and a new sub-detector known as the “ETagger” was added to the PADME setup in order to tag charged particles as they enter the calorimeter (Section 3.2.7).

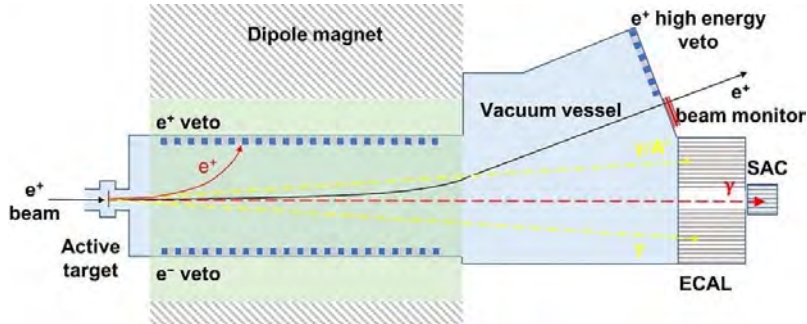


Figure 3.1: Schematic of PADME detector, showing all subdetectors and an $e^+e^- \rightarrow \gamma\gamma$ or $e^+e^- \rightarrow \gamma A'$ event in yellow and a Bremsstrahlung event in red. The trajectory of beam particles which don't interact in the Target is represented in black.

3.1 Experimental Hall and Beam Setup

The PADME apparatus is installed in the Beam Test Facility (BTF) of the DAΦNE ϕ -factory at the National Laboratories of Frascati (LNF). Figure 3.2 shows a schematic representation of the DAΦNE accelerator complex. The BTF can provide beams of either electrons or positrons, at different energies, numbers of positrons per bunch and bunch lengths, depending on the

configuration of the LINAC beamline. Primary electrons are produced by a gridded electron gun, while two different targets for positron conversion are placed in different positions along the beamline.

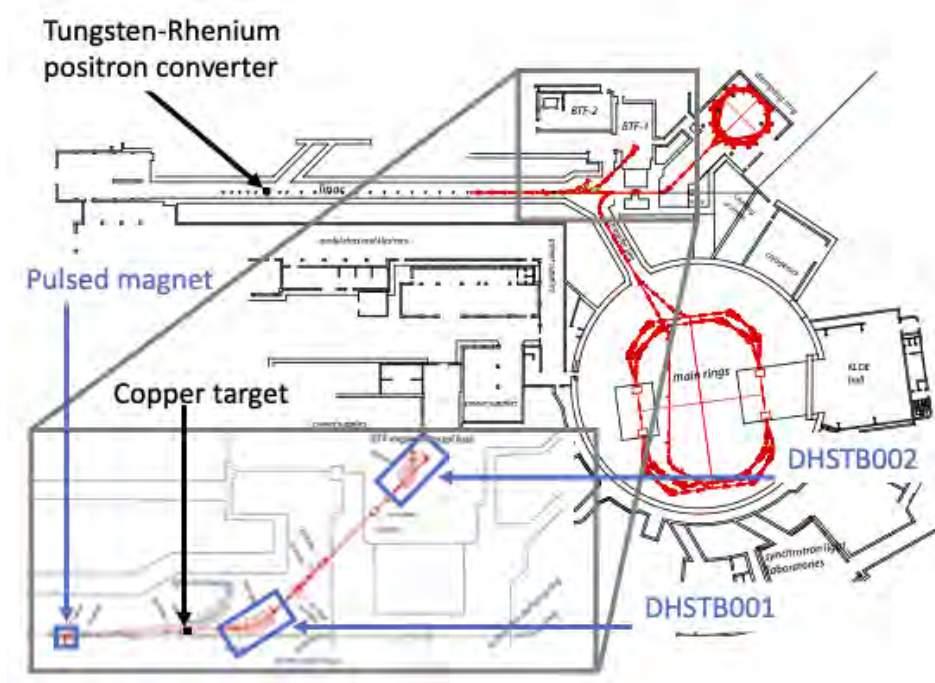


Figure 3.2: Layout of DAΦNE accelerator complex. The inset shows the BTF transfer line in detail. Two different targets can be used to produce positrons: the positron converter or the BTF secondary copper target. These are highlighted in black. In blue, the pulsed dipole and the BTF dipoles DHSTB001 and DHSTB002 can be seen.

Two types of positron beam production are possible:

- Primary positron beam production: positrons are created firing 250 MeV electrons with a $2X_0$ Tungsten-Rhenium positron converter placed near the entrance to the LINAC tunnel, after the first five accelerating sections. This is the method used to create e^+ beams to inject in the main ring and has the advantage of causing very little beam-induced background in the BTF. The positrons are then accelerated up to a maximum of 510 MeV by the rest of the LINAC.
- Secondary beam production: positrons are created firing 750 MeV electrons onto a $1.7X_0$ copper target placed at the end of the LINAC tunnel just before the dipole which directs the beam into the BTF. The secondary positron beam produces more background but has a maximum energy of ~ 550 MeV.

The two different positron-producing targets are shown in black in Figure 3.2, and the parameters of the different types of beams are summarised in Table 3.1

Table 3.1: Beam characteristics for different beam types at BTF [88].

Parameter	e ⁻	primary e ⁺	secondary e ⁺
Maximum beam energy [MeV]	800	510	550
RF frequency [MHz]	2856	2856	2856
Beam pulse length [ns]	1-300	1-300	1-300
RMS energy spread	0.56	< 0.96	0.96
LINAC repetition rate [Hz]	1-50	1-50	1-50
Emittance [mm mrad]	1	~ 1	~ 1
Divergence [mrad]	1-1.5	1-1.5	1-1.5

Electrons/positrons are deflected along the BTF beamline by a pulsed dipole (highlighted in blue in inset of Figure 3.2) which sends 49 bunches per second towards the BTF and one to a hodoscope which is used to measure the beam momentum.

The positron beam is then steered into the BTF hall by the dipole DHSTB001, focused by a pair of quadrupoles, transported through the wall into BTF, where it is focused by a second pair of quadrupoles and finally deflected into the PADME experiment by the dipole DHSTB002 (also in blue in inset of Figure 3.2).

To separate the 10^{-6} bar PADME vacuum from the 10^{-8} bar linac vacuum, until July 2019 a $250 \mu\text{m}$ beryllium window was placed after the BTF wall and before the final pair of quadrupoles, as shown schematically in Figure 3.3. After the initial data-taking run, however, a large amount of background was observed in the ECal. Using the Monte Carlo simulation of the full beamline described in [89], it was understood that the most significant source of this background was the beryllium window. An intervention was therefore made to move the window to immediately before the PADME Target, however during the repositioning process the window broke and the run had to be paused.

The broken beryllium window was replaced with a $125 \mu\text{m}$ thick Mylar window, placed immediately after the DHSTB001 dipole, as shown in Figure 3.3. This is the configuration for all data taken after July 2019.

A sketch (not to scale) of the path taken by the beam is shown in Figure 3.3.

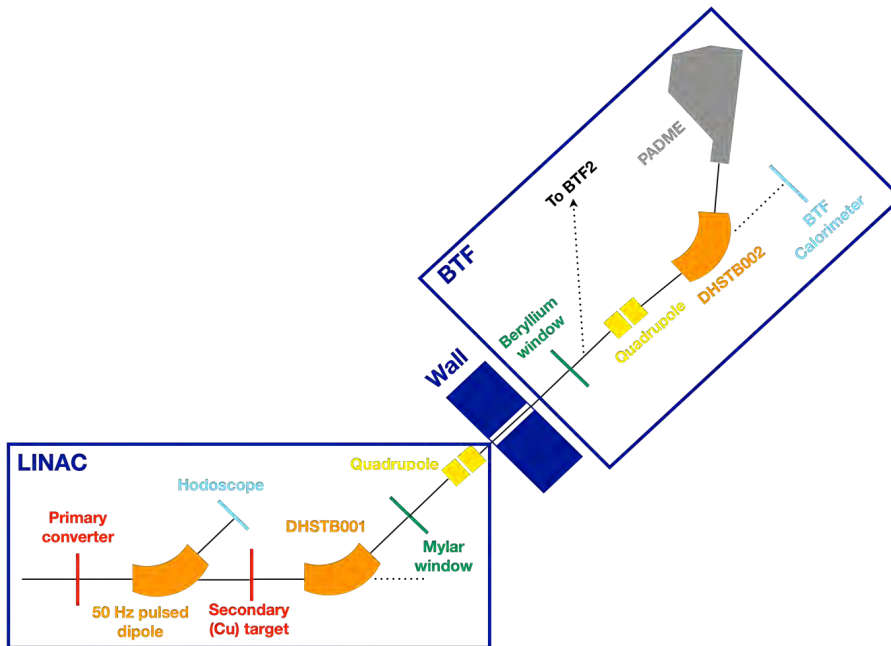


Figure 3.3: Not-to-scale sketch of beam path. As shown in the technical drawing in Figure 3.2, the primary positron converter is much further upstream than indicated in this sketch.

The beam characteristics required by PADME are:

- $< 1\%$ beam momentum spread;
- Beam spot size of order 1 mm;
- Angular divergence of beam \sim few mrad;
- up to $\sim 20\text{k-}30\text{k}$ particles on target (PoT) per bunch;
- Long bunch spills so that the beam flux is < 100 PoT per ns

3.2 The PADME Detector

PADME was designed to search for dark photons (A') in associated production with a Standard Model photon in the reaction $e^+e^- \rightarrow \gamma A'$, where positrons from the beam annihilate with electrons in the fixed Target, producing a signal of a single Standard Model photon in the final state.

Measuring the energy and momentum of the Standard Model photon gives access to the missing momentum and therefore the mass of the A' , given by:

$$M(A')^2 = (P_{e^+} + P_{e^-} - P_\gamma)^2$$

where $P_{e^+,e^-, \gamma}$ is the four-momentum of the incoming positron, incoming electron, and outgoing photon respectively.

The main components of the PADME detector are:

- Active diamond Target (Section 3.2.1);
- Electromagnetic Calorimeter (ECal) (Section 3.2.2);
- Small Angle electromagnetic Calorimeter (SAC) (Section 3.2.3);
- Dipole magnet (Section 3.2.4);
- Charged particle veto system (Section 3.2.5);

In the following sections a detailed description of each subdetector is given.

3.2.1 Active diamond Target

To reconstruct the momentum of photons in the final state, the position of annihilation must be known. Moreover, to set limits on the couplings of new particles, and in order to make Standard Model cross-section measurements such as that presented in Chapter 6 of this thesis, PADME needed an independent measure of luminosity.

For these reasons, the Target was designed to be able to measure beam position, intensity and spot size, bunch by bunch. The material chosen to do this needed to be a radiation hard solid to withstand the beam intensity, and had to have a low atomic number (Z) since the cross section of Bremsstrahlung (the main source of background at PADME) scales as Z^2 . For these reasons, the target is made of diamond.

The $2\text{ cm} \times 2\text{ cm} \times 97\text{ }\mu\text{m}$ target crystal was created using chemical vapour deposition (CVD) by Applied Diamond Inc. in the USA. To measure the x and y position of the beam, orthogonal graphite strips were created by the INFN Lecce group on opposite sides of the target using an ArF laser. 19 strips in x and 19 strips in y of $850\mu\text{m} \times 1.9\text{ cm}$ were created and bonded to the front-end readout electronics. The production process of the Target is described in detail in [90].

The Target is located inside the PADME vacuum pipe and can be moved into or out of the beam trajectory using a remote controlled step motor. The Target setup with front-end electronics can be seen in Figure 3.4.

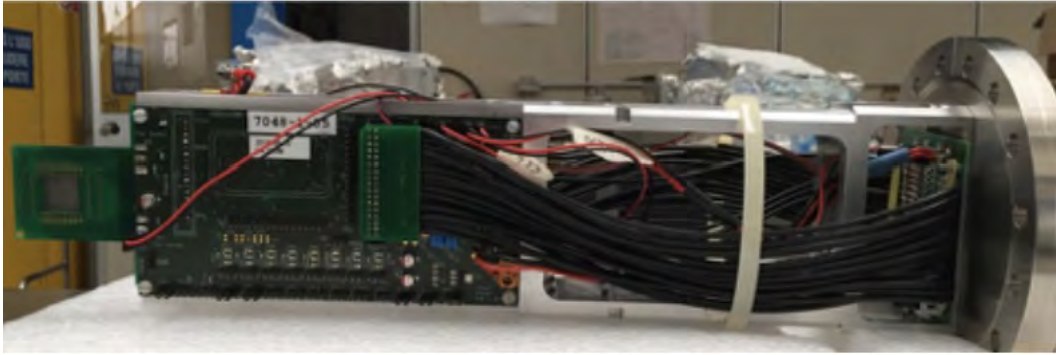


Figure 3.4: Target setup before being installed into beamline

Specific runs were taken during the beam commissioning for Run 2 which used the BTF calorimeter to calibrate the measurement of number of positrons per bunch, known as the “multiplicity”, detected by the Target. The magnet DHSTB002 was turned off to send the beam onto the BTF calorimeter and the multiplicity was measured. The magnet was then turned back on, the beam sent into PADME and the response of the target was evaluated. The outcome of this process in two different sets of data can be seen in Figure 3.5.

It can be seen here that focussing the beam on a single graphite strip of the Target causes the detector to saturate at high multiplicities. This problem was ameliorated by ensuring the Target was placed so that the beam hit two different strips, and by using a reconstruction method which was not based on the most intensely hit strips. More information about the Target and the multiplicity reconstruction can be found in [90].

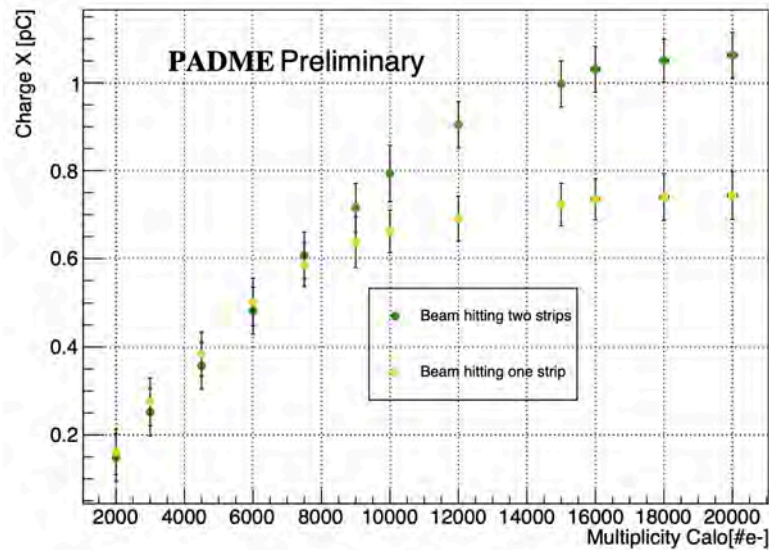
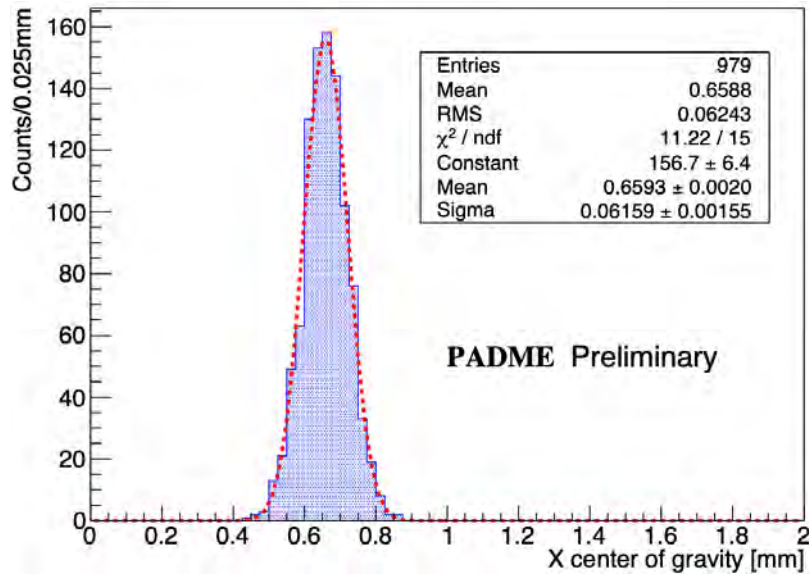


Figure 3.5: Charge collected in x view of target as a function of multiplicity measured by BTF calorimeter, with the beam centred on one x strip (yellow) and with the beam split between two x strips (green)

The beam position is taken from the charge centroid on the target, as seen in Figure 3.6 for the x coordinate. The spatial resolution is given as the width of the centroid distribution, and was measured to be 0.0616 ± 0.0016 mm for the x view.

Figure 3.6: Charge centroid distribution in x

3.2.2 Electromagnetic calorimeter

The electromagnetic calorimeter (ECal) was designed to detect the Standard Model photon produced in association with the dark photon (A'), as well as both photons produced in Standard Model annihilation ($e^+e^- \rightarrow \gamma\gamma$). It is composed of 616 parallelepiped BGO crystals, measuring $21 \times 21 \times 230 \text{ mm}^2$ and is placed 3.463 m downstream of the PADME target. Each crystal is glued to a HZC XP1911 photomultiplier tube (PMT).

The decay time of light emission in BGO crystals is relatively slow, with a time constant τ of $\tau=300 \text{ ns}$, meaning that signals are $\sim 1 \mu\text{s}$ in duration, limiting the maximum rate acceptable in the detector. Studying the Bremsstrahlung distribution it was found that the rate of this process would overwhelm the ECal, particularly in the region at small angles to the beam, where the Bremsstrahlung photon spectrum peaks. For this reason the detector was built with a hole in the centre measuring $105 \times 105 \text{ mm}^2$ (5×5 crystals), behind which is the Small Angle Calorimeter described in Section 3.2.3. The ECal crystals are arranged cylindrically around the central hole, as seen in Figure 3.7 and Figure 3.8.

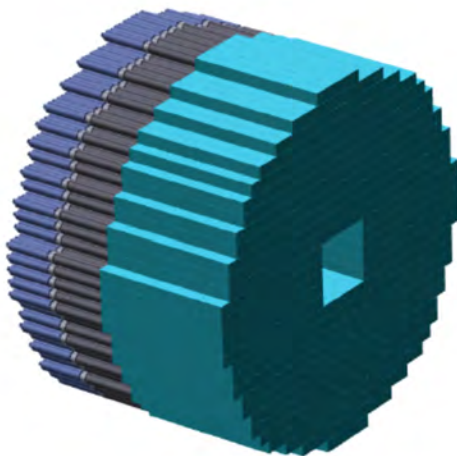


Figure 3.7: Schematic diagram of ECal

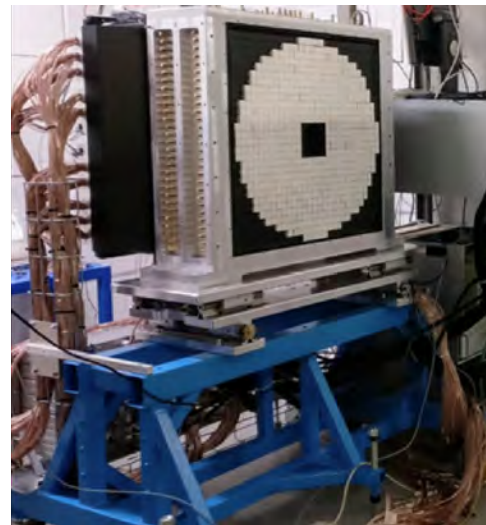


Figure 3.8: ECal with front crystals uncovered.

The BGO crystals were recovered from the calorimeter of the L3 experiment at LEP. From L3, the expected energy resolution was $\frac{(1-2)\%}{\sqrt{E(\text{GeV})}}$. As reported in [91], the energy resolution of the calorimeter at 490 MeV beam energy is 2.62 ± 0.05 (stat)% and the efficiency of the detector for cosmic ray muons is $\geq 98\%$ for 99.1% of the channels. The estimated spatial resolution is ~ 3 mm in both x and y .

3.2.3 Small Angle Calorimeter

In order to cope with the very high rate of Bremsstrahlung photons produced at small angles to the beamline, a second, faster calorimeter was built and placed behind the ECal to cover the angular range $[0, 18.9]$ mrad. This calorimeter is known as the Small Angle Calorimeter (SAC) and is made of 25 PbF_2 crystals of dimension $30 \times 30 \times 140$ mm³, each coupled to a R13478UV Hamamatsu photomultiplier tube. Since PbF_2 is a Cherenkov radiator, the emission of the light is instantaneous and has no decay time. For this reason the detector has a signal width of $O(2)$ ns, making it able to sustain a much higher rate of Bremsstrahlung than the ECal.

The SAC is also able to veto 3-photon annihilation events where two photons are produced in the forward direction and the third is detected in the ECal – events which would otherwise appear as single photon events in the ECal, causing background to the Dark Photon signal.

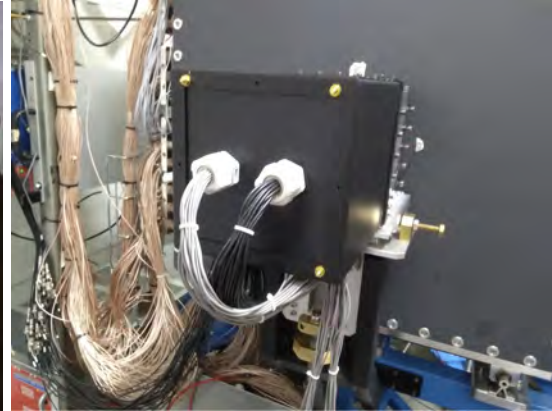


Figure 3.9: Back of SAC during assembly.

Figure 3.10: Placement of SAC behind ECal.

The timing and energy resolution requirements for the SAC were better than 200 ps and better than 10% of beam energy respectively. In prototype tests described in [92], the measured resolutions were 81 ps and 10% at 550 MeV respectively.

3.2.4 The PADME dipole magnet

The PADME magnetic field serves two main functions:

- First, to prevent any beam positrons which have not interacted in the target from reaching the SAC, which at 28k positrons per bunch would be overwhelmed;
- Second, to divert positrons which have lost energy through Bremsstrahlung in the Target into the PVeto/HEPVeto detectors, and allow the rejection of Bremsstrahlung photons, the main source of background in the single photon analysis.

The requirements for the PADME magnet are listed in Table 3.2, where the constraints on weight and maximum power consumption are imposed by the maximum load of the BTF crane (30 tonnes) and by the availability of power supplies at LNF respectively.

Table 3.2: Main requirements for the PADME dipole magnet [93].

Parameter	Value
B field	>0.42 T
Length	1 m
Vertical gap	20 cm
Horizontal gap	>40 cm
Weight	<30 t
Power	<100 kW

Characteristics matching the requirements were found in the dipole series MBP-S of the CERN SPS transfer line. These magnets had length 1 m, width 52 cm, vertical gap 20 cm and weight 15 tonnes. A spare one was shipped to Frascati where it was refurbished to increase the vertical gap to 23 cm, and its magnetic field was remapped before installation in the BTF hall. The technical drawings for the magnet show its geometrical parameters after the widening of the vertical gap, see Figure 3.11. The magnetic field in Gauss in the good field region ($B(Gauss)$) was calibrated as a function of current (I), leading to the following relation:

$$B(Gauss) = 19.44 I + 32.801$$

Using this information, the current was adjusted to provide a magnetic field which sent positrons at the beam energy from the centre of the target towards the TimePix3 detector used as a beam monitor, described in detail in Section 3.2.6. The nominal magnet current for Run 2 was 183.5 A, giving a magnetic field of 3.6 kGauss.

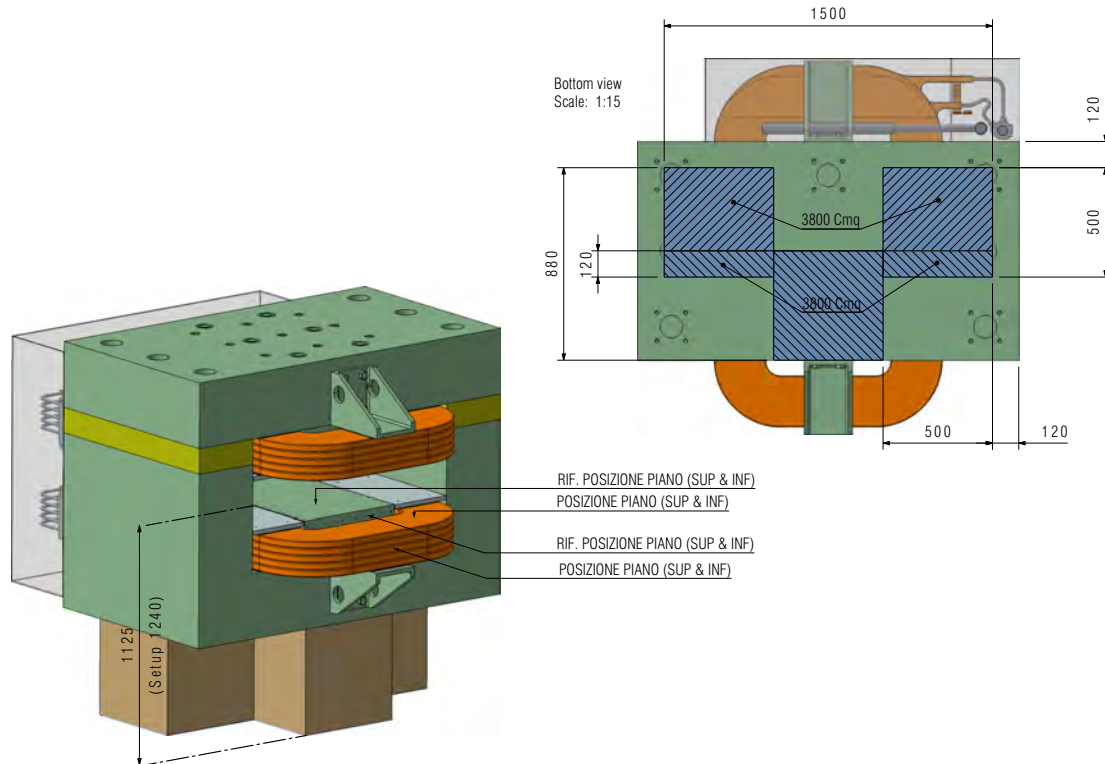


Figure 3.11: Mechanical drawing of the PADME Dipole

The magnetic field as a function of (x, z) coordinate of the magnet is shown in Figure 3.12. The centre of the magnet is $(x, y, z) = (0, 0, 0)$.

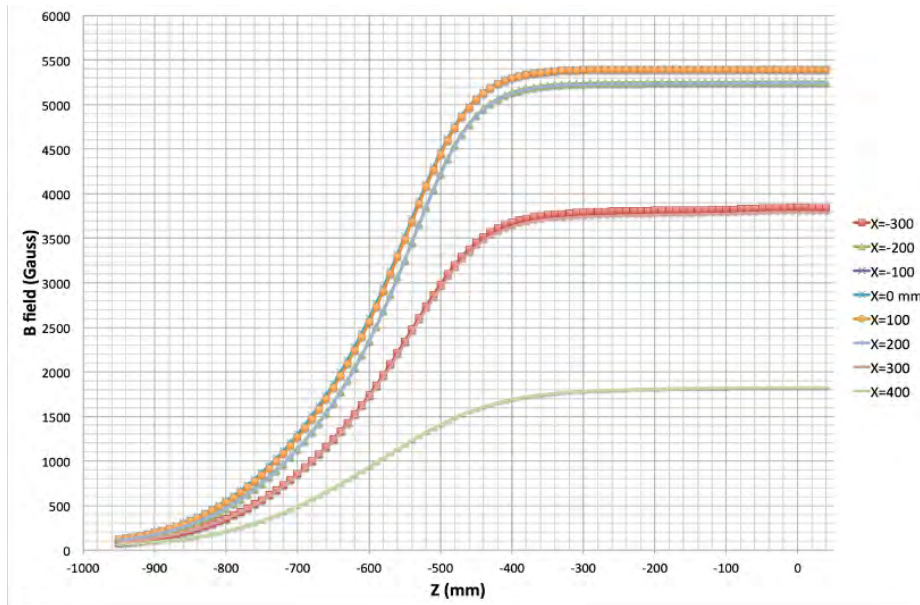


Figure 3.12: Magnetic field, B , as a function of z -coordinate and x -coordinate. The centre of the magnet is at $(x, y, z) = (0, 0, 0)$.

3.2.5 Charged Particle Vetoes

To veto single photons in the ECal coming from Bremsstrahlung which could otherwise be mistaken for the dark photon signal, a detector was constructed to identify the accompanying positron which loses energy in the Bremsstrahlung interaction in the target. This detector is known as the Positron Veto (PVeto) and is made of 90 plastic scintillators placed vertically in the magnetic field, as seen in Figure 3.13. The bars, produced by UNIPLAST, have dimensions $10 \times 10 \times 178$ mm and are made of plastic polystyrene-based material with a 1.5% concentration of POPOP. An optical wavelength-shifting fiber (WLS), Bicron BCF-92, is placed within a 1.3×1.3 mm² longitudinal groove in each of the scintillating bars and glued with Eljen EJ500 optical epoxy cement. The maximal emission wavelength of the BCF-92 fiber is 492 nm and the maximal absorption wavelength is approximately 400 nm (matching the POPOP emission spectrum). Hamamatsu 13360 Silicon photo-multipliers (SiPMs), which are able to work in vacuum and sustain a magnetic field of about 0.6 T, convert the photons into electrical signals.



Figure 3.13: Vetoes inside magnetic field. PVeto is on the right, EVeto on the left.

Given the relatively low cost of this type of detector, a similar detector was built on the other side of the vacuum chamber in the magnetic field. This second detector, known as the Electron Veto (EVeto), is able to detect electrons produced in Bhabha scattering processes in the target as well as potential e^+e^- final states coming from short-range visible decays of a dark photon. It consists of 96 bars of plastic scintillator configured analogously to the PVeto bars.

A third set of 16 bars is placed outside of the magnetic field, perpendicular to the beam line after bending by the magnetic field (see Figure 3.1). This detector, known as the High Energy Positron Veto (HEPVeto) is designed to detect positrons which have lost little energy through Bremsstrahlung in the target. Since the Bremsstrahlung spectrum peaks at low photon energies, most Bremsstrahlung positrons are expected in this detector. Therefore the electronic readout was doubled, placing one SiPM at each extreme of the bars to cope with the increased rate.

3.2.6 Timepix based Beam Monitor

To study the spatial and temporal structure of the beam, a silicon pixel detector was placed in line with the beam exit for particles which don't lose energy in interactions with the target. This detector, produced by the ADVACAM company, is composed of 12 Timepix-3 detectors, each a 256×256 matrix of pixels, with a pitch of $55 \mu\text{m}$, creating a total surface area of $8.4 \times 2.8 \text{ cm}^2$. During data taking runs 1 and 2, the Timepix detector was not integrated into the standard PADME DAQ. Data from the detector was acquired in stand-alone processes and correlation with information from other detectors was performed offline, using the timestamp of the frames collected. The Timepix setup can be seen in Figure 3.14.



Figure 3.14: Timepix detector setup.

3.2.7 Charged Particle Tagger

As discussed in Section 1.6, in April 2021, A.J. Krasznahorkay and colleagues from the ATOMKI institute and the University of Debrecen in Hungary published three new data points to add to the growing body of evidence for a new particle of approximately 17 MeV mass, known frequently as the “X17” particle, observed in the internal pair creation decays of excited atomic nuclei [94]. As the work described in Chapter 6 developed, it became clear that the PADME setup from Runs 1 and 2 was not ideal to study visible decays, such as the processes indicated by the X17 anomaly. The PADME collaboration was therefore prompted to modify the detector setup to study visible final states with better precision.

In order to improve the precision of the energy measurement, it was decided to turn off the magnetic field so that all final state particles were sent towards the calorimeter system. To distinguish photons from charged particles in this setup, a new Electron Tagger (ETag) detector was built, made of 18 plastic scintillating bars of $4\text{ cm} \times 60\text{ cm} \times 0.5\text{ cm}$, shown in Figure 3.15. This made the visible signal in the new setup a pair of particles in the calorimeter, in time, with combined energy which summed to the beam energy, which also produced signals in the Electron Tagger.

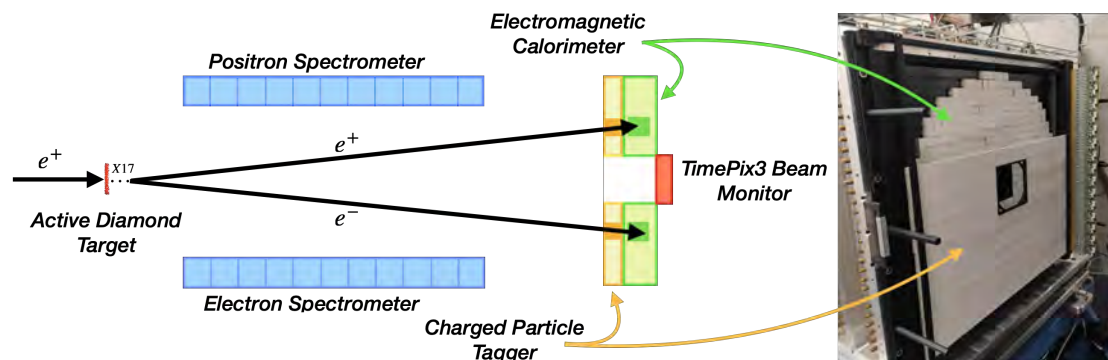


Figure 3.15: Schematic of PADME setup for Run 3. The photo on the right hand side shows the ETag in construction in front of the ECal. The lifetime of the X17 would in reality be ~ 0 , here it is only shown leaving the target for clarity about the process considered.

3.3 Trigger and Data Acquisition

The PADME data acquisition system reads data from a total of 897 channels with an acquisition rate of ~ 50 Hz, dominated by the LINAC operation frequency. All channels are connected to a set of 29 CAEN V1742 switched capacitor ADC boards based on the DRS4 chip consisting of a 1024 cell switched capacitor array. The sampling rate is tunable in the range 1-5 GS/s and the resolution is 12 bits. The Target signal and the relatively slow signal produced by the BGO crystals are sampled at 1 GS/s, while the faster signals from the charged particle vetoes and the SAC are sampled at 2.5 GS/s. Dedicated PCI Express boards collect data from all ADC boards via 8 optical links.

All ADC boards are interfaced with the main PADME Trigger and Timing System (TTS). The TTS consists of a main trigger board and two trigger distribution units. The trigger board can receive up to six NIM-type external triggers. During Run 2, three triggers were in use. These were:

- The beam trigger: an external trigger sent from the BTF before the arrival of a positron bunch from the LINAC (49 Hz);
- The cosmic trigger: on arrival of a cosmic ray as discussed in detail in [91] (~ 5 -10 Hz);
- The “off-beam” trigger: a “delayed” trigger designed specifically to acquire out-of-bunch data (~ 2 Hz)

The total rate of data acquisition at PADME DAQ is > 60 Hz.

The data acquisition process is organised into two stages: level 0 collects data from the ADC boards while level 1 merges all data into a single event structure and produces the final data files. All data produced by the PADME DAQ system are written to a local disk buffer directly connected to the level 1 servers.

3.4 Data Taking at the PADME Experiment

The data used in the analysis for this thesis come from the second data-taking run, known as Run 2, the parameters of which were decided upon after detailed studies of the different beam line configurations used during the first run and of detailed Monte Carlo simulations of the whole beamline, as discussed in [89, 95]. The timeline of data-taking from first switch on to the end of 2020 is shown in Figure 3.16.

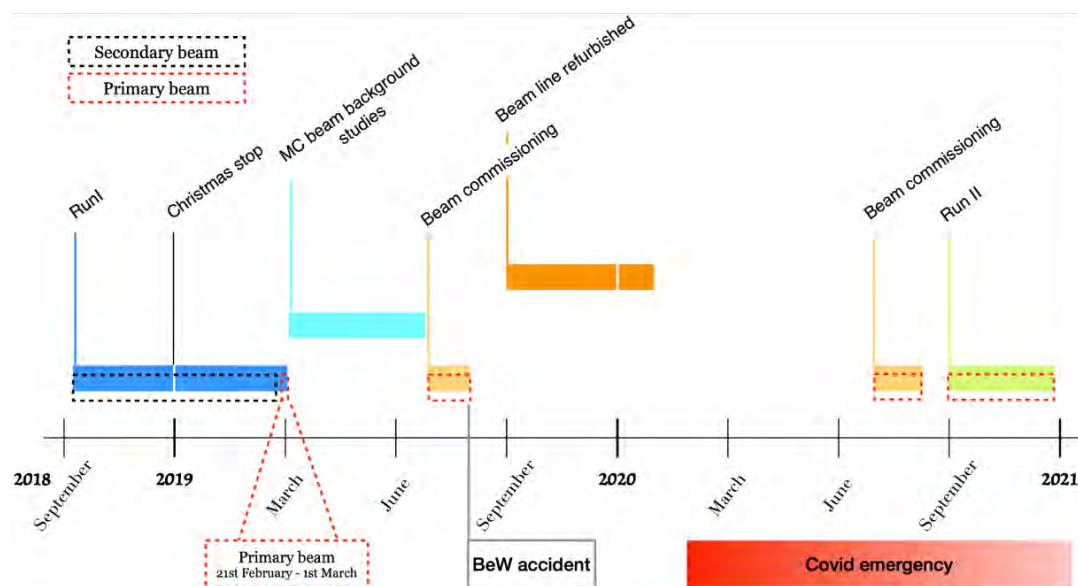


Figure 3.16: Data-taking in PADME up to end of Run 2.

3.4.1 Data-Taking Run 1

After 6 weeks of beam conditioning from September to October 2018, the default conditions for Run 1 were:

- Secondary e^+ beam;
- 545 MeV beam energy;
- $\sim 20 \times 10^3$ positrons on Target (PoT) per bunch;
- ~ 250 ns bunch length

Data-taking was paused in December for the Christmas holiday plus 2 weeks maintenance, before restarting in mid-January 2019 and continuing with these conditions until mid-February. From the 21st of February until the end of the run on the 1st of March, the primary e^+ beam was used with 490 MeV energy and a shorter bunch length of 150 ns, in order to study contributions to the background.

The integrated luminosity collected in Run 1 is shown in Figure 3.17, reaching a total of $(6.37 \pm 0.32_{sys}) \times 10^{12}$ PoT.

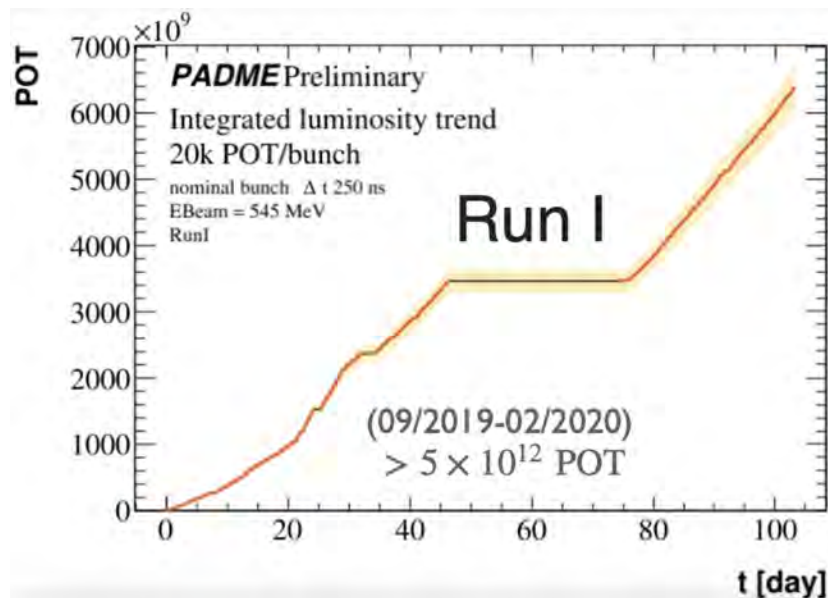


Figure 3.17: Integrated luminosity collected over Run 1. The orange points give the cumulative measure of positrons on Target (PoT) while the yellow band shows the 5% systematic error.

Studying the total energy deposited in the ECal per bunch gives a good estimate of the level of background at PADME. As can be seen in Figure 3.18, using the primary beam gave a significant reduction in the total energy in the calorimeter, demonstrating a clear improvement in the background conditions of the experiment. For this reason, the decision was made to continue using the primary beam during Run 2.

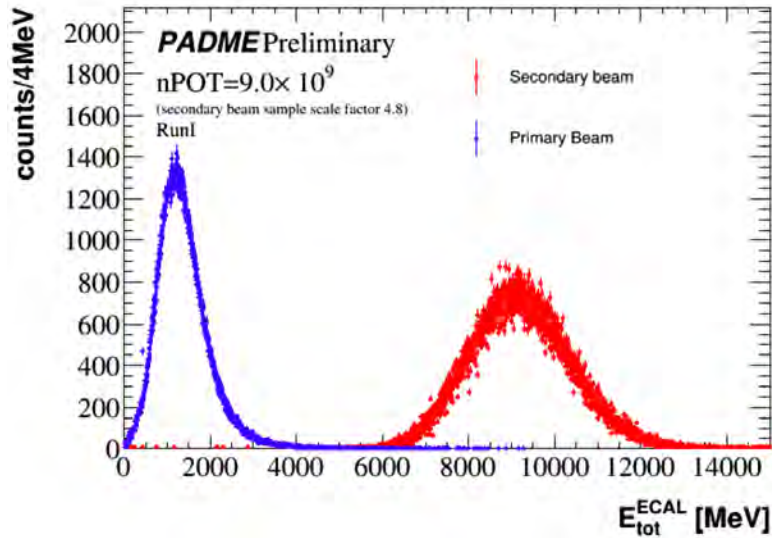


Figure 3.18: Total energy per bunch in ECal in Run 1, for each beam line configuration.

3.4.2 Data-taking Run 2

The start of Run 2 was delayed by the national lockdown due to the Covid-19 pandemic. PADME had the good fortune to be able to restart beam commissioning in the summer of 2020, however the lockdown still caused a delay of several months to the data-taking, and thus in the timeline of the analysis for this thesis.

Data-taking for Run 2 started in mid-September that year and continued until winter of 2020, working in accordance with the regional restrictions in place during the period. This ability was aided by the possibility of monitoring the data-taking remotely, meaning that international colleagues were able to cover shifts from their home countries instead of having to travel to Frascati to complete them. This was made possible by the online monitoring of the detector, described in Section 3.4.4.

The standard beam conditions for Run 2 were the following:

- Primary e^+ beam;
- 431 MeV beam energy
- $\sim 27 \times 10^3$ positrons on Target (PoT) per bunch
- 280 ns bunch length

Figure 3.19 shows the total energy per bunch collected in the ECal in Run 2 compared to the so-called “golden run” of Run 1, which used the primary positron beam at 490 MeV. It can be seen from this that the background level was significantly reduced by the adjustments to the beam line made in the long shutdown.

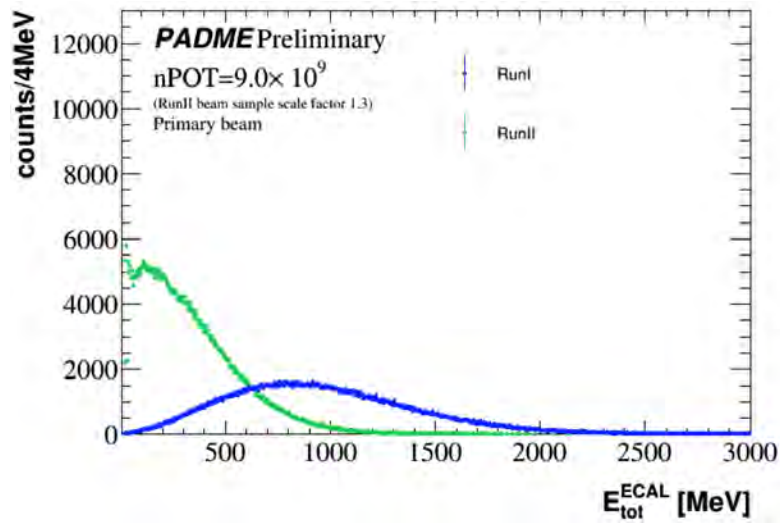


Figure 3.19: Total energy per bunch collected in ECal in Run 2 (green) compared to Run 1 (blue).

At the end of Run 2, $(5.47 \pm 0.27_{sys}) \times 10^{12}$ PoT were collected. The integrated luminosity as a function of time can be seen in Figure 3.20.

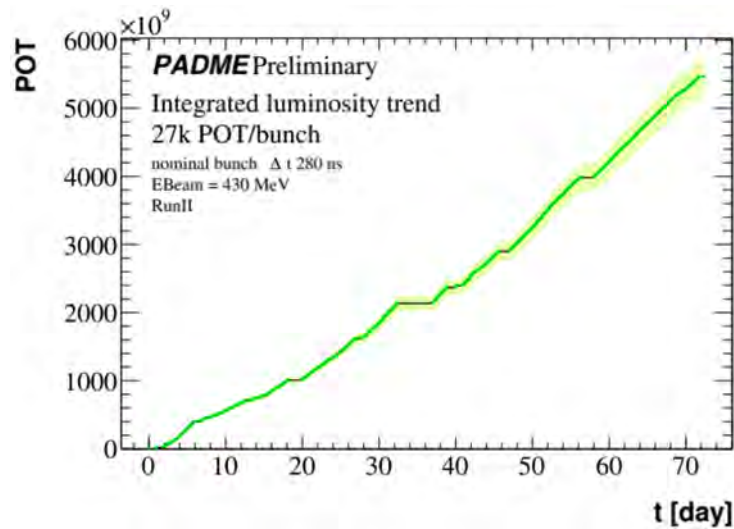


Figure 3.20: Integrated luminosity collected during Run 2. The green points give the cumulative measurement of positrons on Target (PoT) while the band shows the 5% systematic error.

During the Run, a few types of “special runs” were taken. The two important types for this thesis are:

- The “no-Target run” which saw the Target moved into and out of the beamline at various points, in order to study the beam-induced background, coming from interactions of beam particles outside of the Target
- A run taken with the magnetic field reversed to send positrons towards the EVeto side of the vacuum chamber, used to have enough statistics in the EVeto to be able to perform equalisation of the electronic gain for individual channels and correct for the time delay induced by cables.

3.4.3 Run 3: X17-dedicated data-taking run

In late 2021/early 2022, thanks in part to the work discussed in this thesis, it was understood that making precision measurements of the $e^+e^- \rightarrow e^+e^-$ cross section with the original PADME setup was a very challenging task. More detail about these challenges is presented in Chapter 6. Also in late 2021, the ATOMKI collaboration presented new measurements of ^{12}C decays at the X17 workshop in Rome [96], later published in November 2022 [97]. On the basis of these two developments, it was decided that to search specifically for charged particle final states, a new experimental setup would be needed.

Since it was discovered that measuring the invariant mass of e^+e^- final states with the Vetoes was a very difficult task, it was decided to turn off the magnetic field, sending all particles straight downstream towards the ECal. In order to “tag” charged particles, distinguishing them from photons, the ETag was built in front of the Calorimeter, as discussed in Section 3.2.7.

Since in this case the hypothesised parameters of the particle were known with good precision, precision in the measurement was valued over extremely high statistics. For this reason, the beam intensity was reduced to 2.5 kPoT/bunch to reduce pile-up. Knowing the mass also allowed the collaboration to change the beam energy: instead of running at the highest energy possible to cover the maximum achievable mass region, the energy was reduced to have \sqrt{s} as close as possible to the mass of the X17, since, as discussed in [98], producing an X17-like particle at its resonant energy causes a very significant increase in the production cross-section.

Given that the energy of positrons reaching the PADME target can be controlled to approximately 0.7 MeV at $\sqrt{s} \sim 17$ MeV, in 2022 an energy scan was performed, taking approximately 10^{10} Positrons on Target (PoT) per point over 47 different energy points in the region 5σ below and 4σ above the mean mass of the particle. Figure 3.21 shows the projected sensitivity of a data-taking campaign using this strategy, for the case that the X17 is a vector particle or an ALP [98]. The final sensitivity expected from PADME Run 3 has the mass range of the wider distribution but the spacing between points and the reach in coupling strength of the thinner, deeper distribution.

Work is currently ongoing to analyse the data taken in this Run.

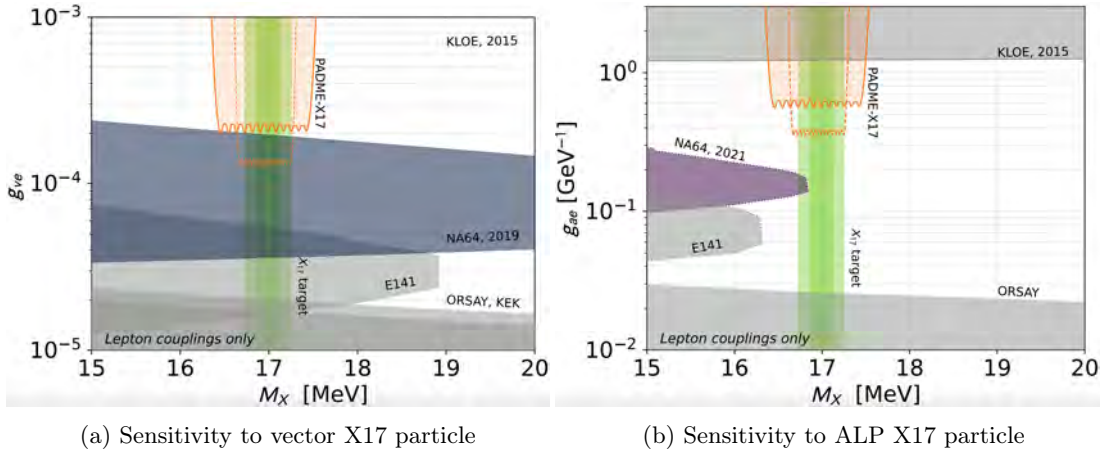


Figure 3.21: Predicted PADME sensitivity to X17 particle in the case that it’s a vector particle (a) or an ALP (b)[98]

3.4.4 Online Monitoring System

Monitoring tools have been developed to control the operation of the detector and check its stability during data-taking. The parameters to be controlled fall into two categories:

- physical variables in the detectors, such as occupancy, energy or time distribution;
- hardware settings and ambient parameters

The two classes are managed by the DAQ system, mentioned above, and the Detector Control System. Both generate data files that are displayed via a web-based online monitor.

In Runs 2 and 3, the online monitoring system was of fundamental importance to allow shifts to be run remotely. The monitor showed instantaneous information about the number of PoT per bunch, the total energy in the ECal, the occupancy in the Vetoes, the ECal and the SAC and other important information regarding the quality of the data being taken. An example of a screenshot from the Online Monitor in Run 30660, used in the analysis in Chapter 6, is shown in Figure 3.22. As well as information about the individual detectors, the Monitor also shows information about the data acquisition system and the status of both the BTF magnets DHSTB001 and DHSTB002 and the PADME magnet. A screenshot of this information from the same run is seen in Figure 3.23.

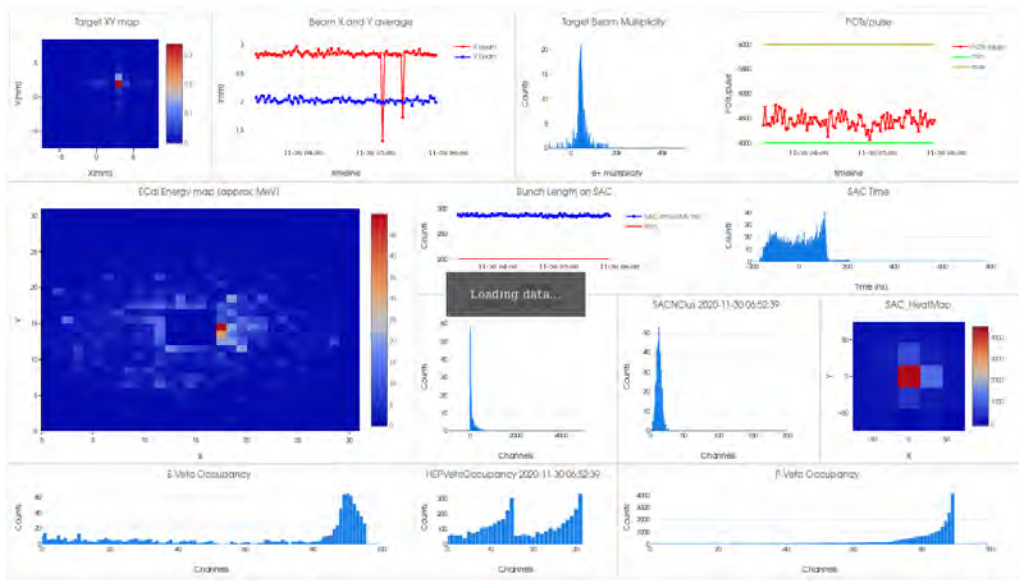


Figure 3.22: Screenshot of detector information from online monitoring system from Run 30660.



Figure 3.23: Screenshot of DAQ and magnet information from online monitoring system from Run 30660.

Chapter 4

Charged Particle Detector Reconstruction

One of the most significant sources of background to the associated production of a dark photon at PADME is Bremsstrahlung events, in which the photon is detected in the ECal and the positron goes undetected. To resolve this problem, both particles need to be reconstructed. For this reason a two-part veto system was created, using the SAC to detect the photon and the PVeto to detect the positron. In order to maximise the efficiency of rejection of Bremsstrahlung photons in the ECal, an efficient reconstruction of particles entering the PVeto is vital.

This chapter presents the reconstruction process developed to optimise the detection of charged particle final states at PADME. This was one of the principle objectives of the work done for this thesis, leading to the physics analysis presented in Chapter 6. This reconstruction was then implemented into the official reconstruction software for Run 2.

The Veto reconstruction is performed in two steps: first, individual “hits” are reconstructed. Hits are signals of particles entering one of the 90 individual plastic scintillator bars. These hits are then grouped into “clusters” which represent the interaction of particles in more than one bar of the detector. Since the expected rate of particles entering each bar is high, the reconstruction uses a “multi-hit” approach, where more than one hit can be assigned to each bar for each bunch.

Figure 4.1 shows a photo of the vetoes inside the vacuum chamber.

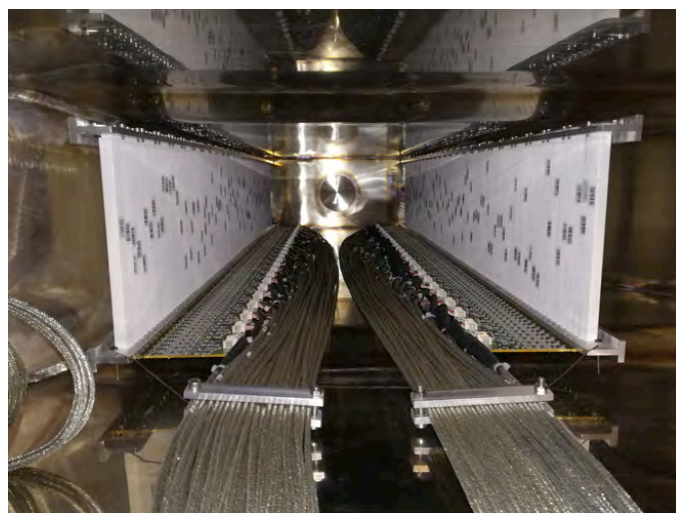


Figure 4.1: Vetoes inside magnetic field. PVeto is on the right, EVeto on the left. Underneath the scintillating bars the front-end electronic readout boards can be seen.

4.1 Overview of the PADME veto detectors

The Positron Veto (PVeto) is complemented by an analogous detector, known as the Electron Veto (EVeto), on the opposite side of the magnetic field in the vacuum chamber. The EVeto was designed with two aims in mind: firstly to allow the detector to be used with either a positron or an electron beam, and, importantly for this thesis, to allow the study of dilepton final states. In the original PADME design, both detectors had 96 scintillating bars. Between Runs 1 and 2, however, it was found that positrons from the beam which lost only a small amount of energy in interactions in the target ended up creating showers in the most downstream bars of the PVeto. Many of these shower particles went on to reach the ECal, creating a significant amount of background, and therefore the last 6 bars of the PVeto were removed. Given that these showers came from beam particles, the EVeto did not suffer from the same problem and so no EVeto bars were removed.

Since the two charged particle Veto detectors are made of the same material and have the same readout system, from the silicon photomultipliers to digitisation of the signal, the reconstruction for both detectors is functionally identical, adjusted only for the different number of scintillating bars in the two detectors and for the different calibration constants necessary to compare reconstructed quantities in each scintillating bar.

It is important to remember, however, that each detector experiences a different rate of particles entering per event, known as the channel ‘‘occupancy’’. This is due to the fact that the only process at PADME able to generate electrons is Bhabha scattering, which has a cross-section orders of magnitude lower than that of Bremsstrahlung, the principle process populating the PVeto. Moreover, the PVeto receives positrons from the ‘‘beam halo’’ - particles which lose energy through the beam transport or arrive out of trajectory and are bent more strongly by the magnetic field.

The respective occupancies for the two Vetoes in the two runs used for the calibration can be seen in Figure 4.2. The PVeto calibration was carried out using Run 30650 which was taken in standard conditions: 430 MeV e^+ beam with a 280 ns long bunch containing 28k positrons. The EVeto calibration relied on a specific run taken at the end of Run 2 in which the magnetic field of the PADME magnet was inverted, sending positrons towards the EVeto side of the experiment. Since the PADME vacuum chamber is asymmetrical, the angular opening of the chamber on the PVeto side, shown in Figure 3.1, does not exist on the EVeto side. For this reason, as well as the fact that the wall of the BTF experimental hall is much closer to the EVeto side, a higher level of backplash was expected in this configuration, both from the chamber and from the wall. For this reason the beam intensity was lowered to approximately 2k positrons on target per bunch (PoT/bunch) instead of the PADME standard of 28k PoT/bunch.

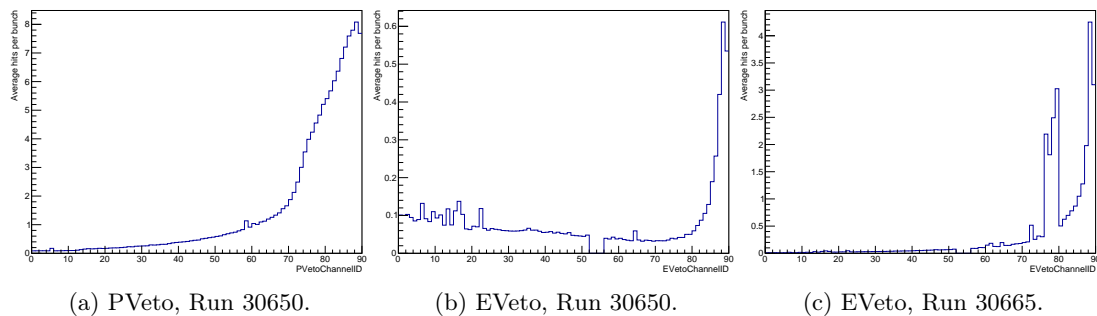


Figure 4.2: PVeto (left) and EVeto (centre) occupancy in Run 30650, and EVeto occupancy in Run 30665 (right). Each channel is a scintillating bar and $ChannelID = 0$ represents the bar closest to the target, while $ChannelID = 90$ is the closest to the ECal. The Y axis is the average number of particles entering the respective channel in a single bunch crossing the target (an ‘‘event’’). Note the difference in Y-axis scale.

Since the software tools used to perform this reconstruction were originally developed for the

PVeto and its 90 channels, only 90 channels were considered in the EVeto reconstruction as well. As is explained in Section 4.2.5 channels with channel number above 70 were not considered for physics analysis in either of the detectors due to the increased occupancy in this region, caused in large part by the beam halo, meaning that the last 6 channels of the EVeto would not have been used in any case.

The spike seen in Figure 4.2c at channels 76-79 may be due to showers caused by a vacuum chamber flange around this region, but again, this is beyond the range of “good channels” considered in physics analyses. The spike is only seen in the inverted magnetic field configuration. The hole in EVeto channels [52,55] is due to the fact that the front end preamplifier boards inside the vacuum chamber stopped working between Run 1 and Run 2. Since it was not possible to recover them, the front end cards were disconnected and their data was not recorded.

4.2 Hit Reconstruction

At PADME, the Veto detectors are digitised using a CAEN V1742 digitizer, at a rate of 2.5 GS/s. This results in the full analogue waveform of each detector being read out for every bunch, with the signal amplitude saved as a 12 bit number at every point in the 1024 sample array. The 12 bits are used to represent a value of voltage in the range 0-1 V, meaning that each bit corresponds to 0.244 mV. The 0 V amplitude is represented by 4095 counts while 1V is represented by 0 counts. This produces the analogue signals which are the starting point for the software reconstruction.

Hit reconstruction is performed directly on these digitised waveforms, aiming to reconstruct accurately and precisely the following three quantities:

- Hit channel: the channel hit by the particle. One channel represents one scintillating bar and Channel 0 represents the bar closest to the Target, while Channel 90 is the closest to the ECal;
- Hit time: the time after the trigger at which the particle arrives in the bar;
- Hit energy: energy deposited by the particle as it passes through the scintillating bar

The hit reconstruction algorithm is structured in five phases:

- In the first phase, signals are screened using a zero-suppression check, to ensure that digitised event windows are not reconstructed if they do not meet a minimum threshold for containing more than electronic noise from the digitiser. This screening finds the RMS of the first 1000 samples of the 1024 sample signal array which contains the signal amplitude in digitiser counts. If the RMS is > 5 counts, the signal is considered non-zero and therefore of interest.
- Once signals have been selected to be of potential interest, the pedestal of the signal is calculated. Since the time delay between the arrival of the trigger and the arrival of the beam is between 200-250 ns, anything that is recorded before this time does not come from the beam and is therefore only due to the pedestal of the detector. For this reason, the average is taken of the first 150 samples (60 ns) of the signal.
- The pedestal is then subtracted from the signal and the resulting signal height is converted from negative digitiser counts to positive mV. In this way the signal is converted from the un-normalised signal, shown for example in Figure 4.3, to the normalised signal shown in Figure 4.4. Note that this signal comes from Channel 89 in the PVeto – the channel with the highest occupancy rate, as seen in the example in Figure 4.2.
- The signal is scaled by a calibration constant defined for each channel to equalise the electronic gain of the silicon photomultiplier.

- Finally the signal is processed using the procedure described in Section 4.2.1.

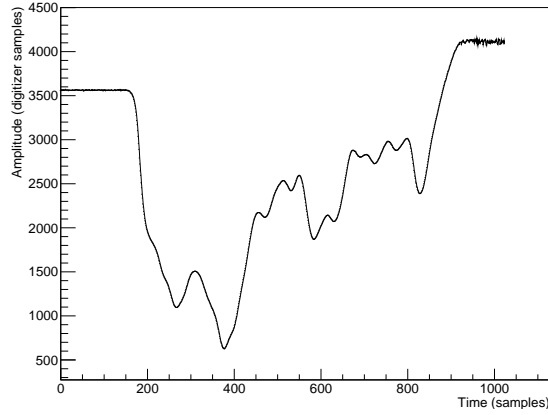


Figure 4.3: Raw signal from V1742 digitizer before normalisation.

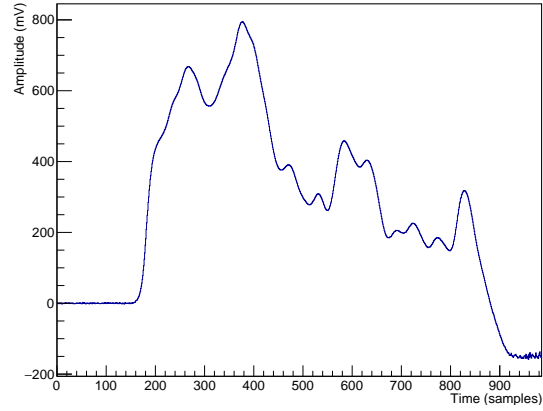


Figure 4.4: Normalised signal, which is processed and passed to TSpectrum.

4.2.1 Signal processing

During hit reconstruction, the digitised signal is passed to the TSpectrum peak-finding method from the CERN ROOT software framework, which searches for gaussian peaks in a spectrum passed as a histogram [99].

In order to make the signal shape more Gaussian, and therefore more easily fitted by TSpectrum, an approximation to the signal derivative is calculated using the following formula:

$$\text{Signal Derivative}[s] = \text{Signal}[s] - \text{Signal}[s - 15] \quad (4.1)$$

where s is the time of the digitised sample under consideration in digitizer counts (~ 0.4 ns).

15 samples $\times 0.4$ ns per sample is almost equal to the rise time, meaning that this procedure retains the rising edge of the signal faithfully but gives a faster descent after the peak than in the raw signal, as can be seen in Figures 4.5 and 4.6. These plots were made using a template of an average signal shape taken from data.

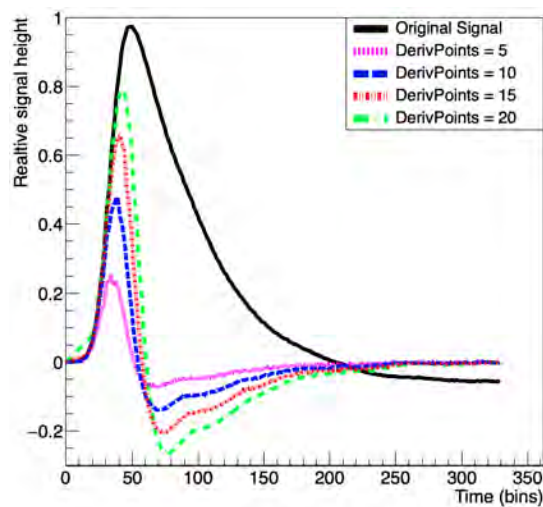


Figure 4.5: Height of original signal compared to height of derivative signals taking the derivative across different numbers of points.

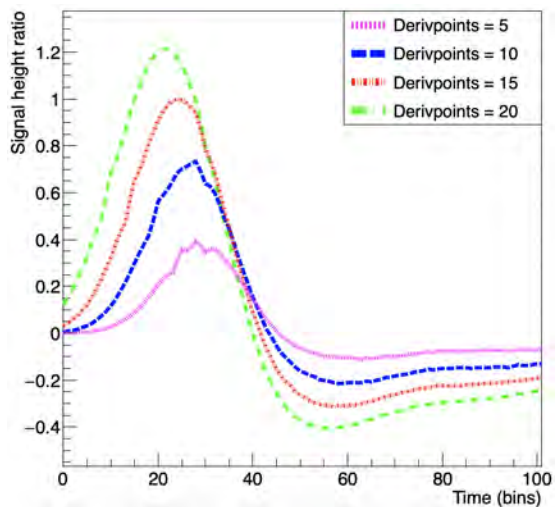


Figure 4.6: Ratio of original signal height to derivative signal height. Note that the x-axis range is smaller than in Figure 4.5

The ideal signal shape after processing would be a Gaussian with amplitude equal to the amplitude of the original signal and a low standard deviation. It can be seen that these requirements are best satisfied by the red curve, which is calculated using Equation (4.1).

Figure 4.7 shows the derivative of the signal from Figure 4.4. Points in which the amplitude is less than 0 have been set to 0 to facilitate the TSpectrum fit. The signals after the derivative processing are narrower and more Gaussian. This treatment therefore improves the separation between hits and reduces the effect of noise on the peak height, which is then used as a measure of the hit energy.

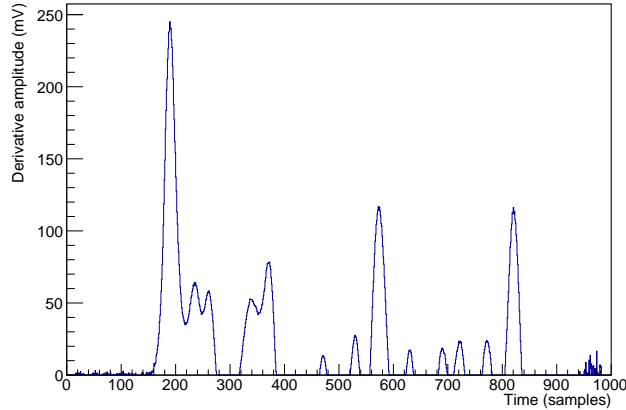


Figure 4.7: Derivative signal, as passed subsequently to the TSpectrum peak search.

4.2.2 TSpectrum hit finding

Once signals have been processed to have a more Gaussian shape, they are passed to TSpectrum which looks for peaks in the signal window. The method takes as input:

- The maximum number of peaks to search for in the signal (*npeaks*);
- The expected standard deviation of peaks (*fPeakSearchWidth*);
- The minimum amplitude allowed for a peak to be considered (*peak_thr*)

The amplitude threshold *peak_thr* is passed to TSpectrum as a fraction of the maximum amplitude of a signal. Therefore, in order to keep the noise threshold constant, *peak_thr* is recalculated for each channel for each event to remove any potential peaks with an amplitude of less than 8 digitizer counts in the raw signal, equivalent to approximately 1.95 mV, or 0.37 MeV released in the scintillating bar. The other parameters are set to *npeaks* = 20 and *fPeakSearchWidth* = 5 ns respectively.

TSpectrum searches for peaks in order of amplitude and performs a Gaussian fit on them. It returns the number of peaks, their amplitude and their position within the digitised window. The position is then transformed from units of sample number within the 1024 sample acquisition window to nanoseconds, and the amplitude is converted from units of derivative digitiser counts to mV, multiplying by 0.046 mV per derivative digitiser count.

The process of gain-equalisation and the finding of the calibration constants to convert from derivative digitiser counts to mV is described in section Section 4.2.3.

Figure 4.8 shows the peaks found by TSpectrum in the sample signal shown above.

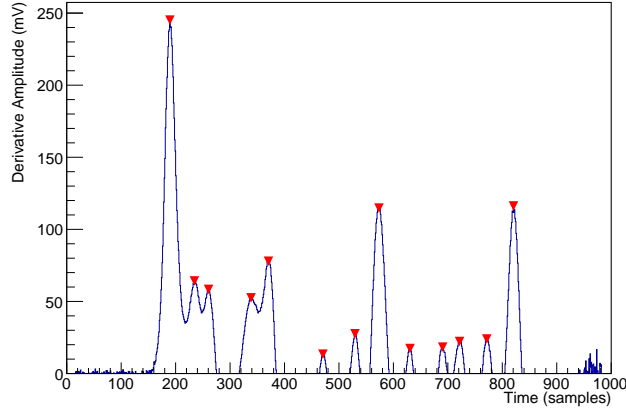


Figure 4.8: Derivative signal with markers on peaks found by TSpectrum.

4.2.3 Gain Equalisation

At energies relevant to PADME, electrons and positrons in the Veto plastic scintillator bars act as minimum ionising particles. The average energy released in each bar is a function only of the average distance traversed in that bar by the particle.

Since the bars are thin compared to the distance to the target, it is a reasonable assumption that on average particles will traverse the same distance in each bar, meaning that the energy released will on average be the same.

Given that the TSpectrum reconstruction includes an amplitude threshold below which signals are not considered, it is important that any difference in the gain of the SiPMs is compensated for offline by finding calibration constants which bring the amplitude spectra of each channel into alignment.

To equalise the gain of the Veto channels, histograms were created containing the amplitude of the derivative of signals in single-hit events, and the peak of these amplitudes was fitted using a Gaussian approximation to give the average amplitude for hits in each channel before equalisation.

This technique was more challenging in approximately the first 20 channels, which have a very low multiplicity due to kinematic and acceptance constraints. In addition, the final 10 channels have such a high multiplicity that it was difficult to find events with only one hit. This does not pose a significant limitation however, since only channels within the range 31-70 were considered in the Bhabha scattering analysis, and kinematic and geometrical factors limit the trajectories of Bremsstrahlung positrons such that they arrive after channel 20.

For the EVeto, the data used for this process came from Run 665 in which the field of the PADME magnet was reversed, sending positrons into the EVeto and allowing for a sufficient rate of particles in each channel to perform the analysis.

The use of the derivative amplitude was validated by studying the ratio of the peak amplitude of the signal derivative, as found by TSpectrum, to the amplitude of the raw signal at the point where the TSpectrum finds the peak on the derivative. This point is on the rising edge of the raw signal as shown in Figure 4.5 and is therefore less sensitive to noise than the peak of the raw signal. Figure 4.9 shows that, to within 5%, the ratio of the rising-edge amplitude to the TSpectrum amplitude is constant, giving confidence in the use of the TSpectrum amplitude as a measure of energy.

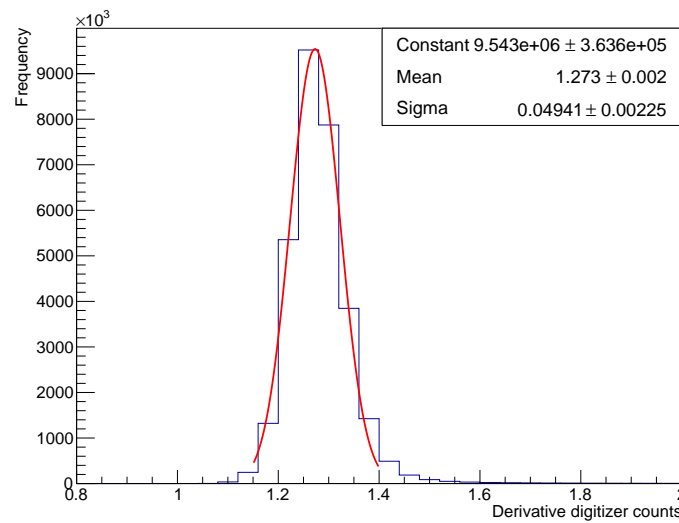


Figure 4.9: Ratio of height of signal rising edge to peak amplitude found by TSpectrum.

Figure 4.10 shows the mean of the Gaussian fit of amplitudes, taken from signals which contain exactly one hit. The average amplitude across channels is 33 derivative counts, which is biased low by channels below 20 and above 80. Therefore equalisation constants were found to bring the average amplitude of each channel to 35 derivative counts, as shown by the red line. It can be seen that PVeto channels 58 and 60 have particularly low gain, worsening the signal/noise ratio in these channels. The detached EVeto channels (channels 52-55) have been omitted.

Figure 4.11 shows the distribution of TSpectrum amplitudes of one-hit events from all channels combined, with a Landau fit. The shoulder at low amplitudes in the EVeto is probably due to the closed shape of the vacuum chamber and its position close to the wall of the BTF, producing more back-splash which results in showers of photons entering the vetoes. This was foreseen before the run with the inverted magnetic field, and it is for this reason that the intensity for this run was lower than average.

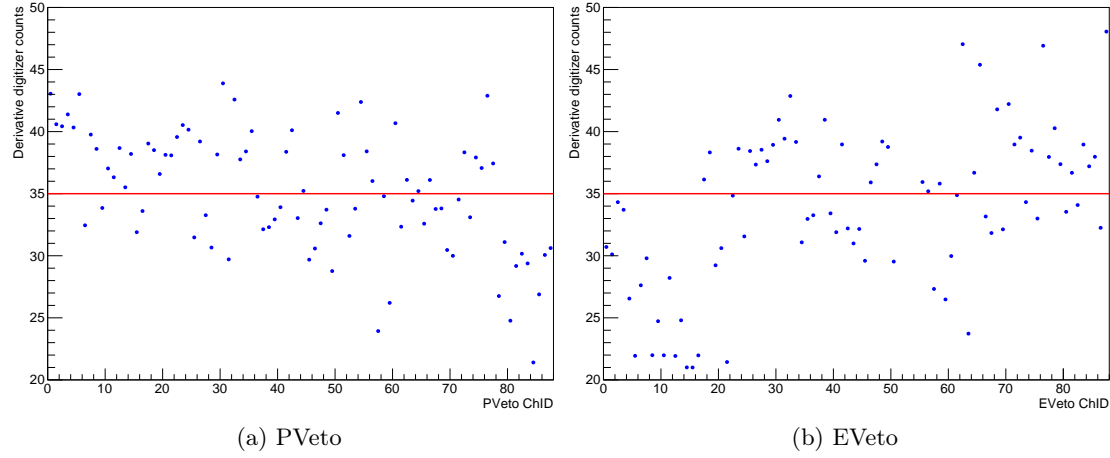


Figure 4.10: Average TSpectrum amplitude for one-hit events for each channel in the PVeto (left) and EVeto (right), before gain equalisation. The red line shows amplitude = 35 derivative counts.

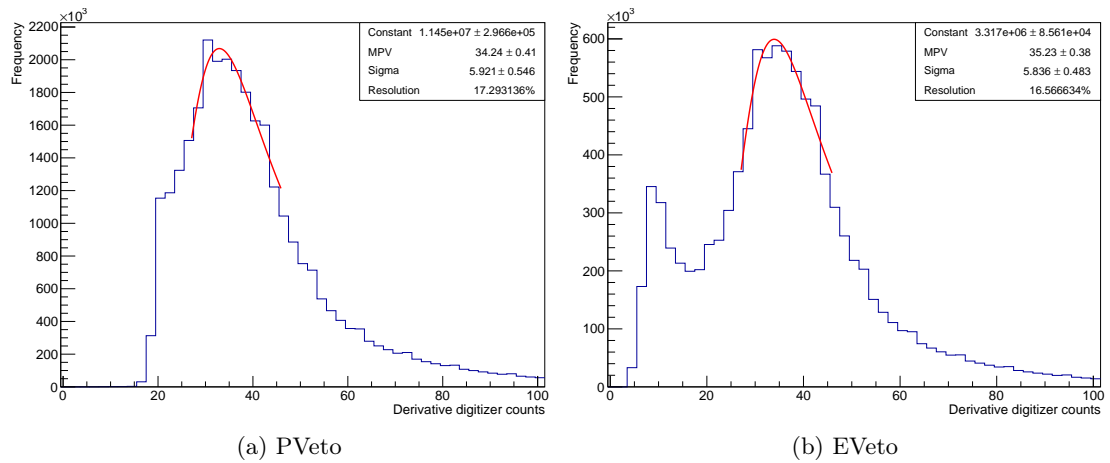


Figure 4.11: TSpectrum amplitude of one hit events in the PVeto (left) and in the EVeto (right), before gain equalisation. Resolution here is defined as $\frac{\sigma}{MPV}$.

Once the calibration constant was found for each channel, it was applied to the raw digitised signal before the derivative was taken and passed to TSpectrum. Figure 4.12 shows the average amplitude per channel after channel equalisation, and Figure 4.13 shows amplitudes for all one-hit events after equalisation. The improvement in the reconstruction is measured by the resolution, as given by the ratio $\frac{\sigma}{MPV}$ of standard deviation to the most probable value of the Landau fit. In the PVeto, the resolution improves from 17% to 15%, while in the EVeto the improvement is from 17% to 13%.

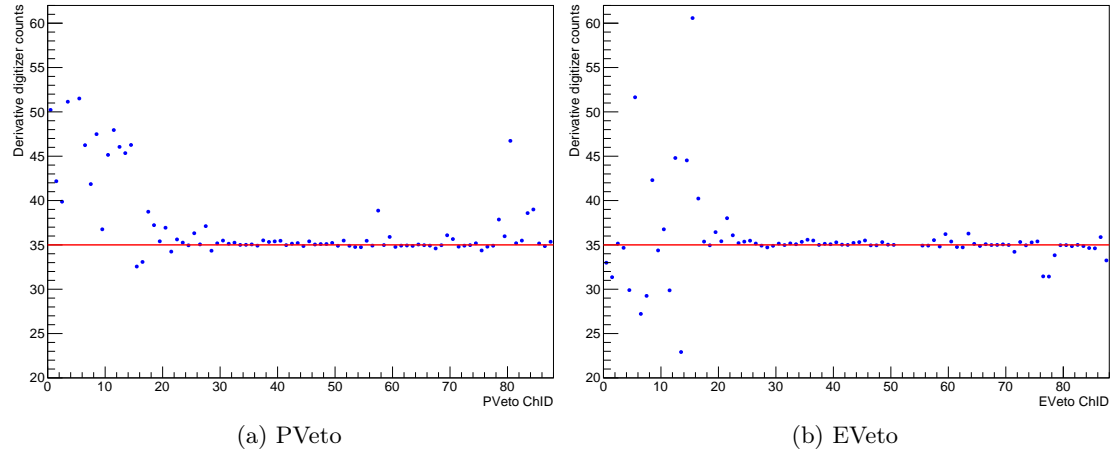


Figure 4.12: Average TSpectrum amplitude for one-hit events for each channel in the PVeto (left) and EVeto (right), after gain equalisation. The red line shows amplitude = 35 derivative counts.

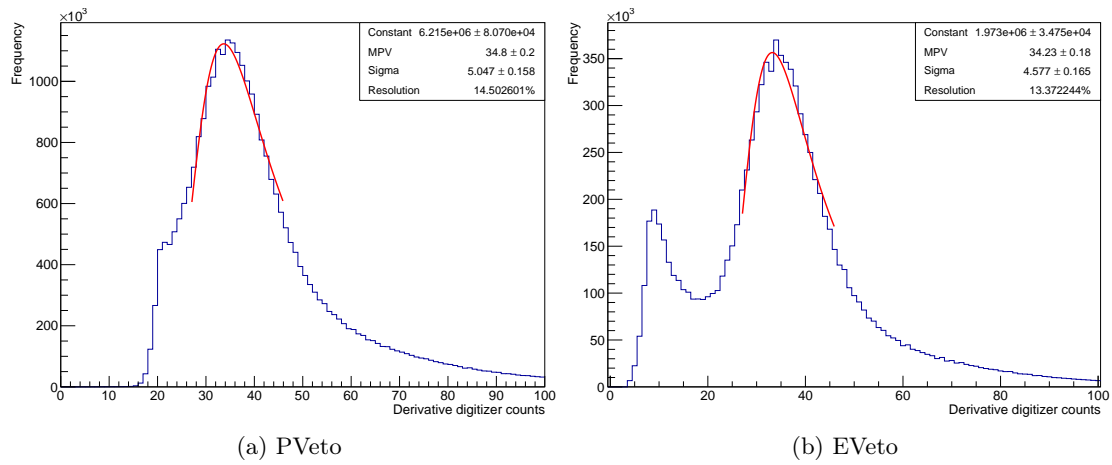


Figure 4.13: TSpectrum amplitude of one hit events in the PVeto (left) and in the EVeto (right), after gain equalisation. Resolution here is defined as $\frac{\sigma}{MPV}$.

4.2.4 Tail correction

In addition to the gain equalisation, the long decay time $\tau \sim 20$ ns of the signal shape poses a potential problem to the energy reconstruction of hits in the vetoes, as the amplitude of hits which arrive on the tail of previous signals would be changed artificially, as shown in Figure 4.14. Moreover, as can be seen here, the tail eventually drops below zero, meaning that even signals which arrive a long time after a previous signal will still have their amplitude altered.

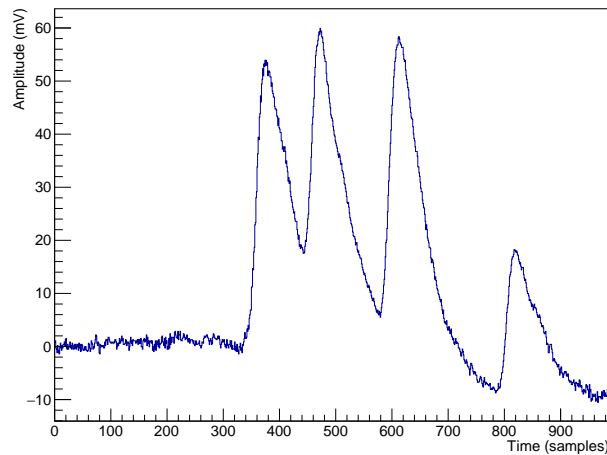


Figure 4.14: Example signal where the amplitude of one hit is changed by the fact that it arrives before the previous exponential has dropped to 0.

While the use of the derivative makes the decay time of the signal fitted by TSpectrum shorter, the problem of the negative tail persists in the derivative, as can be seen in Figure 4.5. For this reason, the fractional height of the derivative of signals was studied as a function of the time after the arrival of a previous hit. Thus for each hit after the first in time, the amplitude found by TSpectrum was adjusted using the following equation:

$$V_i = A_i - V_{i-1} \times f(t_i - t_{i-1})$$

where V_i is the adjusted amplitude of hit i , A_i is the un-adjusted amplitude as found by TSpectrum, V_{i-1} is the adjusted amplitude of the previous hit and $f(t_i - t_{i-1})$ is the fractional height of the $i - 1$ th signal at the time of arrival of the i th hit. Figure 4.15 shows the amplitude of hits in the PVeto before and after this correction, while Figure 4.16 shows the amplitudes in the EVeto.

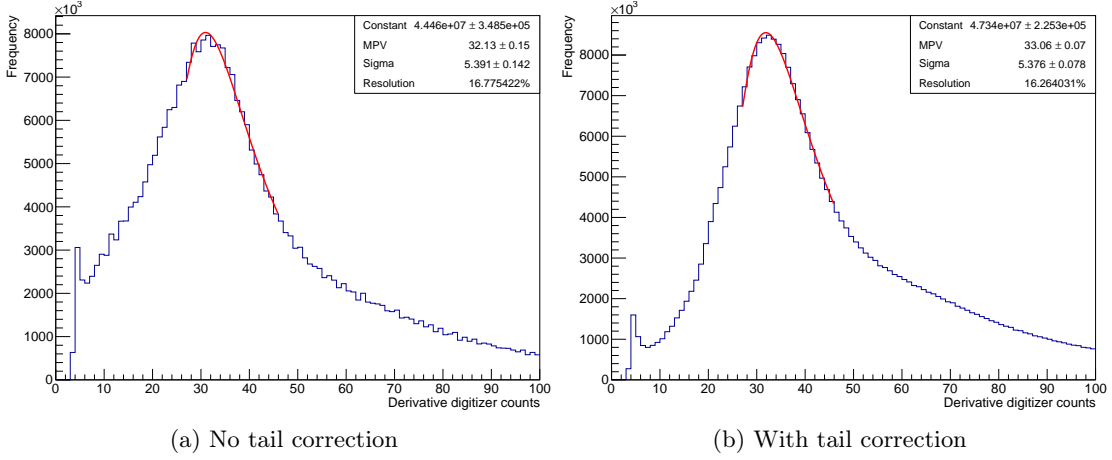


Figure 4.15: Amplitude of all PVeto hits without (left) and with (right) tail correction. Resolution is defined as $\frac{\sigma}{MPV}$.

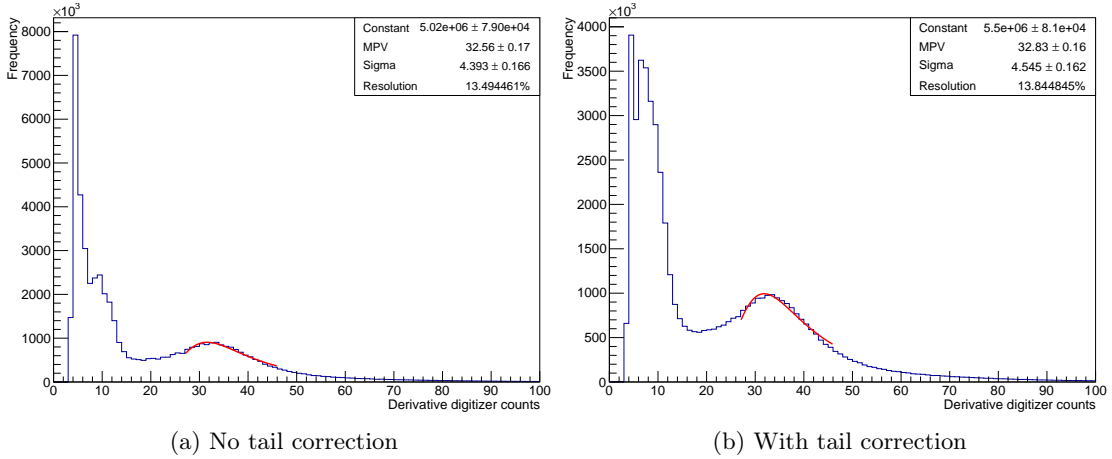


Figure 4.16: Amplitude of all EVeto hits without (left) and with (right) tail correction. Resolution is defined as $\frac{\sigma}{MPV}$.

It can be seen here that the resolution improves in the PVeto, while for the EVeto the peak in Figure 4.16b is more symmetrical than in Figure 4.16a. In the EVeto the resolution remains relatively unchanged. This is due to the fact that the tail correction improves the amplitude reconstruction for hits after the first in events which contain more than one. Since channels in the EVeto typically receive fewer than one hit per event on average, there are few hits for which the tail correction was applied.

4.2.5 Time synchronisation

The time of arrival of a signal at the PADME digitisers is due to two main factors: the time of flight of the particles and the delay caused by cables and front end electronics. The time of flight depends on the trajectory the particle takes between the Target and the detector and can be computed using the Monte Carlo simulation, so that Data-MC difference shows only the delay due to cables and electronics.

The SiPMs of the Veto channels are connected to the digitiser using two different lengths of cables for each detector: in the PVeto, the 48 channels closest to the target used 2.5 m long

cables, while the others used 2 m cables. In the EVeto the cables were 2 m and 1.5 m in length respectively. The EVeto cables are shorter than the PVeto cables since the feed-through vacuum flange is downstream on the EVeto side.

To get an empirical estimate of the delay caused by the combination of cables and other detector effects, the time difference between positrons arriving in the Vetoes and photons arriving in the SAC was studied in both data and Monte Carlo. This method was used since the principle physical process in both detectors is Bremsstrahlung, causing a strong correlation in time between them.

It was therefore assumed that any difference between the time reconstructed in the data and that expected from the Monte Carlo was due only to cables and other hardware effects, or due to the data reconstruction. For example, using the time of the derivative peak as the time of the hit instead of the time at which the signal starts to rise, or the time of the peak of the raw signal, will yield a value of time which differs by a constant.

The Monte Carlo sample used for this calibration simulated the whole beam line from the Mylar window separating the BTF vacuum from the PADME vacuum (see Section 3.1). More information about the beam line simulation can be found in [89].

Symmetry between the PVeto and the EVeto was assumed, meaning that the time of flight for Bremsstrahlung positrons was the same in both detectors, allowing the standard Monte Carlo sample to be used to calibrate the EVeto.

Figure 4.17 shows the average time difference between clusters in the Vetoes and clusters in the central channel of the SAC, channel 22. The Veto clusterisation process is described in Section 4.3 while detail of the SAC reconstruction and clusterisation is given in Section 4.4. Figure 4.18 shows the mean difference per channel for the “good channels”, channels 20 to 70, with two linear fits to the two different distributions. This definition of “good channels” was used because above channel 70 the occupancy becomes too high for the Veto reconstruction to be reliable, and because it is kinematically impossible for Bremsstrahlung positrons to enter the detector acceptance with such little energy as to be deflected into channels before channel 20. This kinematic constraint results in an extremely limited number of clusters in the first 20 channels in the Monte Carlo, leading to the extremely large error bars seen in Figures 4.17 and 4.20, where the error bars are given by the sigmas on the fit of the difference in time between the Veto and the SAC.

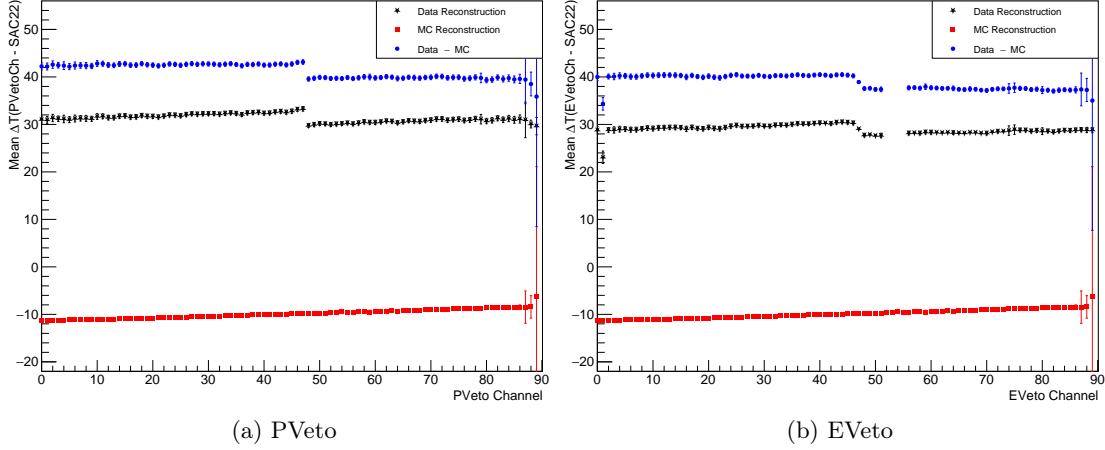


Figure 4.17: Mean time difference between Veto clusters and SAC clusters before time equalisation, for all Veto channels. The black stars are the mean values of $\Delta T(PVetoCh - SAC22)$ for each channel in data, the red squares are Monte Carlo (MC) and blue dots are the difference between data and MC.

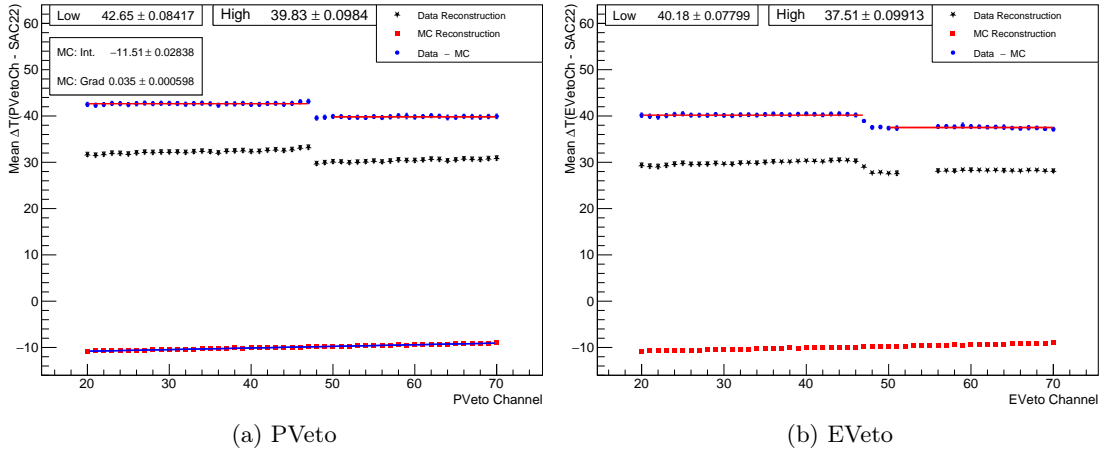


Figure 4.18: Mean time difference between Veto clusters and SAC clusters before time equalisation, for "good" Veto channels (from channel 20 to channel 70). The black stars are the mean values of $\Delta T(PVetoCh - SAC22)$ for each channel in data, the red squares are Monte Carlo (MC) and blue dots are the difference between data and MC. The two blue distributions are fitted separately with a constant, shown as "Low" for the channels between 20-47 and "High" for the channels from 50-70. The red distribution has been fitted as a single straight line with y-intercept "MC. Int" and gradient "MC. Grad".

The two distinct distributions, coming from the two different cable lengths used in each Veto, can be seen more clearly in Figure 4.19, which shows $\Delta T_{Data} - \Delta T_{MC}$, where ΔT is the difference in time between Veto clusters and SAC clusters. Since the cables are flat multiwire cables, the length of the cable for each group of cables is exactly identical. This means that difference in the value of $\Delta T_{Data} - \Delta T_{MC}$ found from channel to channel within the same group is due to uncertainties in the method. Therefore, the two regions in each detector, marked as "Low" and

“High” respectively in Figure 4.18, were fitted with a single constant each, and the value from this fit was assigned as the constant time difference due to the cable.

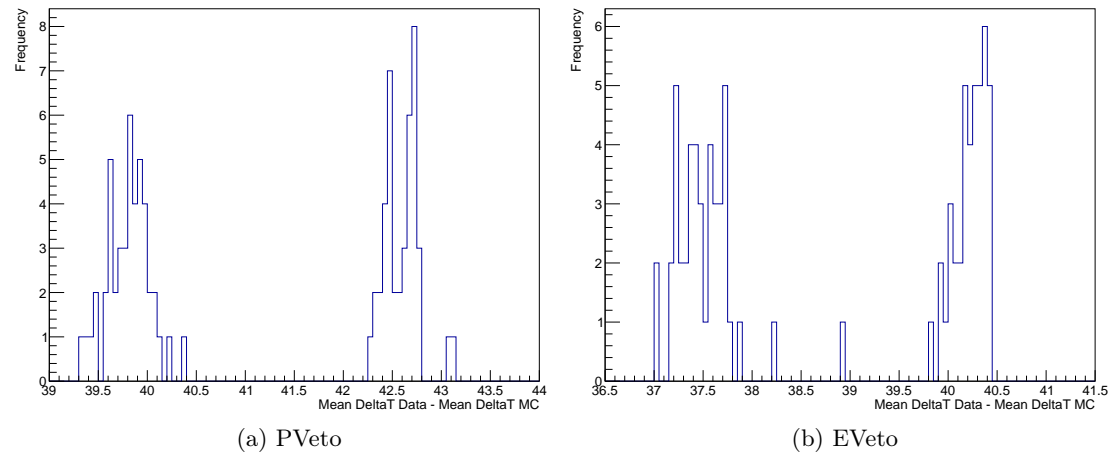


Figure 4.19: Histogram of the difference between the mean time difference between Veto clusters and SAC clusters in data and Monte Carlo, before time equalisation, for all PVeto Channels.

As can be seen in Figures 4.20 and 4.21, once the time equalisation constants have been applied, the data and the Monte Carlo agree well. The fact that the correction works so well in the EVeto gives confidence in the idea that beam is well centred on the target and has a very low angle to the z-axis – if this were not the case the gradient of the time of flight as a function of channel number would be different between the PVeto and the EVeto and the resulting subtraction would not give a flat line for the EVeto.

Figure 4.21 also shows that the correction in the PVeto leads to two distributions which are each relatively linear but are not perfectly centred on 0. However, noticing that the errors on the points here represent the sigmas of the fit on each channel, it can be seen that all of the points are compatible with 0. This shows that the difference between the “Low” and “High” distributions and 0 is negligible compared to the resolution of the reconstruction.

Figure 4.22 shows that once the cable lengths have been corrected for, correcting for the time of flight of Bremsstrahlung positrons as shown in Figure 4.21 gives a resolution of ~ 0.5 ns.

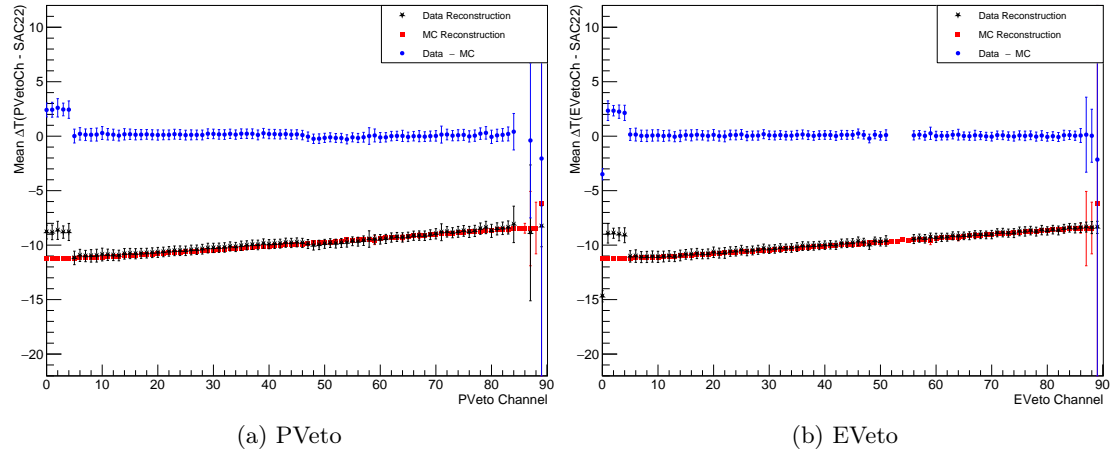


Figure 4.20: Mean time difference between Veto clusters and SAC clusters after time equalisation, for all Veto channels. The black stars are the mean values of $\Delta T(PVetoCh - SAC22)$ for each channel in data, the red squares are Monte Carlo (MC) and blue dots are the difference between data and MC.

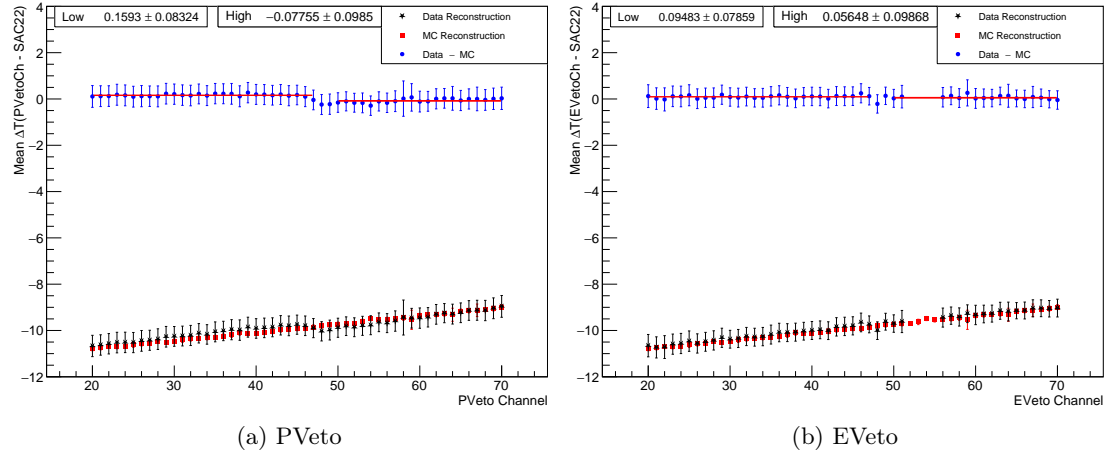


Figure 4.21: Mean time difference between Veto clusters and SAC clusters after time equalisation, for "good" Veto channels (from channel 20 to channel 70). The black stars are the mean values of $\Delta T(PVetoCh - SAC22)$ for each channel in data, the red squares are Monte Carlo (MC) and blue dots are the difference between data and MC.

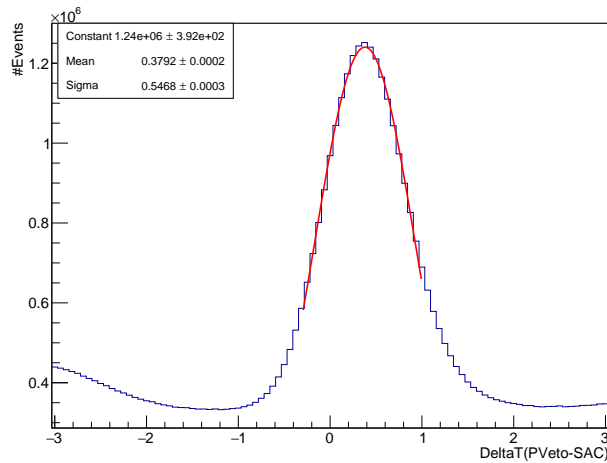


Figure 4.22: $\Delta T(PVeto - SAC)$ for good channels, after correcting for cable lengths and Bremsstrahlung time of flight.

4.2.6 Validating the calibration

The performance of the time and energy calibration mechanisms was evaluated by applying the calibration constants which had been found from Run 30650 to the data from Run 30540. These two runs, taken approximately one month apart, are considered “good for physics”, since both have approximately 27k positrons on target per bunch and stable data taking conditions. As can be seen in Figure 4.23, the corrections derived from Run 30650 also improve the amplitude resolution in Run 30540.

Unfortunately, since only one run has been taken with the magnetic field reversed, such a cross check could not be done for the EVeto, however the stability of the PVeto reconstruction provided confidence in the EVeto reconstruction as well.

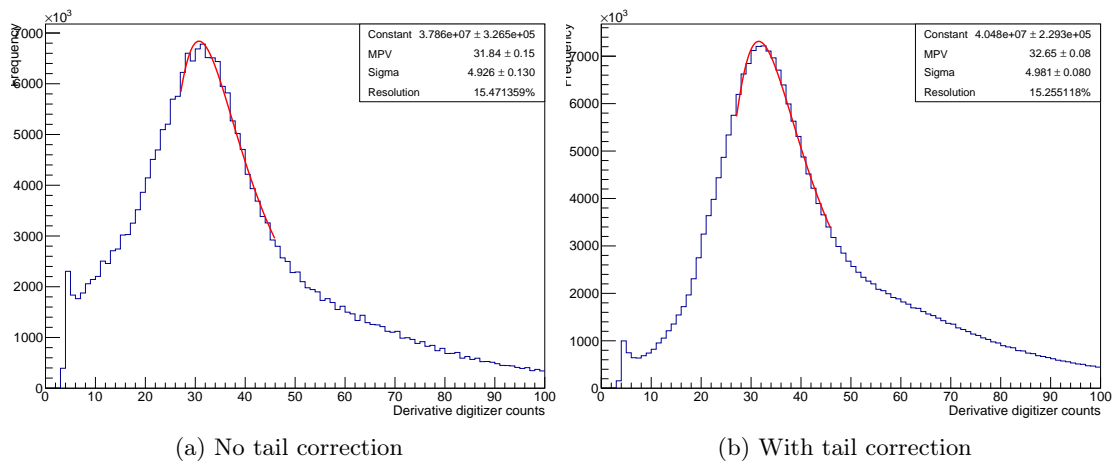


Figure 4.23: Amplitude of all PVeto hits without a and with (b) tail correction.

4.3 Cluster Reconstruction

Due to the geometry and kinematics of the experiment, some particles will pass through multiple channels in the Vetoes before exiting the detector, as shown in Figure 4.24. This causes hits to be created in multiple neighbouring channels, which need to be clustered together to give a good reconstruction of the original particles.

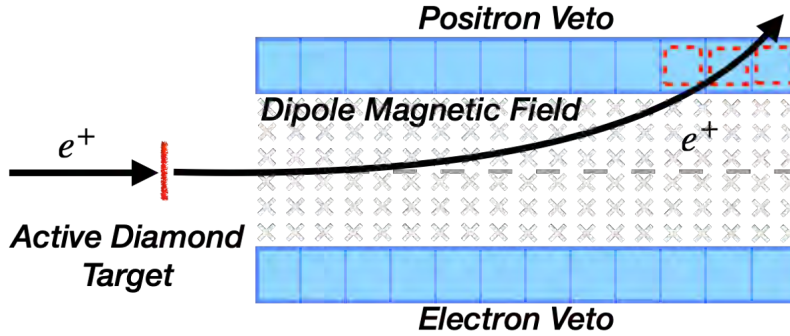


Figure 4.24: Example of trajectory causing hits in more than one channel.

After hit reconstruction, hits are sorted first by channel number and then by increasing time. For the clusterisation, all hits are placed into a single structure and sorted only by time. The first hit to be considered creates a “cluster” by itself. The second hit is then compared to the first cluster. If they are in nearest-neighbouring channels and within 2 ns of each other, the second hit is clustered with the first, with time given by the average of the two times and energy by the sum of the individual energies. The geometrical limits of the cluster are also saved as the “MostUpstreamChannel” and the “MostDownstreamChannel”.

If the second hit does not satisfy the requirements to be clustered with the first, a new cluster is created containing just this hit. The algorithm continues like this, clusterising new hits with old clusters if they are within 2 ns of the cluster time and either immediately upstream of the “MostUpstreamChannel” or immediately downstream of the “MostDownstreamChannel”, until all hits have been considered.

Since the time resolution of the detector is larger than the time taken for particles to go from one channel to the next, hits which are adjacent in time are not necessarily in adjacent channels. This leads to potential splitting of clusters, as can be seen in Figure 4.25a. For this reason, after the initial clusterisation stage, an analogous process is undertaken to merge clusters which have been split artificially, resulting in the unified cluster seen in Figure 4.25b.



(a) Individual clusters before merge.



(b) Single cluster after merge.

Figure 4.25: Cluster merging process. The numbers represent the order of detected arrival time of individual hits.

4.4 Bremsstrahlung reconstruction

Since the main purpose of the Veto detectors is to veto positrons coming from Bremsstrahlung, the performance of the offline software reconstruction was evaluated by studying Bremsstrahlung events detected in the Vetoes and in the SAC.

The SAC reconstruction, like that of the Vetoes, relies on TSpectrum to identify peaks in the digitised signal. Unlike in the Vetoes, however, the energy of photons in the SAC is determined by integrating the height of the signal within 2 ns before and 2 ns after any peak is found. More information about the characterisation of the SAC can be found in [92], and its performance is discussed in the PADME commissioning paper [95]. Once hits are found in the SAC they undergo a clusterisation process where the energies of participating hits in nearest-neighbour crystals are summed to give the energy of the cluster, and time is given by the energy-weighted mean of the times of hits.

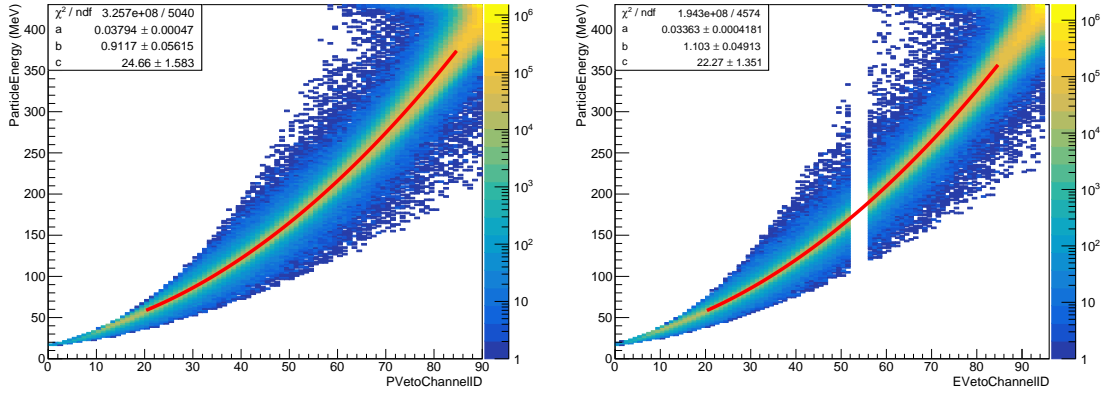
Once the time detected in the Vetoes was converted into a time comparable with that of other detectors according to the process described in Section 4.2.5, it was possible to search for

Bremsstrahlung events using the SAC and the Vetoes.

Since the Monte Carlo simulation retains the truth-level information about each vertex through all the reconstruction and analysis processes, it was possible to determine which Veto channels ended up being hit by positrons coming from Bremsstrahlung vertices, thereby creating a relation between positron energy and eventual Veto channel. Fitting the 2D histogram of impact channel vs Bremsstrahlung positron energy it was found that the energy, E , is a function of channel, Ch , such that:

$$E = 24.66 + 1.09117 \times Ch + 0.03794 \times Ch^2$$

This function is overlaid on the 2D histogram in Figure 4.26.



(a) Energy of positrons deflected into each PVeto channel

(b) Energy of positrons deflected into each EVeto channel, assuming reversed magnetic field

Figure 4.26: Impact channel of Bremsstrahlung positrons as a function of positron energy, fitted with second-order polynomial $ax^2 + bx + c$.

Using the function shown in Figure 4.26a to reconstruct the energy of positrons which are in time within 1 ns with a cluster in the SAC, the energy resolution of the sum of the energies of the positron and the photon is $\sim 9\%$, as seen in Figure 4.27a. The fact that the mean of the distribution is higher than the beam energy is probably due to pileup in the SAC. Since the energy of a SAC cluster is the integral of all pulse heights within ± 2 ns of the peak time, if several particles enter in this time, the pulse height will be artificially increased, causing an increase in reconstructed energy. This hypothesis is supported by the fact that in Run 30660, which was taken at 4.6×10^3 positrons on Target per bunch, the average sum of the energies is reduced from 453 MeV to 443 MeV, as seen in Figure 4.27b. If the difference were due to pile-up in the Vetoes, the energy should be reduced in high pile-up conditions. This due to the fact that the clusterisation algorithm assigns the most upstream channel to the cluster, which would correspond to a lower energy, as seen in Figure 4.26a.

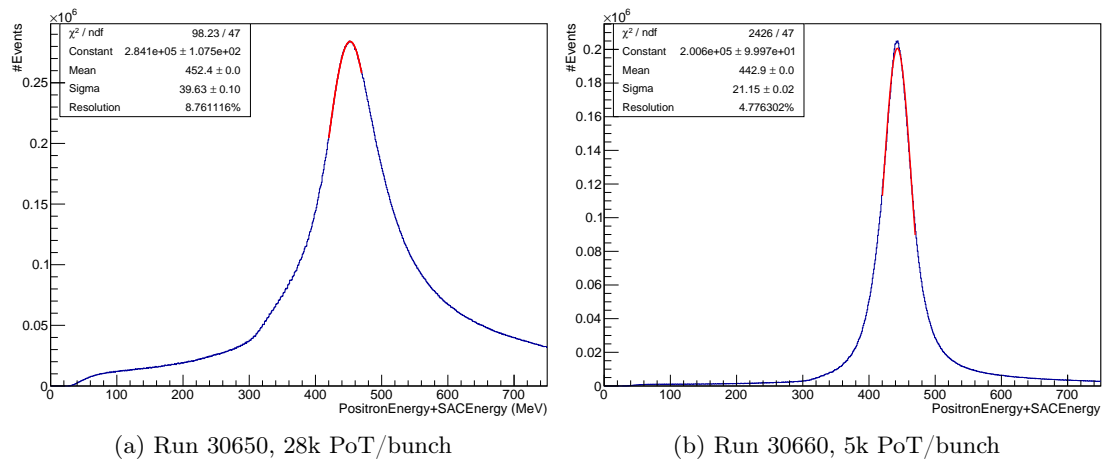


Figure 4.27: Sum of energies of clusters in the SAC and positrons in PVeto, given by the function seen in Figure 4.26a, for clusters which are in time within 1 ns between SAC and PVeto in Run 30650 (left), taken at 28k PoT/bunch, and in Run 30660 (right), taken at 5k PoT/bunch.

Chapter 5

Neural network based veto reconstruction

In 2020, a neural network-based method of reconstruction was studied on the basis of Run 1 and Run 2 data, to determine whether such a method could lead to improved reconstruction efficiency. At the time of development, there was no way to include this type of algorithm in the software framework of PADME, and therefore work on the method was paused in favour of the “standard” software based approach discussed in Chapter 4. Since this time, however, the PADME group based in Sofia, Bulgaria have won a European Research Council grant to study the use of machine learning and neural network tools in the reconstruction at PADME. As part of this work they are studying the interface between the standard C++-based PADME framework and the infrastructure used in the neural network tools. This opens the way to the possibility of incorporating the work described in this chapter in future versions of the PADME software framework.

The scope of the studies described in this chapter is limited to improving the counting of hits in the Vetoes, particularly in situations of high pile-up. The work described here started before the end of Run 2 and therefore before the specific beam conditions of 2020 data had been studied. Figure 5.1 shows the distribution of the number of clusters entering the PVeto in data from Run 1 (2019). It is important to note that since this time, both the hit reconstruction and the clusterisation algorithms have been updated, and that, as described in Chapter 3, the beam conditions were significantly improved in Run 2, leading to much lower-background conditions in the data studied in this thesis. It is clear to see from Figure 5.1, however, that the reconstruction in 2019 was not able to cope with the high rate of particles entering the Veto, and that the reconstruction was systematically underestimating the number of particles arriving. These were the conditions of the reconstruction when this work was started and what this work was intended to improve. The significant difference in the expected occupancy of different channels of the vetoes means that it was very important to ensure that this reconstruction method was able to reconstruct events with few hits per event as well as events with more hits, with good efficiency in both cases. Efforts to this effect are discussed in Section 5.8 and Section 5.9.

Since data-taking was still underway while the neural-network studies were being performed and at the time of writing no interface exists between neural-network tools and the standard PADME software framework, the shape of pulses in many of the simulated data samples used to train the network was not optimised to reflect the real data in the first samples studied. Given that at the time the studies were done the neural network tools could not be used with the standard PADME software framework, not all studies were repeated with data-based signals. Nevertheless, the work done in this chapter can be understood as “proof of concept”, that a well-trained neural network can have a higher efficiency in reconstructing hits in the PADME veto detectors than the pure C++-based TSpectrum method.

Section Section 5.1 describes the simulation of “toy” Monte Carlo signals created using two different analytical functions as a first estimate to replicate the pulses found from data. After

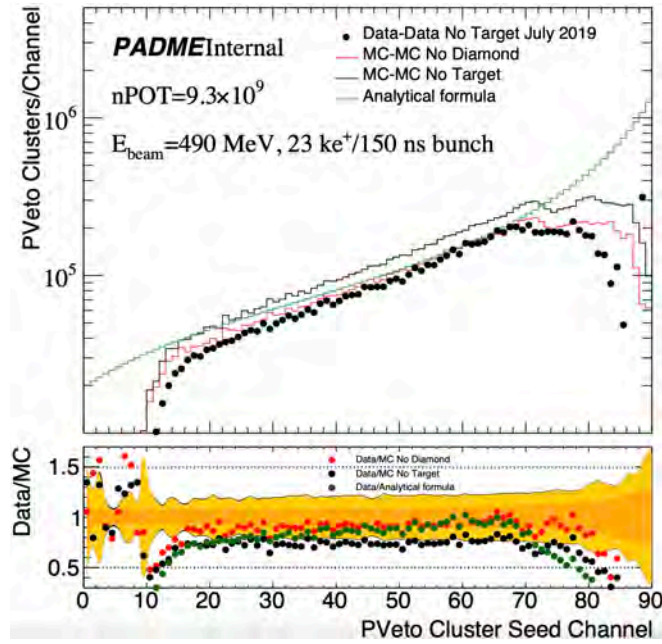


Figure 5.1: Number of clusters detected in each Veto channel in Run 1 (black points), compared with the number expected from the Monte Carlo without the diamond target, but with the PCB target support (red line), and without both the target and its support (black line), and with the analytical expectation from Bremsstrahlung positrons [90]. Plot created using the reconstruction as of 2019.

the end of Run 2, pulse shapes taken from real data could be used as a template to train a neural network, as discussed in Section 5.2. Section 5.3 describes the concept of using a convolutional neural network (CNN) to reconstruct the number of hits in an event, and Section 5.4 shows the results of a CNN trained on a sample of standard signals.

To test the hypothesis that the neural network learned to recognise the rise-time of the pulse, pulses were produced with different rise times and neural networks were trained and tested on these samples. Section 5.5 discusses the results from signals with a 5 ns rise time, while Section 5.6 presents studies of 10 ns rise time signals. In Section 5.7, studies are discussed in which the amplitude of pulses was fixed, in order to study the effect of variable amplitudes on the neural network reconstruction.

Since it was hypothesised that a network trained on a more challenging but related problem would be more efficient at reconstructing an easier problem, a network was trained on a sample of events which had 5 hits per event, instead of the standard 3 hits per event. Results from this study can be seen in Section 5.8. The effect on reconstruction efficiency of the distribution of number of hits per event is studied further in Section 5.9, where a model is trained on a sample of uniformly distributed hits per event and used to reconstruct the standard 3 hit per event sample and the 5 hit per event sample.

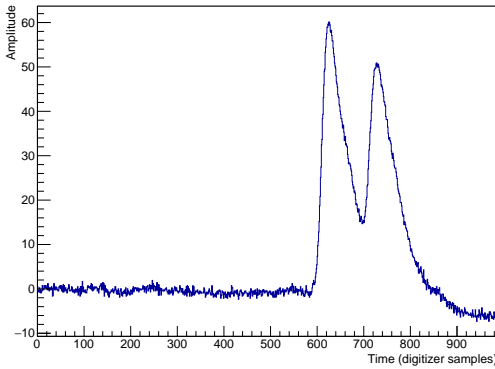
In Section 5.10 results are shown from tests using pulses with an exponential rise shape, intended to simulate more faithfully real pulses than the standard pulses which have a linear rise.

Section 5.11 discusses the possibility of finding a neural network architecture which is able to reconstruct all channels of the Veto efficiently event if they haven't been equalised to the same average amplitude. Finally, Section 5.12 shows results from a network trained and tested on simulated signals coming from a real pulse shape from data.

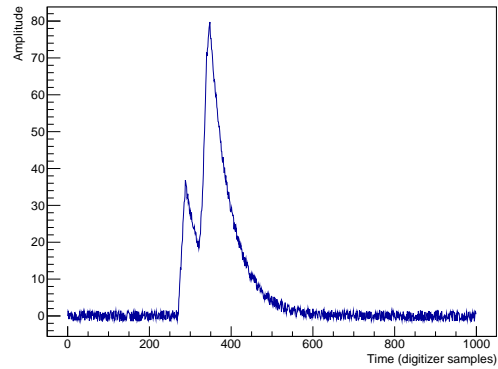
5.1 Signal simulation: Toy MC signals

It is important to train the network on a data sample which reflects the reality of the problem. Signals were simulated in two ways: first using a toy Monte Carlo signal generator (Section 5.1), with two different pulse shapes: using a linearly rising slope, and using an exponential. These tests were used as proof of principle while Run 2 was still ongoing. After the end of Run 2, signals were simulated using the average shape of pulses from real Run 2 data from PVeto and HEPVeto channels (Section 5.2).

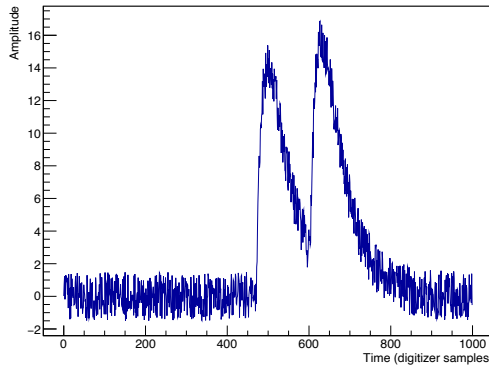
In order to test the behaviour of the reconstruction methods under different simulated conditions, a number of different types of simulations were produced. This was particularly important in understanding which parameters were recognised by the neural network and therefore under which conditions this form of reconstruction is likely to be most accurate.



(a) Real data signal from PVeto channel 67, from Run 30205.



(b) Simulated signal using linear rise



(c) Simulated signal using exponential rise time

Toy Monte Carlo signals were simulated according to the following method. The number of hits per bunch was generated randomly according to a Poisson distribution with mean $\lambda = 3$, and each hit was assigned a randomly generated amplitude which followed a Landau distribution with MPV = 50 mV and $\sigma = 12$ mV, to which was added noise generated randomly in the interval $U[-1.5, 1.5]$ mV. To simulate the 200 ns bunch length inside the 400 ns digitiser window, the arrival time of each hit was simulated with a uniform distribution inside the window $U[80, 280]$ ns. Hits were then ordered in time before the generation of the waveform. All random variables were calculated using the CERN ROOT TRandom3 package [99] using the system time in UTC as a seed.

The standard pulse shape of the signal used a linear 7 ns rise time followed by an exponential decay with $\tau = 20$ ns (Figure 5.2b) to simulate the detector response.

The height of the pulse was then calculated at each sample of the 1024-sample digitizing window, and the height in digitizer counts at each sample was recorded in a both a ROOT

TTree and a .txt file. The the .txt file was passed to the convolutional neural network (CNN) described in Section 5.3, while the ROOT file was used both for the TSpectrum reconstruction as in Section 4.2 and to use as the "truth" level data against which the reconstructed data was compared.

Variations on the standard sample included:

- Reducing the rise time of the signals to 5 ns (Section 5.5)
- Increasing the rise time of the signals to 10 ns (Section 5.6)
- Fixing the amplitude of created signals to 50 mV (Section 5.7)
- Increasing the mean number of hits per event to 5 (Section 5.8)
- Using a sample of events with a uniformly distributed number of hits between 0 and 13 (Section 5.9)
- Using an exponential rise time as well as an exponential fall time (Figure 5.2c), so that the waveform was given by

$$V(t) = -1 \times \exp\left(-\frac{t}{\tau_{Rise}}\right) + \exp\left(-\frac{t}{\tau_{Fall}}\right)$$

where $V(t)$ is the height of the signal at time t , τ_{Rise} is the 7 ns rise time and τ_{Fall} is the 20 ns decay constant (Section 5.10)

- Using a different, randomly generated constant $\sim U[0.7, 1.3]$ for each of the 90 channels of the PVeto and randomly assigning one of these 90 channels to each event. This was intended to reflect the fact that the respective gains of each of the channels had not yet been equalised. (Section 5.11)

5.2 Signal simulation: Data-averaged signals

After the end of Run 2, the studies described here were repeated on signals generated from the average shapes of pulses in the PVeto. In order to create a template of an average pulse, a simple algorithm was designed to search for peaks. Using the data from Run 30552, the derivative of the signal at a given sample was approximated by taking the signal height at the next sample of the data window and subtracting the height at the previous sample:

$$\text{SignalDerivative}[s] = \text{SignalHeight}[s + 1] - \text{SignalHeight}[s - 1]$$

The RMS of the derivative of the pedestal was calculated on the negative pulses from the first 50 samples of the acquisition window, and a peak was then found in a region where the average of 20 consecutive samples was less than $-0.5 \times \text{RMS}$. The “t0” of the peak is the point at which the derivative is the lowest in the 30 consecutive samples following the first sample in which the previous condition is met.

If only one peak was found in the event, the baseline was set to 0 by subtracting the RMS from the signal, the signal was normalised by dividing by the maximum amplitude and the window between `sample[t0-30]` and `sample[t0+299]` was saved. Once all of the single-hit events in the run were found and saved for each channel, the average of the pulses in each of these channels was found and saved in the form of a TGraph for each channel in a root file. The average shape of these pulses can be seen in Figure 5.3.

Once the template was extracted, signals were simulated according to the method described in Section 5.1, substituting the algebraically-defined pulse shapes with a shape taken from the TGraph root file. Signals could be generated using the same channel from the root file for all events, or for a different, randomly selected channel each event, in order to give the neural network the widest variety of signals to learn from. An example event is shown in Figure 5.3.

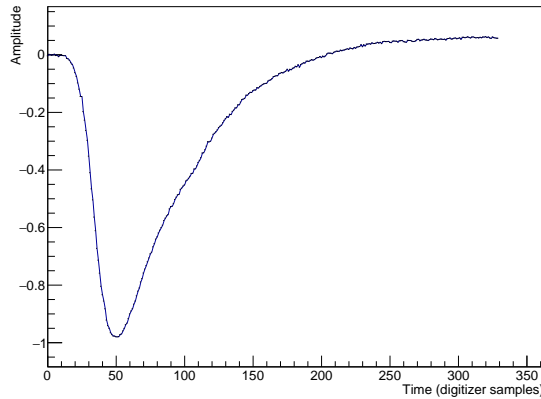


Figure 5.3: Average pulse shape of signals in PVeto Channel 0.

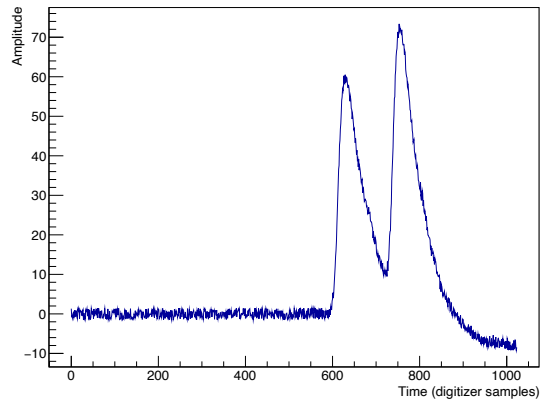


Figure 5.4: A simulated event using the average shape of real Veto pulses.

5.3 Multi-hit reconstruction using a convolutional neural network

The reconstruction method discussed here made use of a convolutional neural network (CNN) model. The network was trained to identify the number of hits in a simulated event using a training sample of 200×10^3 simulated events and a validation sample of 100×10^3 events. Testing was done on a sample of 200×10^3 independent events. The training, validation and testing process was run separately for each type of simulation listed in Section 5.1.

The input to the network was the signal height at each of the 1024 digitiser samples, and the network was trained to minimise the categorical cross-entropy loss function:

$$L_i = - \sum_{j=1}^N t_{i,j} \log(p_{i,j})$$

where N is the total number of events in the sample, p is the number of hits predicted by the network, t is the true number of hits, j is the event being analysed and i is the iteration of the network.

Table 5.1 shows the architecture of the CNN used to reconstruct events with a linear rise time. For “standard events” with 3 hits per event, the CNN used 3 convolutional blocks (highlighted in red) and a dropout layer of weight 20% between the two final densely connected layers, meaning that a randomly selected 20% of neurons after the penultimate layer were set to zero and not used in the final layer.

Model: "VGGLike_CNN"			
	Layer (type)	Output Shape	Param #
	input_1 (InputLayer)	[(None, 1024, 1)]	0
Convolutional Block 1	Conv_1 (Conv1D)	(None, 1022, 16)	64
	leaky_re_lu (LeakyReLU)	(None, 1022, 16)	0
	MaxPool_1 (MaxPooling1D)	(None, 511, 16)	0
Convolutional Block 2	Conv_2 (Conv1D)	(None, 509, 16)	784
	leaky_re_lu_1 (LeakyReLU)	(None, 509, 16)	0
	MaxPool_2 (MaxPooling1D)	(None, 254, 16)	0
Convolutional Block 3	Conv_3 (Conv1D)	(None, 252, 32)	1568
	leaky_re_lu_2 (LeakyReLU)	(None, 252, 32)	0
	MaxPool_3 (MaxPooling1D)	(None, 126, 32)	0
	Flatten (Flatten)	(None, 4032)	0
	Dense_1 (Dense)	(None, 64)	258112
	ReLU_dense_1 (ReLU)	(None, 64)	0
	dropout (Dropout)	(None, 64)	0
	Dense_2 (Dense)	(None, 64)	4160
	ReLU_dense_2 (ReLU)	(None, 64)	0
	Output (Dense)	(None, 14)	910
=====			
Total params: 265,598			
Trainable params: 265,598			
Non-trainable params: 0			

Table 5.1: Architecture of convolutional neural network used to analyse events with a linear rise time.

The parameters of interest in this reconstruction were the efficiency, defined as the number of events reconstructed correctly as a fraction of the total number of reconstructed events and the minimum difference in time ΔT_{min} between hits for which the reconstruction was accurate in $> 95\%$ of events. All errors reported in this chapter are purely statistical.

5.4 Standard signals

The results discussed in this section are of the reconstruction of standard signals (Section 5.1) using a model trained specifically for these signals (Table 5.1), compared to the TSpectrum reconstruction discussed in Section 4.2.

Figure 5.5 shows the number of hits per event simulated by the toy Monte Carlo (yellow), and reconstructed using TSpectrum on the derivative (black) and by the CNN (red). The bottom plot shows the efficiency of reconstruction as a function of the true number of hits generated.

It was assumed that any reconstruction method was likely to be able to distinguish pulses which are well separated in time. To find the minimum time difference ΔT_{min} between two hits for which events were reconstructed accurately, the minimum time difference between any two hits in an event was plotted in Figure 5.6 for all events (yellow) and for events in which the correct number of hits was reconstructed by the CNN (red) and using the TSpectrum reconstruction (black). The plot is limited to $\Delta T_{min} < 25$ ns. The bottom plot shows the reconstruction efficiency as a function of ΔT_{min} . The threshold of separability was considered to be the minimum ΔT at which 95% of events were reconstructed accurately, shown by the blue line.

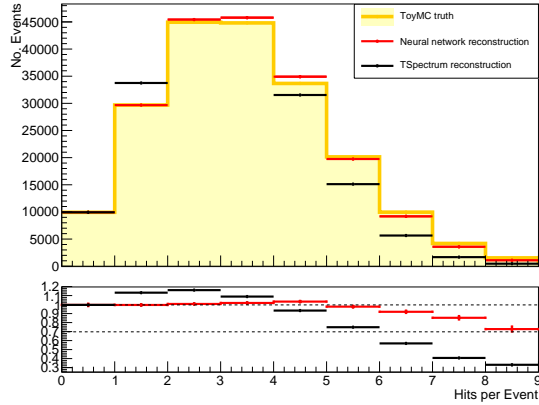


Figure 5.5: Number of hits per event created and reconstructed under standard simulation conditions.

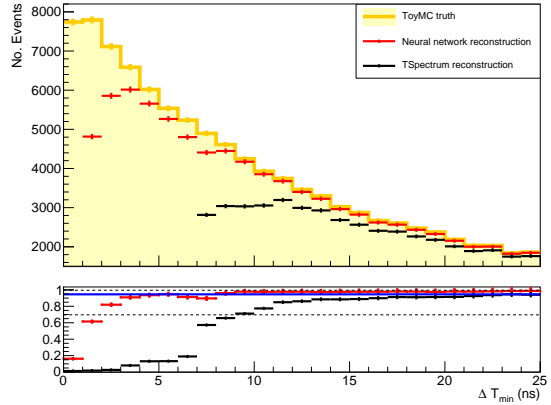


Figure 5.6: Minimum difference in time between hits in the same event for simulated events and events correctly reconstructed, under standard simulation conditions.

It can be seen from Figure 5.5 that with an efficiency of 92%, the neural network gives a much more faithful reconstruction of the number of hits in an event than the TSpectrum reconstruction, which gives an efficiency of 72%. It can also be seen from Figure 5.6 that the 95% separability threshold is reached at $\Delta T_{min} = 8$ ns for the neural network compared to $\Delta T_{min} > 20$ ns for the TSpectrum reconstruction, and even for events with hits separated by $\Delta T_{min} < 7$ ns, the reconstruction efficiency is very high. It is interesting to note the dip in reconstruction efficiency for hits separated by $\Delta T_{min} \approx t_{rise}$, where t_{rise} is the rise time of the signal. This suggests that the neural network is able to identify the rising edge of the pulse and use that as a tool to identify different hits.

This hypothesis was tested in the following two studies, described in Section 5.5 and Section 5.6 respectively, where the rise time was changed in order to see whether this dip moved according to the rise time of the pulses.

To explain the non-negligible efficiency of the reconstruction for events where $\Delta T_{min} < t_{rise}$, the hypothesis that the network was able to learn and use the average pulse amplitude was tested by creating a set of signals with a fixed 50 mV amplitude, to which was added the standard uniform noise. The results are discussed in Section 5.7.

5.5 Signals with 5ns rise time

Maximum efficiency for signals with this reduced rise time was given by adding a 4th convolutional block to the network. This gave an overall efficiency of 96%.

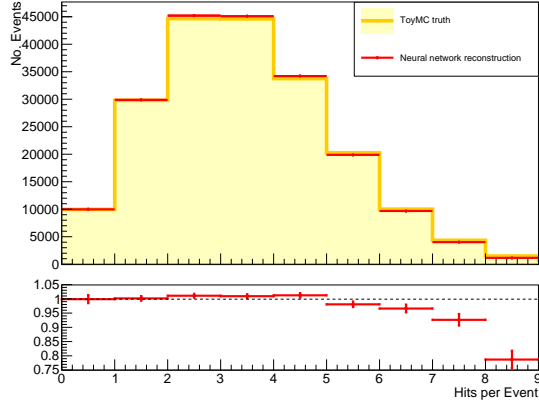


Figure 5.7: Number of hits per event created and reconstructed for events with 5ns linear rise.

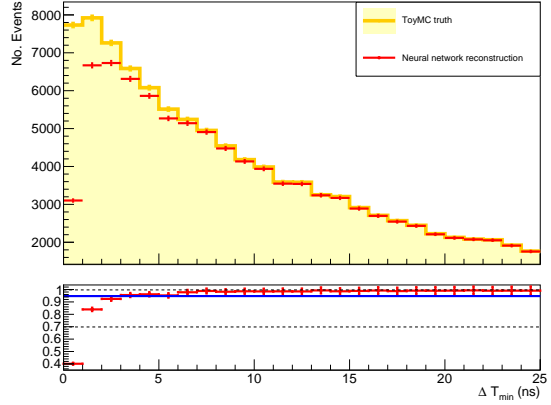


Figure 5.8: Minimum difference in time between hits in the same event for simulated events and events correctly reconstructed, events with 5ns linear rise.

It can be seen from Figure 5.8 that the dip in efficiency has moved to the 5ns bin, supporting the hypothesis that this dip is due to the difficulty in reconstructing hits which are separated by $\Delta T \approx t_{rise}$. It is worth noting the 4 percentage point increase in efficiency of this reconstruction compared to the reconstruction of standard signals. It is logical that the increase in efficiency and the decrease in significance of the dip around the rise time are correlated, due to the fact that for the same number of hits on average arriving inside a time window of equal width, it is less probable that the hits are separated by less than the 5 ns t_{rise} compared to the 7 ns t_{rise} .

5.6 Signals with 10ns rise time

To achieve a network with a comparable efficiency to that used for the standard signals, 3 convolutional blocks were used and the dropout was reduced from 20% to 5%. Under these conditions, the efficiency reached was 93%.

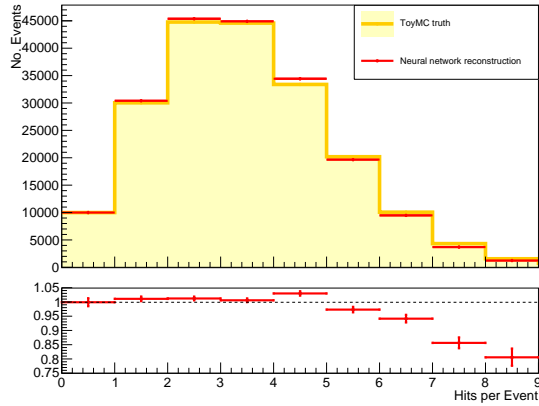


Figure 5.9: Number of hits per event created and reconstructed for events with 10ns linear rise.

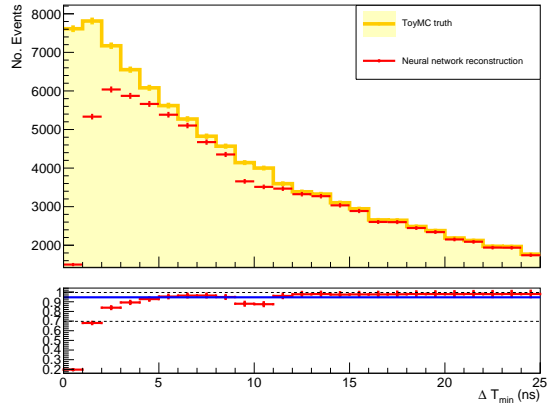


Figure 5.10: Minimum difference in time between hits in the same event for simulated events and events correctly reconstructed, events with 10ns linear rise.

From Figure 5.10 the efficiency dip has clearly moved from around 7ns for the standard signals to be at approximately 10ns, again supporting the idea that the neural network recognises the rising edge of the signal and uses it to separate one pulse from the next.

5.7 Signals with amplitude fixed at 50mV

To investigate the possibility that the network was able to learn and recognise the average pulse height, a network was created with the same architecture as used for the standard signals and trained on a sample of events in which each hit was created an amplitude of 50mV, to which was added uniformly distributed random noise in the interval $U[-1.5,1.5]$. The overall efficiency reached was above 99.9% .

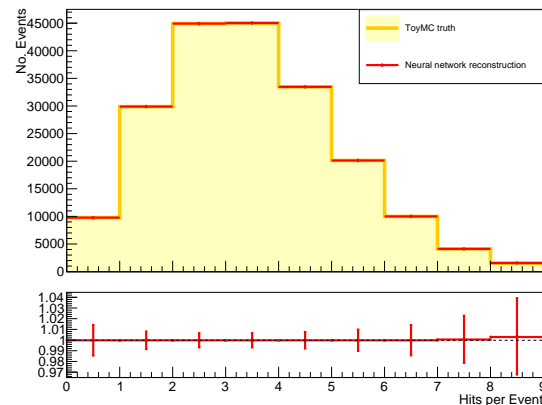


Figure 5.11: Number of hits per event created and reconstructed for events with fixed amplitude.

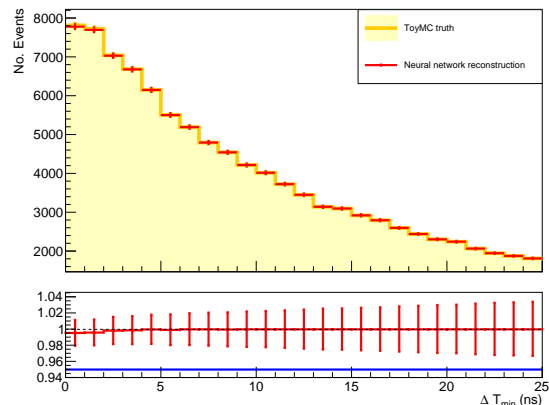


Figure 5.12: Minimum difference in time between hits in the same event for simulated events and events correctly reconstructed, events with fixed amplitude.

These results support the idea that the network is able to learn the amplitude of hits and use this to distinguish them.

5.8 Model trained on signals with mean 5 hits per event

As has been discussed both in Chapter 4 and earlier in this chapter, different channels of the Vetoes are subjected to different rates of particles entering. In order to simulate this effect and to see whether it was possible to find a single architecture of the CNN able to reconstruct signals from all Veto channels, a network was trained on a sample of events created with an average of 5 hits per event and used to reconstruct signals with an average of 3 hits per event.

5.8.1 Signals with mean 5 hits per event

Analysing samples created with an average of 5 hits per event with the network trained on this type of event gives an overall efficiency of 91%.

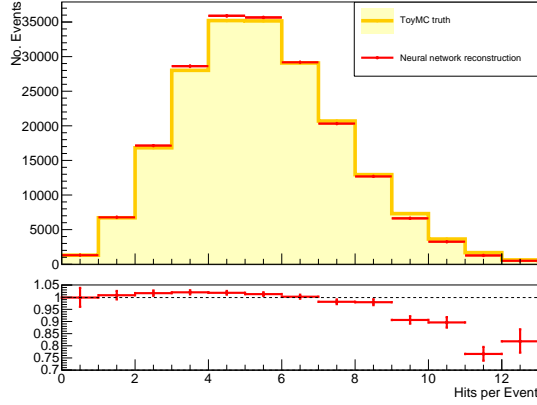


Figure 5.13: Number of hits per event created and reconstructed for events with mean 5 hits per event.

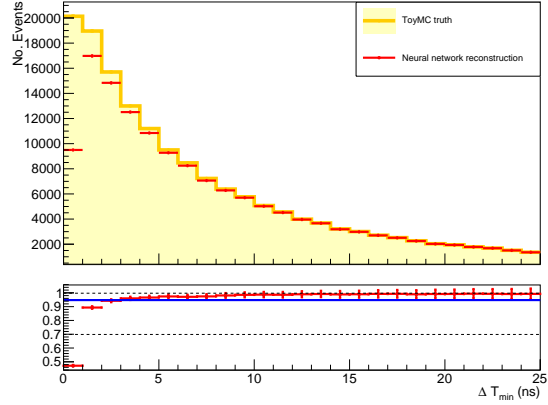


Figure 5.14: Minimum difference in time between hits in the same event for simulated events and events correctly reconstructed, events with mean 5 hits per event.

Using this model, separability of pulses is already reached at $\Delta T_{min} = 3\text{ns}$, which is a significant improvement on the results from the standard signals. This reconstruction also avoids the dip in reconstruction which is seen when using models trained on data with an average of 3 hits per event, as shown in Sections 5.4 and 5.6.

5.8.2 Signals with mean 3 hits per event

Using the model trained on data with an average of 5 hits per event to reconstruct standard signals with a mean of 3 hits event resulted in an efficiency of 97%.

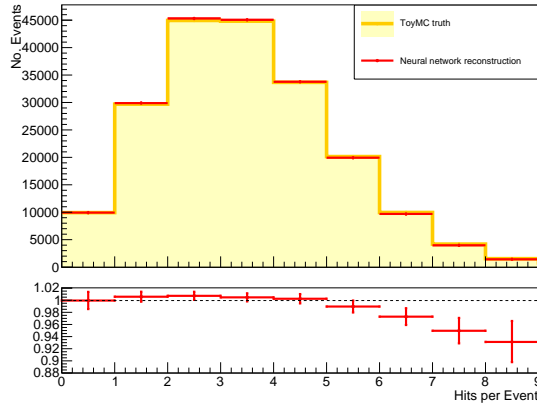


Figure 5.15: Number of hits per event created and reconstructed for standard events reconstructed with 5 hit per event model.

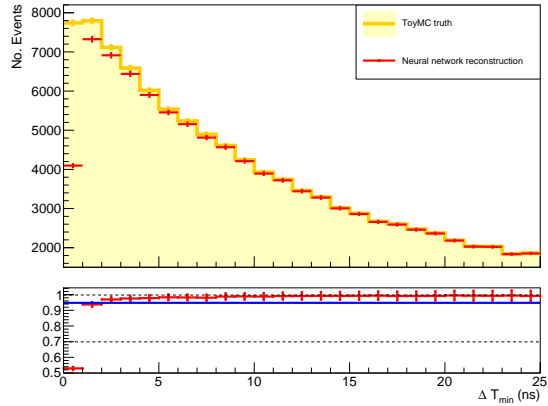


Figure 5.16: Minimum difference in time between hits in the same event for simulated events and events correctly reconstructed, standard events reconstructed with 5 hit per event model.

It can be seen that having trained a model to efficiently reconstruct events with an average of 5 hits per event, this same model can be used with very high efficiency to reconstruct events with an average of 3 hits per event, giving separation from $\Delta T_{min} = 2\text{ns}$ and avoiding the dip in reconstruction efficiency seen in the reconstruction of events using models trained on events with average 3 hits per event, as seen in Sections 5.4 and 5.6.

It should be noticed in addition that the network is able to reconstruct events with higher numbers of hits per event ($\text{No. True Hits} \geq 9$) with much higher efficiency than in the standard model. It is interesting to note that this is true both in the reconstruction of the standard 3 hit

per event samples, where the global efficiency of 97% is significantly higher than the standard model efficiency of 92%, and in the 5 hit per event reconstruction where the global efficiency is slightly lower than for the standard model, at 91%. This is likely due to the fact that the neural network is exposed more often to events with high numbers of hits per event, which are more complex to reconstruct than those with fewer hits per event.

5.9 Model trained on signals with uniformly distributed hits per event

To expand on the study outlined in Section 5.8.2, a network was trained on events where the number of hits per event was generated according to a uniform distribution in the range $U[0,13]$. It was then used to reconstruct three types of data: data with hit numbers following the uniform distribution (Section 5.9.1); data with an average of 5 hits per event (Section 5.9.2) and the standard samples with average 3 hits per event (Section 5.9.3). The optimal reconstruction was reached using 6 convolutional blocks and dropout 15%.

5.9.1 Signals with uniformly distributed hits per event

Using this model to reconstruct signals with a uniformly distributed number of hits per event, the overall efficiency reached 81%.

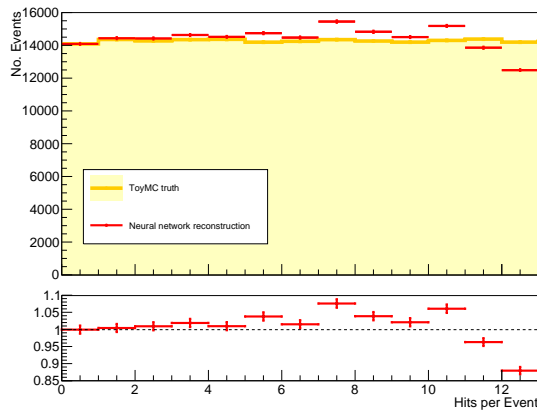


Figure 5.17: Number of hits per event created and reconstructed for events with uniformly distributed hits $\sim U[0,13]$.

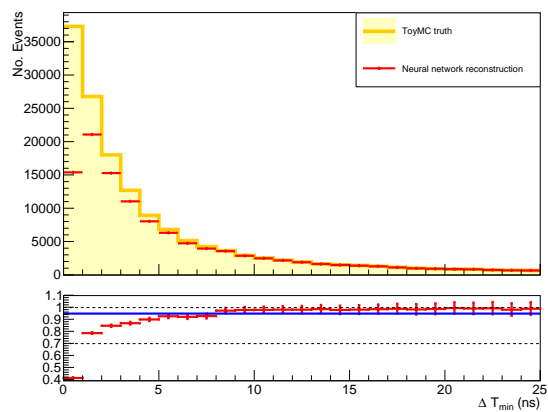


Figure 5.18: Minimum difference in time between hits in the same event for with uniformly distributed hits $\sim U[0,13]$.

It can be seen here that although the model is trained to reconstruct data with exactly this profile, the difficulty in finding an architecture to provide a highly efficient reconstruction means that although the ratio of number of hits reconstructed to true number of hits per event shown in Figure 5.17 is extremely flat compared to Figure 5.5, hits which arrive with $\Delta T_{min} < 7\text{ns}$ are separated with a much lower efficiency than for the standard reconstruction (Compare Figure 5.18 and Figure 5.6).

5.9.2 Signals with mean 5 hits per event

Using the model trained on samples with uniformly distributed events to reconstruct events with average 5 hits per event resulted in an overall efficiency of 89%. This is slightly lower than for the network trained with 5 hits per event (see Section 5.8.1), probably due to an incorrect probability profile being learned by the neural network.

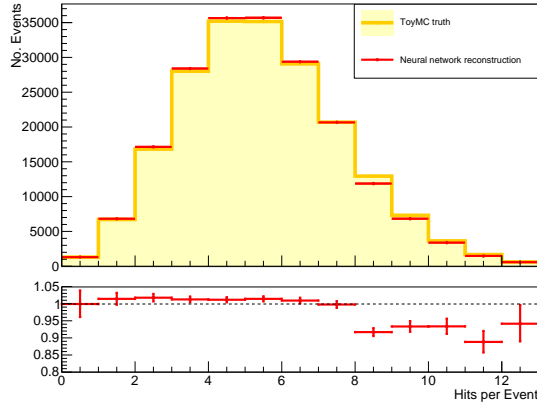


Figure 5.19: Number of hits per event created and reconstructed for events with mean 5 hits per event reconstructed with the uniform distribution neural network.

Again, despite the flatter profile of the ratio of hits per event reconstructed to the truth, the lower global efficiency of the network leads to separability occurring slightly later compared to the reconstruction of 5 hit per event data using the 5 hit per event model (Figure 5.14). Given that events with more hits per event are more likely to have hits arriving closer in time, it is likely that the difficulty in reconstructing events with more hits is also the reason for the higher ΔT_{min} of separability.

5.9.3 Signals with mean 3 hits per event

Reconstructing the standard signal samples which have mean 3 hits per event with the network trained on uniformly distributed hit events, an efficiency of 96% was reached. This is only slightly lower than the global efficiency for the same samples reconstructed with the 5 hit per event model Section 5.8.2 and is in any case higher than the efficiency obtained when reconstructing the samples with the network that was trained on standard events (Section 5.4).

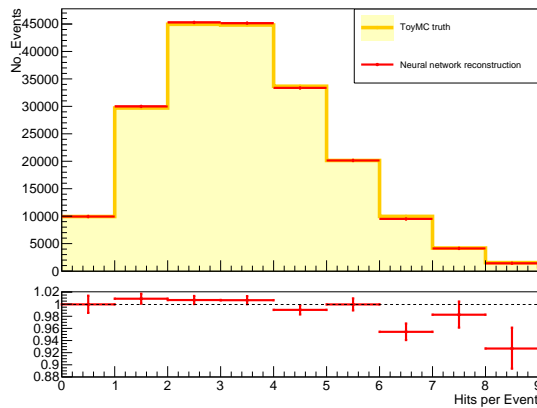


Figure 5.21: Number of hits per event created and reconstructed for events with mean 3 hits per event reconstructed with the uniform distribution neural network.

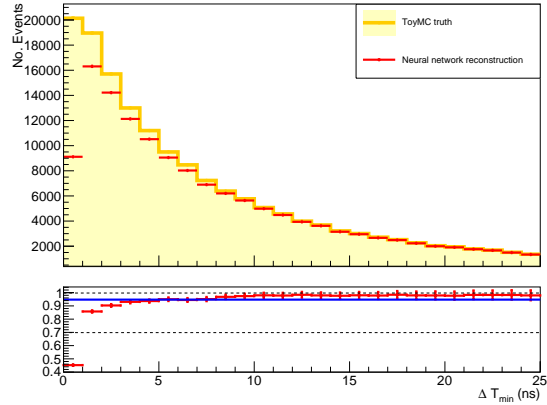


Figure 5.20: Minimum difference in time between hits in the same event for simulated events and events correctly reconstructed, events with mean 5 hits per event reconstructed with the uniform distribution neural network.

Given that events with more hits per event are more likely to have hits arriving closer in time, it is likely that the difficulty in reconstructing events with more hits is also the reason for the higher ΔT_{min} of separability.

5.9.3 Signals with mean 3 hits per event

Reconstructing the standard signal samples which have mean 3 hits per event with the network trained on uniformly distributed hit events, an efficiency of 96% was reached. This is only slightly lower than the global efficiency for the same samples reconstructed with the 5 hit per event model Section 5.8.2 and is in any case higher than the efficiency obtained when reconstructing the samples with the network that was trained on standard events (Section 5.4).

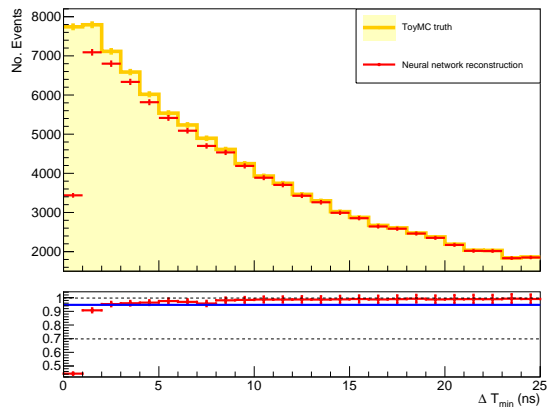


Figure 5.22: Minimum difference in time between hits in the same event for simulated events and events correctly reconstructed, events with mean 3 hits per event reconstructed with the uniform distribution neural network.

From these plots it can be seen that 95% separability is reached at approximately the same ΔT_{min} when the standard samples are reconstructed using the uniformly distributed hit model

as when they're reconstructed with the 5 hit per event model, however for all $\Delta T_{min} < 25$ ns the reconstruction efficiency is lower for the uniform hit model.

This study shows that even if a model trained on uniformly distributed hits has a lower overall efficiency than a model trained on samples with poissonian hits per event, when the model is used to reconstruct the standard samples the parameters of interest (overall efficiency and ΔT_{min} at which hits are separated with 95% efficiency) do not suffer greatly. It seems likely that if it were possible to find a neural network architecture to reconstruct uniformly distributed hits with a higher degree of overall efficiency, it would result in a significant improvement to the reconstruction of the standard samples. As discussed in Section 5.13 however, training a model with other distributions could provide an even better outcome.

5.10 Signals with exponential rise time

The standard samples used in this analysis have a linear 7 ns risetime. It can be seen from Figure 5.2a however, that this is a very idealised idea of the pulse which does not, for example, reproduce the rounded peak that is seen in real data. In order to try to improve the shape, a sample of signals with an exponential rise time was created. The details of the simulations of these signals are explained in Section 5.1. Using 7 convolutional blocks and dropout of 25% the efficiency of reconstruction of these signals was 93%.

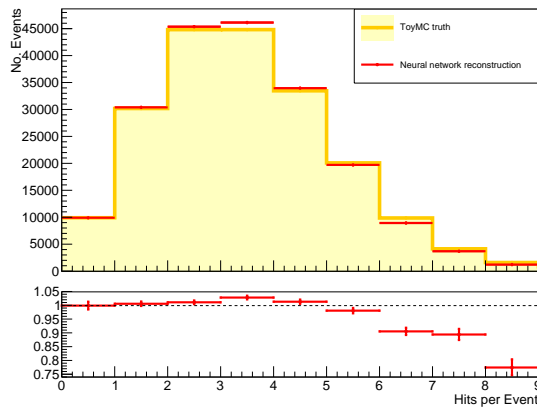


Figure 5.23: Number of hits per event created and reconstructed for events with an exponential rise.

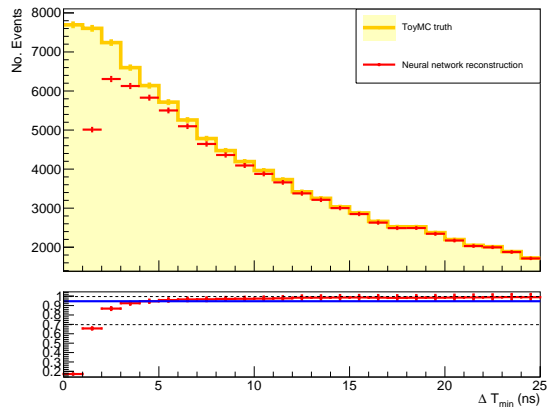


Figure 5.24: Minimum difference in time between hits in the same event for simulated events and events correctly reconstructed, events with an exponential rise.

Here, separability is already reached well before the risetime, at $\Delta T_{min} > 4$ ns. This study shows that it is possible to find a neural network architecture which is able to reconstruct waveforms with exponential rise times with an efficiency at least as good as that of standard signals. This lends support to the idea that it would be possible to find an architecture which is able to reconstruct signals with the true shape of the veto pulses.

5.11 Uncalibrated signal sample

The final study undertaken on signals simulated using the ToyMC investigated the effect of unequalised gain of different veto channels on the possibility of finding a functioning reconstruction. In order to simulate the different gains of each of the 90 Veto channels, an array of 90 randomly generated “calibration constants” were created in the range $U(0.7,1.3)$ and for each event a number was chosen in the range $U[0,90)$ to simulate the veto channel. Once the channel had been simulated, the element of the calibration constant array which corresponded to the simulated channel was used to multiply the simulated amplitude of the hits in the event.

These signals were reconstructed using a neural network with 4 convolutional blocks. Using this model the reconstruction efficiency of these “uncalibrated” signals was 95%.

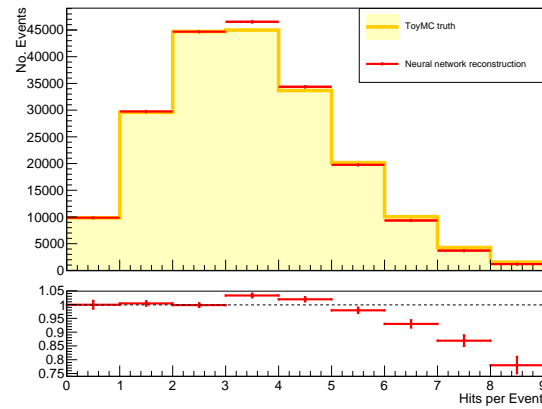


Figure 5.25: Number of hits per event created and reconstructed for events with random “calibration” constant.

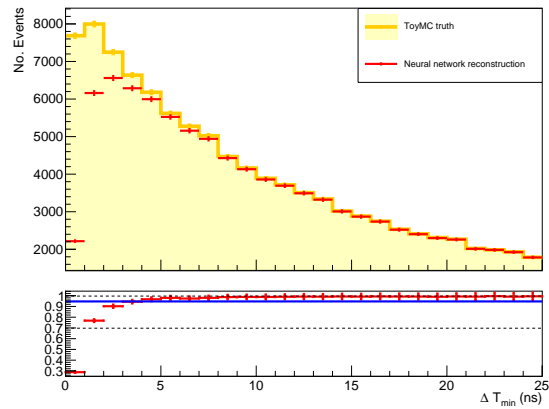


Figure 5.26: Minimum difference in time between hits in the same event for simulated events and events correctly reconstructed, events with random “calibration” constant.

It can be seen from this that it is possible to find a model which reconstructs signals well even if they come from channels of the Veto which do not have perfectly calibrated responses to the energy of incoming particles. This probably means that the network doesn’t rely heavily on the pulse amplitude.

5.12 Model trained on signals from data-averaged signals

A model was trained on a sample of signals created from a mixture of all of the Veto channel templates, as described in Section 5.12. With 8 convolutional blocks, an efficiency of 85% was reached with a sample size of 200,000 training events and 100,000 validation events. After completing the analysis reported below, the network was retrained with 400,000 training and 200,000 validation events but the efficiency only rose to 86%, so the analysis was not repeated.

5.12.1 Signals from mix of templates

Using this network to reconstruct a sample of 400,000 signals created using the same combination of channel templates as was used to train the network, the efficiency reached 86%, and hits were separated at 14 ns. The efficiency of the TSpectrum reconstruction on this sample was 64% and hits were separated at $\Delta T_{min} > 25$ ns.

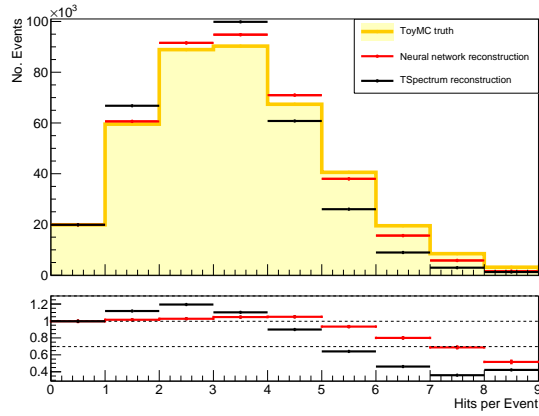


Figure 5.27: Number of hits per event created and reconstructed for events from the Channel 2 template, analysed with the model trained on the mixed channel template.

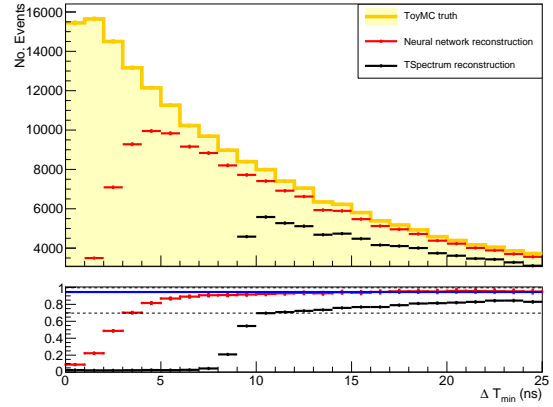


Figure 5.28: Minimum difference in time between hits in the same event for simulated events and events correctly reconstructed, events from the Channel 2 template, analysed with the model trained on the mixed channel template.

5.12.2 Signals from Channel 0 Template

Reconstructing 400,000 signals made from the template of pulses from PVeto Channel 0, using the model trained on all of the Veto channels, an efficiency of 86% was reached. This is comparable to the validation efficiency of the trained network.

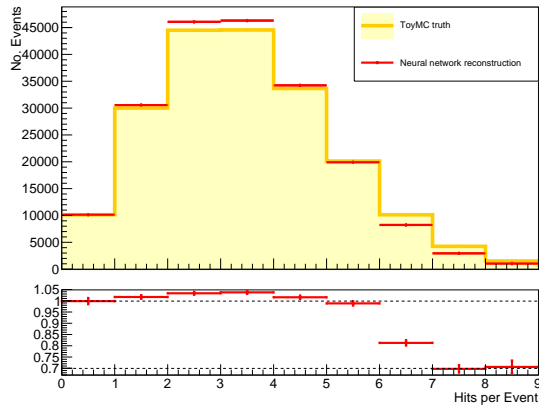


Figure 5.29: Number of hits per event created and reconstructed for events from the Channel 0 template, analysed with the model trained on the mixed channel template.

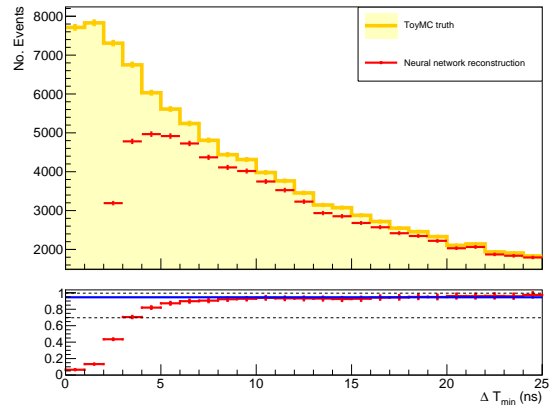


Figure 5.30: Minimum difference in time between hits in the same event for simulated events and events correctly reconstructed, events from the Channel 0 template, analysed with the model trained on the mixed channel template.

From Figure 5.29 it can be seen that on average the network underestimates the number of hits per event and Figure 5.30 shows that there appears to be an oscillation effect with the reconstructed efficiency dipping and rising again approximately with every 10 ns added to ΔT_{min} . Since 10 ns is approximately the rise time of the pulse (see Figure 5.3), it is possible that the dip is related to this fact, however why this would cause the effect to repeat is not yet understood.

The large errors in Figure 5.30 mean that it is impossible to say with certainty at exactly which value of ΔT_{min} the separability threshold is reached.

5.12.3 Signals from Channel 1 Template

Signals simulated with the template from Channel 1 events were reconstructed using the model trained on signals from all the Veto channels, and an efficiency of 84% was obtained.

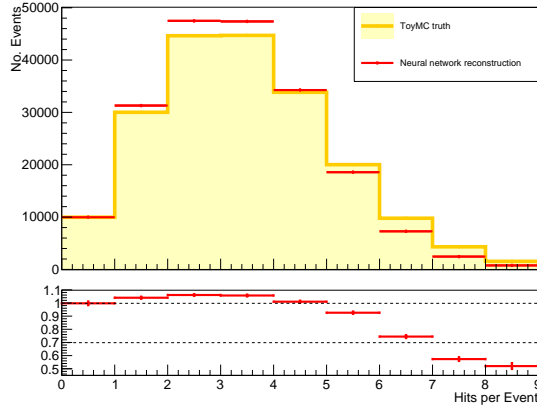


Figure 5.31: Number of hits per event created and reconstructed for events from the Channel 1 template, analysed with the model trained on the mixed channel template.

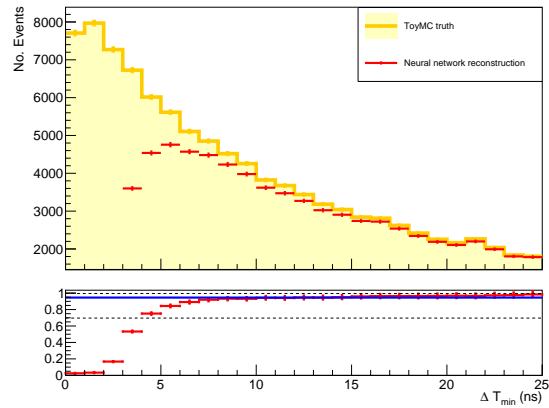


Figure 5.32: Minimum difference in time between hits in the same event for simulated events from the Channel 1 template, analysed with the model trained on the mixed channel template.

The underestimation of the number of hits per event can be seen again in Figure 5.31, however Figure 5.32 does not seem to show the characteristic dip in efficiency, and the oscillation effect is reduced compared to the reconstruction of Channel 0 with the mixed model (Figure 5.30). Since the overall efficiency of this reconstruction is slightly lower (84% as opposed to 85%), this shows that the oscillation is not more evident in lower efficiency studies.

5.12.4 Signals from Channel 2 Template

The reconstruction of signals from the Channel 2 template using the mixed template model gave an efficiency of 86%.

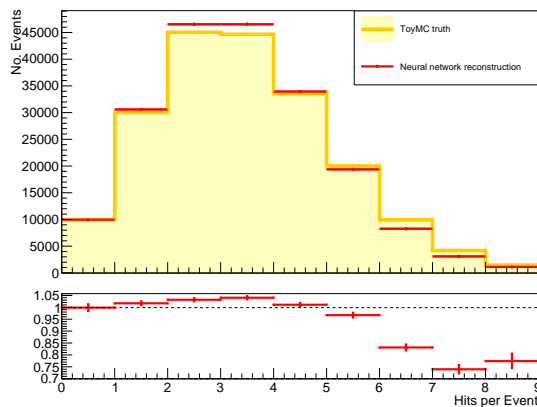


Figure 5.33: Number of hits per event created and reconstructed for events from the Channel 2 template, analysed with the model trained on the mixed channel template.

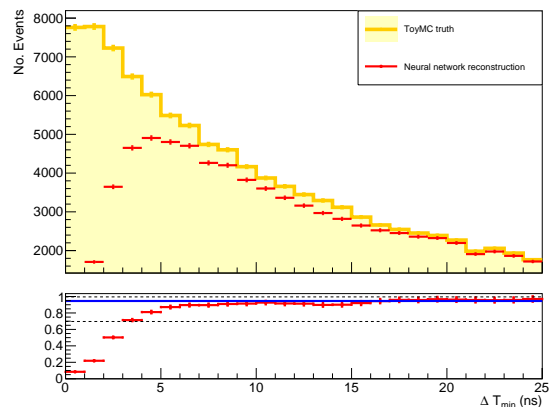


Figure 5.34: Minimum difference in time between hits in the same event for simulated events from the Channel 2 template, analysed with the model trained on the mixed channel template.

The underestimation of the number of hits per event can be seen again in Figure 5.33, and again we see that despite this data sample having the highest reconstruction efficiency of the three samples reconstructed with the mixed channel model, the oscillation effect is the most visible in this study (Figure 5.34).

5.13 Conclusion

The work in this chapter demonstrates that it is possible to create a convolutional neural network to reconstruct simulated signals from the PVeto at PADME. It has been shown that the architecture required for the network depends on the particular characteristics of the signal samples used, but in all cases an acceptable level of efficiency was achieved and 95% separability was reached at a relatively low ΔT_{min} .

It is likely that if a network were trained on samples of events which had more events with high numbers of hits per event than events with low numbers of hits per event, the performance of the network on the standard samples would be improved. This is because events with more hits are more complex and have hits closer together in time on average, meaning that higher numbers of examples of these events are needed to train the network to recognise their shape.

This study supports the hypothesis that a convolutional neural network could be found to reconstruct all channels of the Veto with roughly equal efficiency, however the network trained on templates from data from all of the veto channels was not as efficient as most of the networks trained on toy Monte Carlo signals. It is possible that increasing the size of the training and validation samples could improve this situation, however the increase would have to be very large, as doubling from 200,000 to 400,000 training samples did not produce significant effects. It is also possible that changing the distribution of hits per event as mentioned above could have a bigger impact, however this was not tested in this work.

The data tests also show an unusual oscillation effect in the reconstruction efficiency as a function of the minimum difference in time between two hits in an event. This study did not investigate the reasons for this effect, however it is not clear that an overall increase in reconstruction efficiency would prevent this from happening.

The neural networks created in this study did not reconstruct hit position or amplitude, both fundamental characteristics both for correct vetoing of Bremsstrahlung radiation and for searches for multi-lepton final states. If machine learning tools are implemented in the PADME reconstruction, a method will have to be developed to find the peaks and not only count them. The output from the neural network could be used, for example, as an input parameter for TSpectrum to force the method to search for the number of peaks determined by the neural network.

Since this study was finished, the PADME group at Sofia University has successfully merged neural networks with the standard PADME software and are studying the use of these tools in the analysis of Run 3 data. At the time of writing, however, these tools have not been fully integrated and tested with the full software framework. For this reason, the reconstruction used for the analysis described in Chapter 6 used the analytical tools discussed in Chapter 4. Nevertheless, the success of these techniques is enough to provide an encouraging starting point for further studies into their use for the reconstruction of real data at the PADME experiment.

Chapter 6

Bhabha scattering in PADME Run 2

This thesis presents a measurement of the Bhabha scattering cross-section in the Run 2 data at PADME. The first step in the analysis was to study the geometrical acceptance and the topology of Bhabha scattering events in the PADME detector, outlined in Section 6.1. Section 6.2 sets out the data conditions of the sample used in the analysis presented here. This is followed by a discussion of the timing measurement for particles presumed to come from Bhabha scattering final states (Section 6.3).

Since a measurement of the cross-section of Bhabha scattering relies on a measurement of the number of positrons incident on the Target (NPoT), this information is presented in Section 6.4, after which the sources of background to the Bhabha scattering measurement are presented in Section 6.5, and the process by which they are subtracted is explained in Section 6.6. The number of signals observed is then presented in Section 6.7, and the conversion to cross section is discussed in Section 6.8 before the chapter ends with a discussion of the systematic errors in Section 6.9.

6.1 Topology of Bhabha scattering at PADME

The Veto detectors were originally designed to study Bremsstrahlung. Bremsstrahlung has a very different kinematic profile from Bhabha scattering, and therefore a different angular spectrum, particularly compared to S-Channel Bhabha scattering processes. Since positrons which undergo Bremsstrahlung in the Target typically lose relatively little energy, when leaving the Target the particles are still highly boosted forward and therefore the angular distribution of these particles peaks sharply at low angles to the beam. This means that it can be assumed that any deviation from the z-axis is due only to the effect of the dipole magnet. This in turn means that the z-coordinate of the final point of impact of the particle in the Veto, given by the channel number, can be used to reconstruct the momentum of the particle as discussed in Section 4.4.

The kinematic difference between Bremsstrahlung and Bhabha scattering, particularly S-channel, gives rise to very different angular spectra for the final state particles, as seen in Figure 6.1. This difference in angular distribution causes a completely different correlation between the energy of final state particles and their channel of arrival. The kinematic distributions of S-Channel and T-Channel Bhabha scattering are treated in more detail in Sections 6.1.1 and 6.1.2 respectively. From the analysis presented in these sections, it is clear that it isn't possible to find an analytical formula to infer particle energy from point of impact for final state particles coming from Bhabha scattering. Therefore, the analysis strategy can't be based on finding pairs of particles with energies that sum to the beam energy. With reference to Figure 6.1, it should be noted that the two Bhabha channels were studied independently using samples generated from CalcHEP, whereas Bremsstrahlung and the combination of all Bhabha scattering processes were studied using the physics generator "G4MollerBhabhaModel" from Geant4 [100]. The T-Channel process produced by CalcHEP included a cut on the energy of the outgoing electron at 1 MeV,

to avoid infrared divergence.

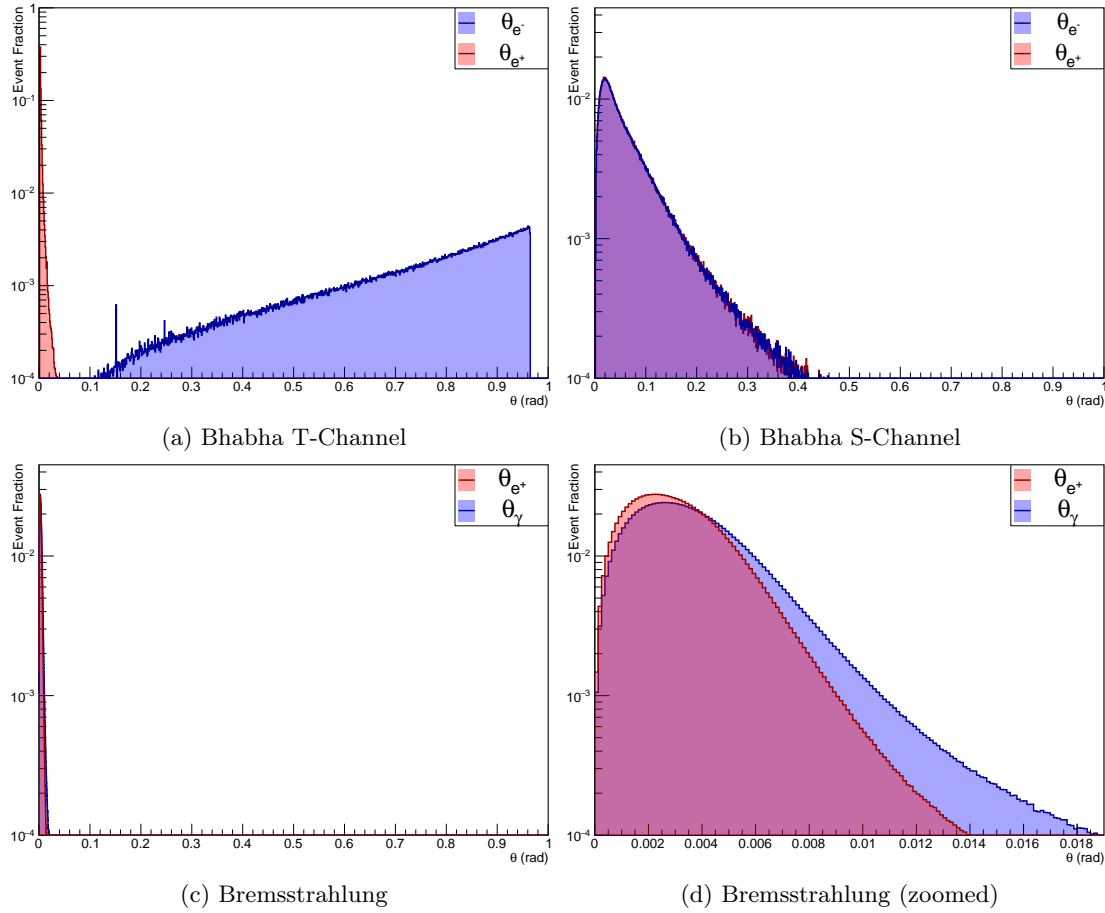


Figure 6.1: Theta: angle to beamline of final state particles in lab frame for Bremsstrahlung and T-Channel and S-channel Bhabha scattering. The positron is represented in red in each case, while in Bhabha scattering blue represents the electron and in Bremsstrahlung blue represents the photon. Plots have been normalised to the total number of events simulated. The bottom right subfigure is a zoom of the bottom left.

While this thesis provides a measurement of the inclusive Bhabha scattering cross section, it is worth noting that, as discussed in Chapter 2, for Dark Sector studies, the kinematic distribution of the S-Channel will be identical to the distribution of final state particles resulting from the decay of, for example, a dark photon (A') with mass $m_{A'} = \sqrt{s}$. In this context, therefore, it is particularly important to study the kinematic and geometrical characteristics of the S-Channel process. As is demonstrated in the following subsections, the S-Channel acceptance in PADME Run 2 was around 15%, while the T-Channel acceptance is $\sim 0.07\%$, meaning that visible decay searches for dark photons would not be overwhelmed by background coming from T-Channel Bhabha scattering. This is a unique opportunity at fixed-target experiments, since in experiments with colliding beams of equal energy the conservation of momentum means that there would be no preferred direction for final state particles in either channel.

The geometrical acceptance was studied using an algorithm known as the “swimmer” which took charged particles produced at the Target in the Monte Carlo and, based on their kinematic properties, the geometry of the detector and the map of the magnetic field, calculated their trajectory point-by-point in steps of 0.2 mm, providing the predicted impact point in the veto system.

6.1.1 S-Channel Bhabha Scattering

Since in S-Channel scattering, the off-shell photon produced in e^+e^- annihilation converts into an e^+e^- pair, the final state particles are emitted symmetrically with respect to the beamline. Combined with the symmetry of the experimental setup, this kinematic symmetry leads to an expected symmetry in the final geometrical distribution of the detected particles as well.

As is discussed in Chapter 4 and treated in more detail in Section 6.2, above Channel 70, the beam halo causes pileup to increase, leading to increased difficulty of reconstruction in this region. Particles which arrived in channels downstream of Channel 70 were therefore omitted from this analysis. As can be seen in Figure 6.2, when final-state particles from Bhabha scattering enter either Veto in channel ≤ 70 , the other final-state particle enters the opposite Veto in channel ≥ 30 . Therefore the signal region for this analysis was defined as:

$$PVetoChID, EVetoChID \in [30, 70]$$

Considering the 4 broken EVeto channels, out of 100,000 tree-level S-Channel events simulated in CalcHEP, approximately 45,000 entered the PADME vetoes, of which approximately 15,000 are contained in the accepted region. This gives a geometrical acceptance of $\sim 15\%$ for the S-channel process.

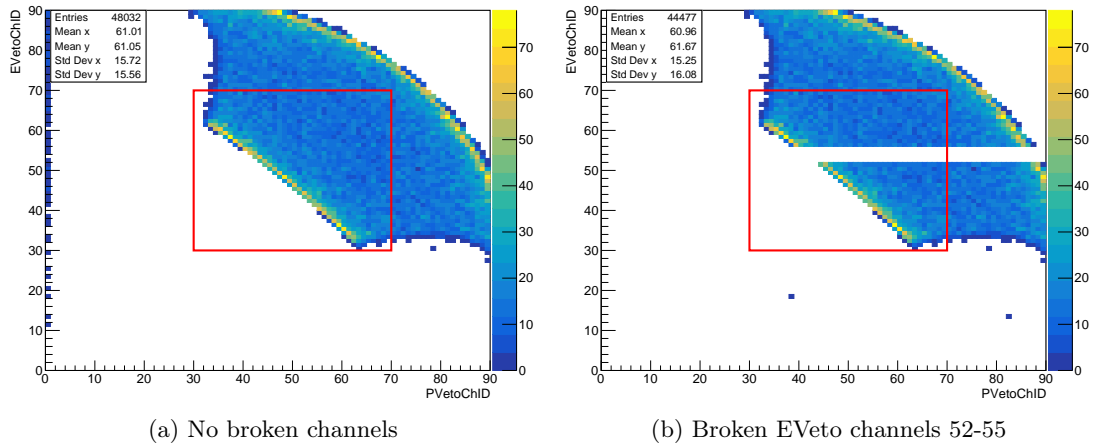


Figure 6.2: Geometrical occupancy of Bhabha S-Channel processes; PVeto channel on x-axis, EVeto channel on y-axis. The red box represents the range between channels [30,70] in both vetoes, the geometrical region considered for this analysis. The left plot shows the distribution as it would be without the four broken EVeto channels while the right plot shows the effect of these broken channels.

The bimodal distributions shown in Figure 6.2 can be seen again in Figure 6.3, which shows the energy in the lab frame of final state particles from S-Channel events as a function of the Veto channel number in which they arrive. This can be contrasted with the monomodal distribution found in Bremsstrahlung events, shown in Figure 4.26.

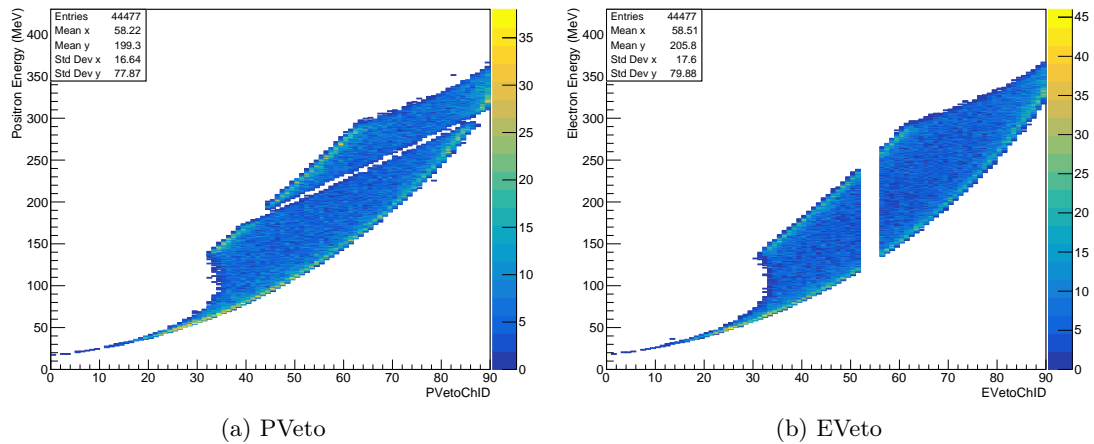


Figure 6.3: Energy of positrons (electrons) vs PVeto (EVeto) channel in which particles arrive, for final-state particles from S-Channel Bhabha scattering.

It can be seen therefore, that for the same channel of impact in the Veto, there is a wide range of energies available to the final-state particles, with two equally probable values on each side of the spectrum. This means that, unlike the Bremsstrahlung case, it is impossible to find a function that transforms Veto channel into particle energy.

Studying the geometrical distribution of e^+e^- pairs coming from S-Channel Bhabha scattering accepted in the PADME Vetoes, shown in Figure 6.2, it can be seen that the signal has a distribution of channel sum greater than a constant:

$$PVetoChID + EVetoChID > const.$$

This is shown clearly in Figure 6.4, where it can be seen that all of the signal lies in the range $PVetoChID + EVetoChID \geq 90$.

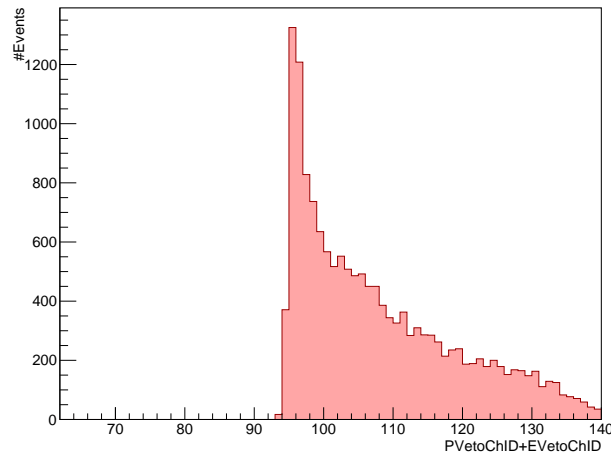


Figure 6.4: Channel sum $PVetoChID + EVetoChID$ for S-Channel Bhabha events with $PVetoChID, EVetoChID \in [30, 70]$.

Selecting events which end up in the region $PVetoChID + EVetoChID \geq 90$ shows that even in the selected events it is still impossible to find a relation that gives the energy of a particle entering the Veto as a function of the channel where it enters. This can be seen in Figure 6.5

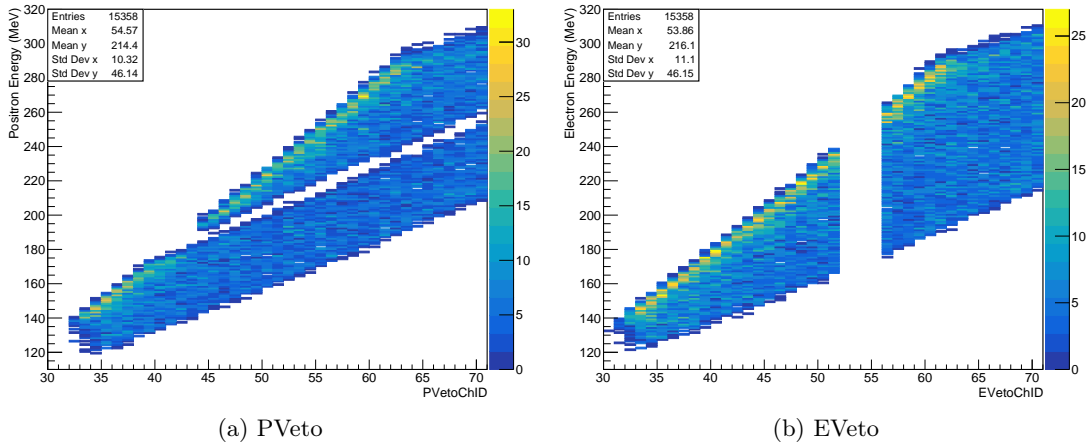


Figure 6.5: Energy of positrons (electrons) vs PVeto (EVeto) channel in which particles arrive, for S-Channel final-state particles where $PVetoChID + EVetoChID \geq 90$.

The angular spectrum of accepted S-Channel particles is shown in Figure 6.6. Here it can be seen that the accepted range of angles is very wide, giving rise to the wide energy spectrum for each channel of impact in the Veto.

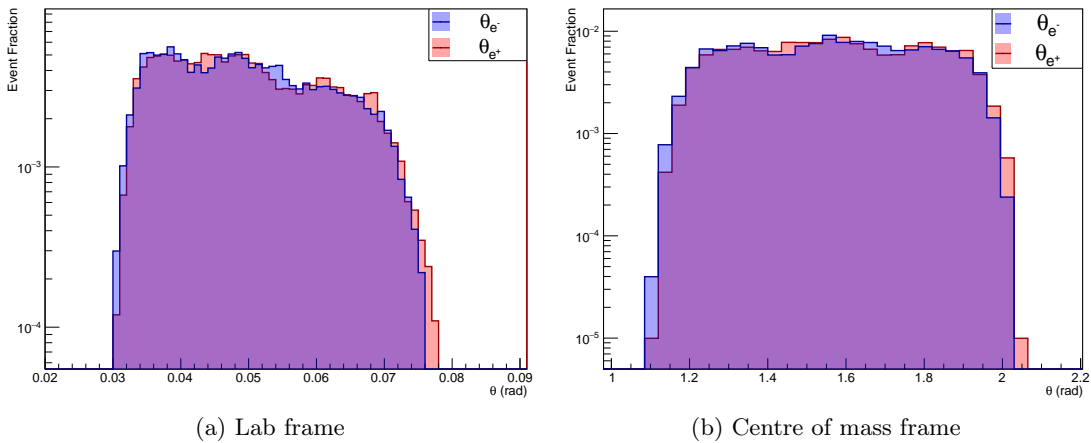


Figure 6.6: Theta: angle to beamline of final state particles from S-Channel Bhabha scattering for events where both particles end up in selected signal region, in lab frame and in centre of mass frame. Plots have been normalised to the total number of events simulated.

6.1.2 T-Channel Bhabha Scattering

Figure 6.1a shows the kinematic distributions of tree-level T-Channel final-states, generated in CalcHEP. As can be seen there, the angular distribution of final state particles coming from T-Channel processes is strongly asymmetric, with the positron mostly very forward. This means that the acceptance of final state particles coming from T-Channel events is much smaller than for those coming from the S-Channel process: of 2×10^7 T-channel events, only 13,000 end up in the selection $PVetoChID, EVetoChID \in [30, 70]$. This gives an acceptance of 0.065%.

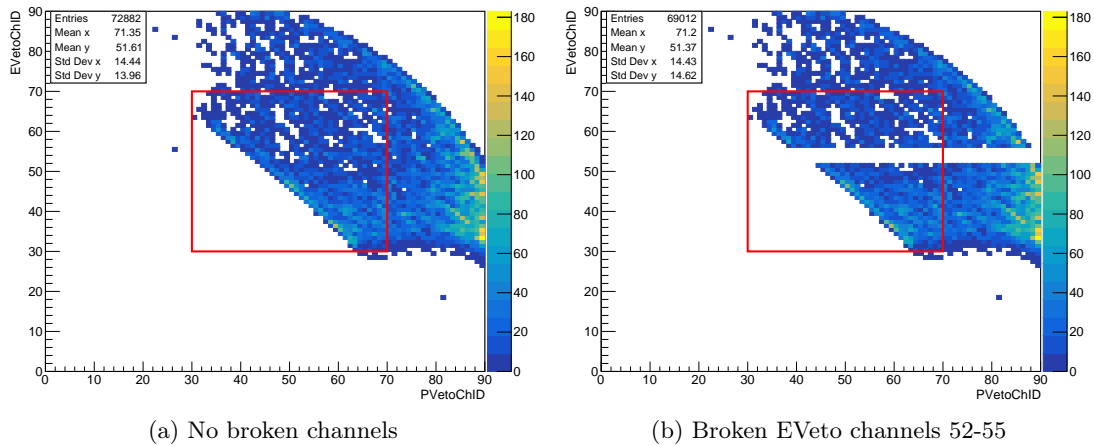


Figure 6.7: Geometrical occupancy of Bhabha T-Channel processes, with and without the effect of the 4 broken EVeto channels. The red box represents the range between channels [30,70] in both vetoes, the geometrical region considered for this analysis.

Figure 6.7 also shows, however, that the populated areas of the vetoes end up being the same, even if the distribution of events within these areas is different: T-Channel events dominantly populate the region of the PVeto closest to the ECal while S-Channel events are more evenly distributed over all of the channels. This shows that the two channels cannot be separated and measurements of the cross section for each channel independently cannot be performed.

The hotspot at high PVeto channels can be seen again in Figure 6.8 which shows the relation between energy and final channel in the Vetoes for T-Channel final state particles. Here again, it is clear to see that there isn't one specific value of particle energy for each Veto channel.

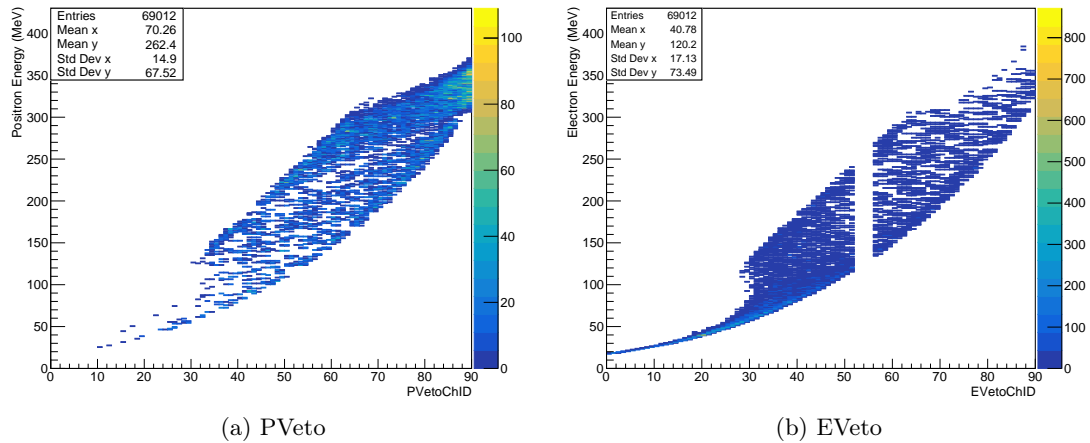


Figure 6.8: Energy of positrons (electrons) vs PVeto (EVeto) channel in which particles arrive, for T-Channel particles.

The similarity in topology of the S-Channel and the T-Channel processes leads to the distribution of $PVetoChID + EVetoChID$ lying in the same region for both S-Channel and T-Channel processes, as shown in Figure 6.9.

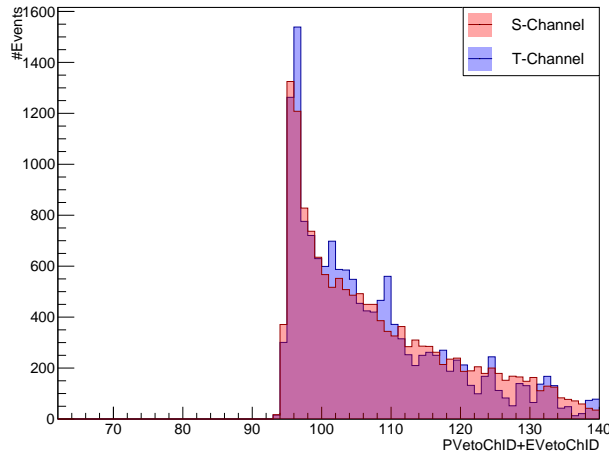


Figure 6.9: Channel sum $PVetoChID + EVetoChID$ for S-Channel and T-Channel Bhabha events with $PVetoChID, EVetoChID \in [30, 70]$. The T-Channel distribution has been scaled to the number of accepted S-Channel events, a factor of 1.2 times.

Performing the selection of the region $PVetoChID + EVetoChID \geq 90$ in T-Channel processes shows that the T-Channel process suffers from the same problem with regards to reconstructing particle energy given channel number as the S-Channel, as seen in Figure 6.10

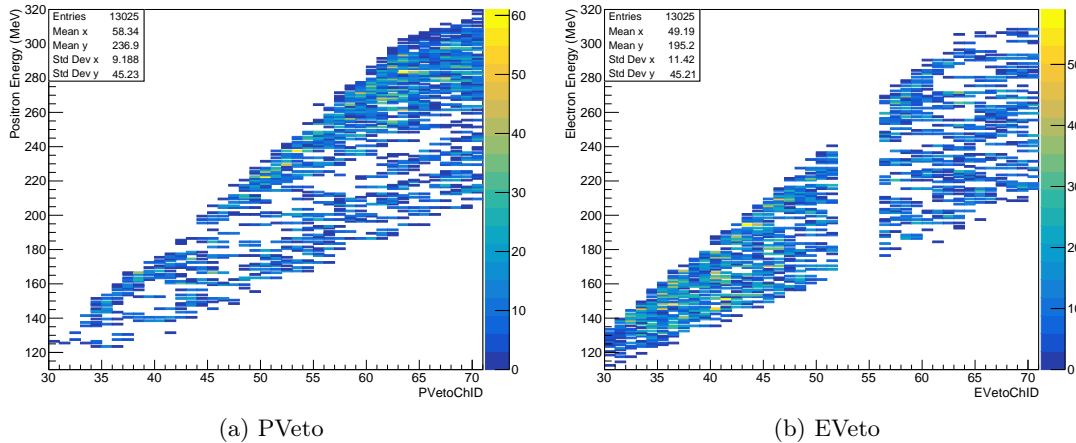


Figure 6.10: Energy of positrons (electrons) vs PVeto (EVeto) channel in which particles arrive, for T-Channel particles where $PVetoChID + EVetoChID \geq 90$.

Given the similarities in the geometrical distributions of S- and T-Channel final states, it is no surprise that the angular range covered by the T-Channel process, shown in Figure 6.11, lies in almost the same region as the S-Channel (cf. Figure 6.6).

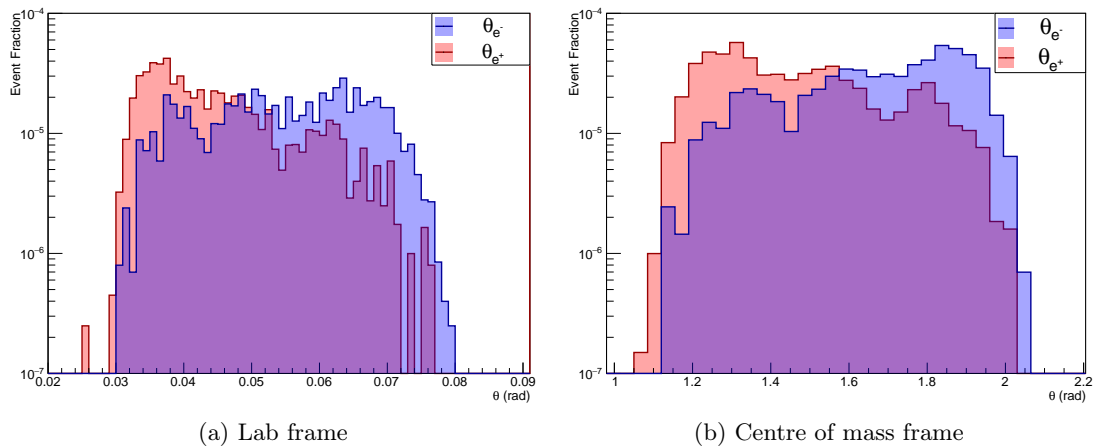


Figure 6.11: Theta: angle to beamline of final state particles from T-Channel Bhabha scattering for events where both particles end up in selected signal region, in lab frame and in centre of mass frame. Plots have been normalised to the total number of events simulated.

6.1.3 Combined S- and T-Channel

In order to study the combined effect of both channels and the interference between them, the Geant4 physics generator “G4MollerBhabhaModel” was used to create the Bhabha scattering events for the full Monte Carlo sample [100]. This was the same sample used in the cross section analysis. It should be stressed again here that Geant4 only contains tree-level calculations for the Bhabha cross-section.

The full Monte Carlo sample included the full simulation of the beamline, meaning that some of the particles which arrived at the target had already lost energy, for example in interactions in the Mylar window, or were slightly out of the nominal trajectory. This leads to a small number of Bhabha events producing particles which arrive outside of the acceptance seen in Sections 6.1.1 and 6.1.2.

The sample contained 2×10^6 bunches, each containing an average of 5.2×10^3 positrons on Target (PoT) per bunch and a total of 4.49×10^7 Bhabha events, and gave the geometrical occupancy shown in Figure 6.12. From this sample, approximately 37,000 Bhabha events entered the selection, giving an acceptance of 0.082%.

The distributions of particle energies vs channel of impact are shown in Figure 6.13. The hotspot at high PVetoChID shown in Figures 6.12 and 6.13a, together with the region of (PVetoChID, EVetoChID) between (30,60) and (60,30) in Figure 6.12 show that despite the low acceptance of T-Channel events, the higher cross section of this process compared to the S-Channel means that a significant number of these events are still detectable by the experiment.

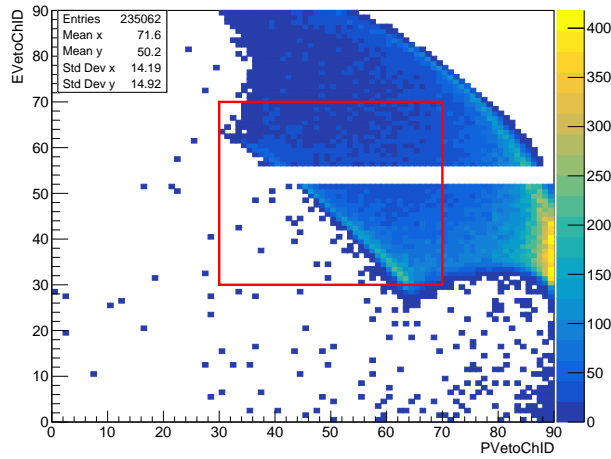


Figure 6.12: Geometrical acceptance of Bhabha events from Geant4 generator. The red box represents the range between channels [30,70] in both vetoes, the geometrical region considered for this analysis.

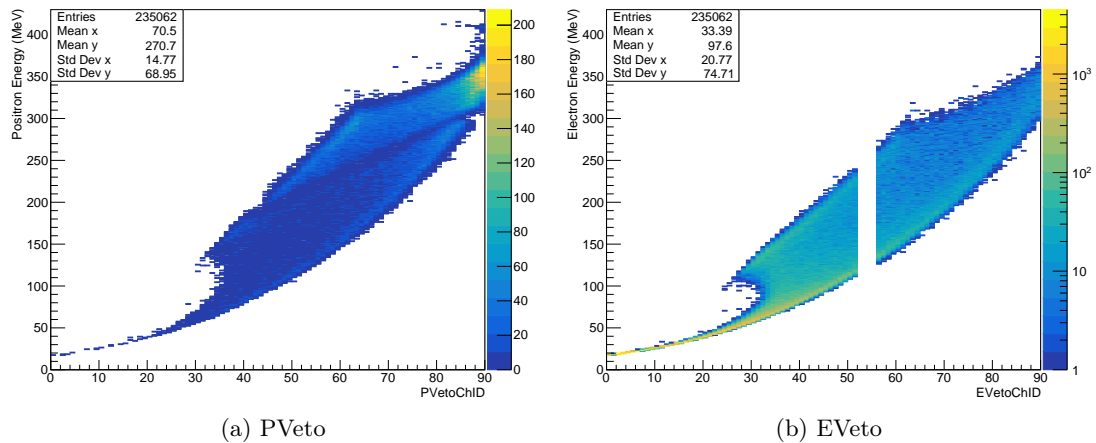


Figure 6.13: Energy of positrons (electrons) vs PVeto (EVeto) channel in which particles arrive, for Bhabha events from Geant4 generator.

The kinematic constraints mean that the distribution of the sum of the channels remains consistent with the distributions from the two Bhabha channels individually, as seen in Figure 6.14.

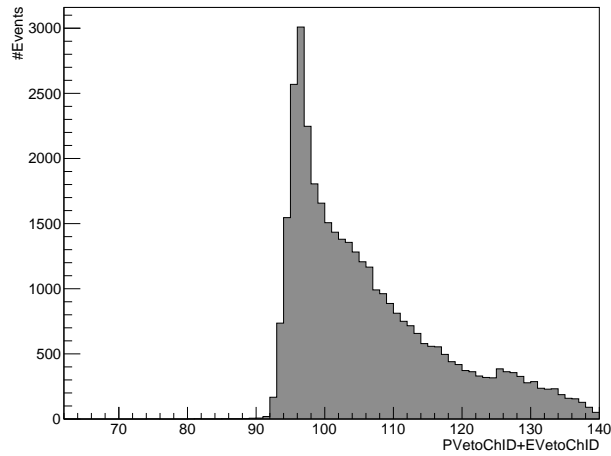


Figure 6.14: Channel sum $PVetoChID + EVetoChID$ for Bhabha events from Geant4 generator which have $PVetoChID, EVetoChID \in [30, 70]$.

Applying the selection that both particles must arrive in the accepted region and satisfy $PVetoChID + EVetoChID \geq 90$, it can be seen that of the $\sim 10.4 \times 10^6$ PoT, approximately 3,700 Bhabha events were produced that were accepted into the geometrical selection. The final angular range accepted from all Bhabha events is seen in Figure 6.16

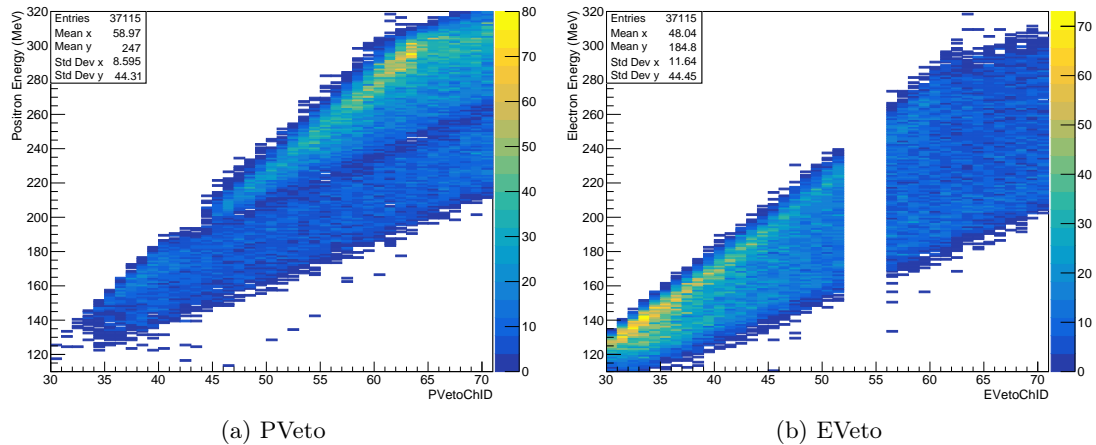


Figure 6.15: Energy of positrons (electrons) vs PVeto (EVeto) channel in which particles arrive, for Bhabha events from Geant4 generator which satisfy $PVetoChID + EVetoChID \geq 90$.

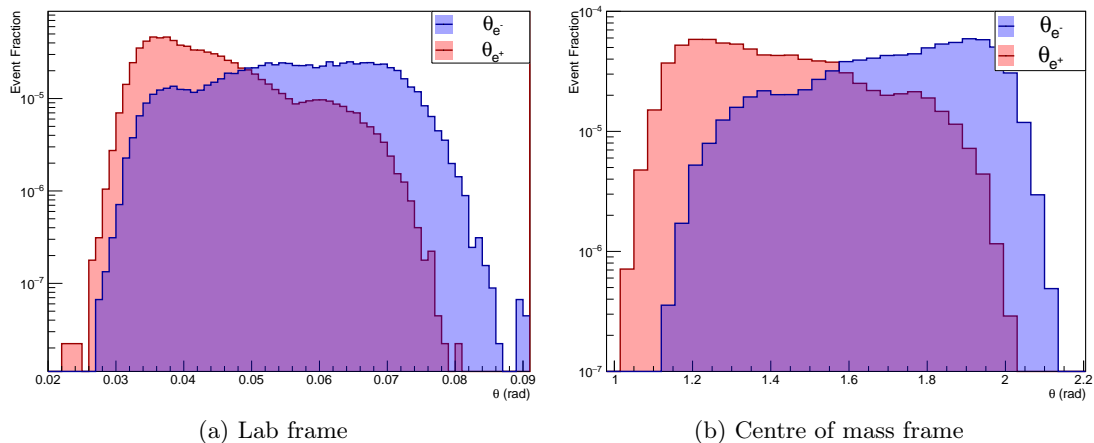


Figure 6.16: Theta: angle to beamline of final state particles for Bhabha scattering from Geant4 generator for events where both particles end up in selected signal region, in lab frame and in centre of mass frame. Plots have been normalised to the total number of events simulated.

As motivated in the preceding sections, the geometrical selection for Bhabha events was based on the following two criteria:

- $PVetoChID, EVetoChID \in [30, 70]$
- $PVetoChID + EVetoChID \geq 90$

6.2 Pile-up and Veto occupancy rates

All types of background become more probable with more particles close in time between the Vetoes, a phenomenon known as pile-up. Clearly, therefore, the higher the intensity of the beam the greater the problem posed by background. However, the high cross-section and acceptance of the Bhabha processes presented in Section 6.1.3 mean that the analysis does not require very large numbers of PoT to achieve a precise measurement. Therefore, in order to reduce pile-up, this analysis used Run 30660 which had a flux, known at PADME as “multiplicity”, of approximately 4.6×10^3 positrons on target (PoT) per bunch. This is almost 6 times lower than the nominal multiplicity of $27\text{--}28 \times 10^3$ PoT/bunch used in dark photon searches at PADME. However with more than 2.5×10^6 bunches in the run, the total luminosity collected is equivalent to approximately 1×10^{10} PoT and the number of accepted Bhabha scattering events is expected to be of order 10^4 .

As previously discussed, in addition to choosing a low-multiplicity run, the pile-up was further reduced by restricting the analysis to the region of the Vetoes which receives a lower flux of particles. Figures 6.17 and 6.18 show the occupancy in Run 30660.

Since the analysis strategy relies on the Monte Carlo (MC) to calculate the acceptance, it is very important that any cuts applied to the data are well reproduced in the MC. It can be seen in Figures 6.17 and 6.18 that the ratio between the occupancy found in data and MC is very stable, particularly in $PVetoChID, EVetoChID \in [30, 70]$.

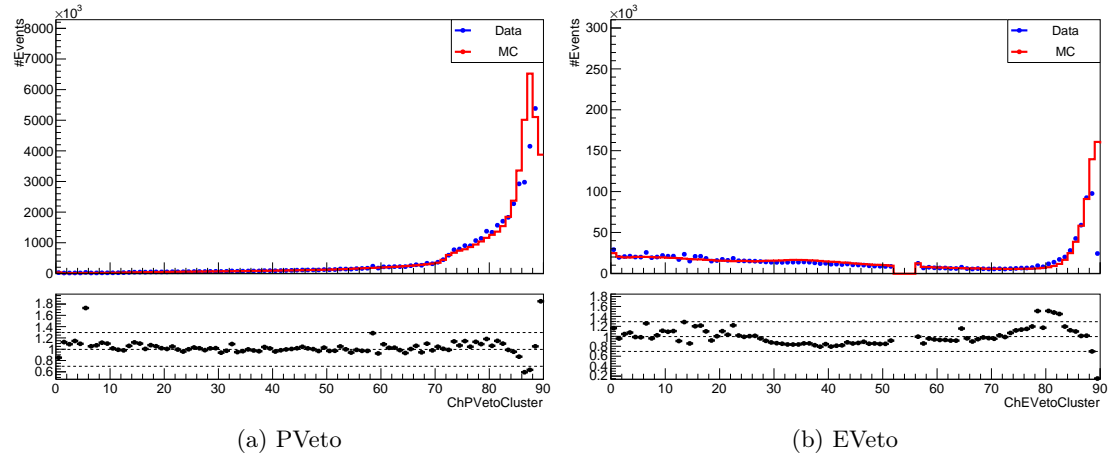


Figure 6.17: Veto occupancy in data compared to MC. Histograms are normalised to the luminosity collected in Run 30660.

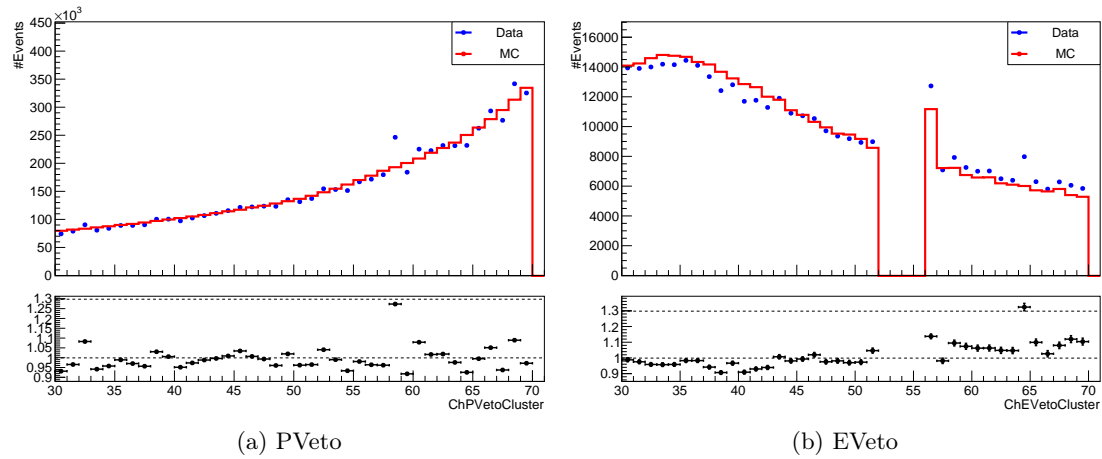


Figure 6.18: Veto occupancy in data compared to MC, zoomed to channels 30-70. Monte Carlo histograms are normalised to the integral of the data.

The figure of merit here is the ratio of the number clusters which fall inside the selection $PVetoChID, EVetoChID \in [30, 70]$ to the number of clusters outside of the selection. This ratio is given in Table 6.1. The ratio was calculated with respect to all clusters in the range $PVetoChID, EVetoChID \in [0, 90]$, ignoring the last 6 channels of the EVeto for two reasons: first, because these channels are particularly sensitive to the beam halo which may not be very well simulated in the MC, and second, because they had not been studied in order to equalise the channel gains and cable lengths of these channels. It can be seen here that this ratio is very well controlled between data and MC for both detectors.

Table 6.1: Fraction of all clusters which arrive inside channels [30-70] for each Veto in data (blue) and MC (red). Errors are statistical.

Distribution considered	Ratio (clusters with $\text{ChID} \in [30,70]$)/all clusters
PVeto Data	0.1413 ± 0.00041
PVeto MC	0.1395 ± 0.00036
EVeto Data	0.2604 ± 0.0018
EVeto MC	0.2660 ± 0.0020

6.3 Bhabha time of flight correction

In the reconstruction of the Vetoes, the time of arrival of a particle in one of the channels is corrected for contributions coming from the electronics and the cables, as described in Section 4.2.5. At the reconstruction level, however, it is not possible to correct for the time of flight of particles, as this depends on their trajectory which depends in turn on the kinematics of the physical process that produced them. Since this information can only be inferred by combining information from different subdetectors, time of flight corrections can only be performed at analysis level. The kinematic distributions discussed previously lead to final state positrons and electrons travelling along dissimilar trajectories. This means that the time at which they arrive in the respective Vetoes will be different, and therefore the simple subtraction of these times will not be enough to determine whether the particles were emitted at the same time from the target.

However, as shown in Figure 6.19, the difference in time of arrival in the Vetoes is a function of the difference in channel ID of the particles ($\Delta\text{Ch} = \text{PVetoChID} - \text{EVetoChID}$) – used as a proxy for the difference in length of trajectory. The function to go from ΔCh to $\Delta T(\text{PVeto} - \text{EVeto})$ was found by fitting a third order polynomial to the Geant4 Monte Carlo sample. As can be seen comparing Figure 6.19a to Figure 6.19b, selecting Bhabha events from the swimming algorithm which arrive in the final selection $\text{PVetoChID}, \text{EVetoChID} \in [30, 70]$ and $\text{PVetoChID} + \text{EVetoChID} \geq 90$, the reduced angular acceptance means that coefficients of the polynomial vary compared to selecting all Bhabha events entering the Vetoes. Since in the final analysis the only events used came from the selection in Figure 6.19b, the polynomial fitted to this selection was used to reconstruct the difference in time between two clusters in the Vetoes.

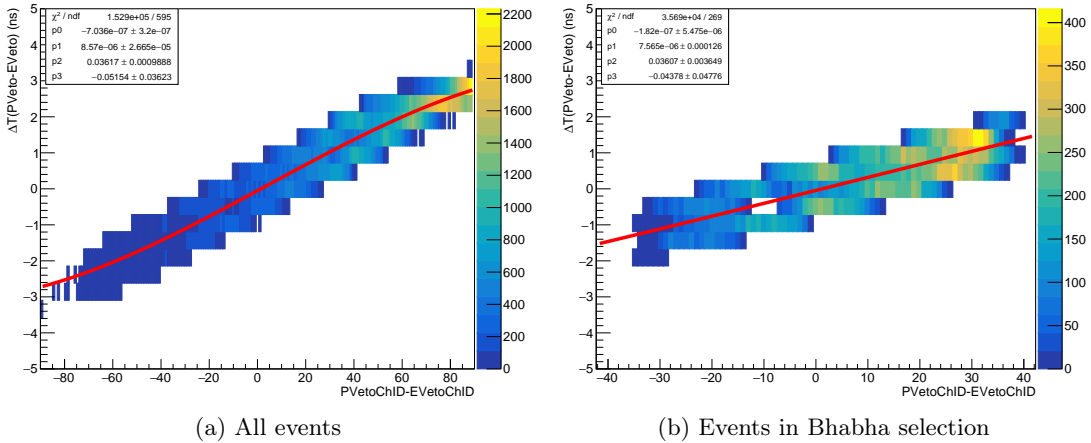


Figure 6.19: Difference in time of arrival from swimming algorithm of Bhabha final state particles in Vetoes as a function of difference in channel number.

Two clusters in the vetoes were therefore considered to be in time if they satisfied

$$|\Delta T(\text{PVeto} - \text{EVeto}) - \Delta T_{\text{traj}}| \leq 5 \text{ ns} \quad (6.1)$$

where ΔT_{traj} is the time correction due to the trajectory, given in ns by

$$\Delta T_{traj} = -1.82 \times 10^{-7}(\Delta Ch)^3 + 7.57 \times 10^{-6}(\Delta Ch)^2 + 0.036\Delta Ch - 0.044 \quad (6.2)$$

with

$$\Delta Ch = PVetoChID - EVetoChID \quad (6.3)$$

The choice of 5 ns as a cut is motivated at the end of this section, after Figure 6.25.

Figure 6.20 shows the effect of applying the relation found from the swimming algorithm to reconstructed clusters from the full Monte Carlo simulation which end up in the selection. It can be seen that the time resolution between the two Veto detectors improves very significantly.

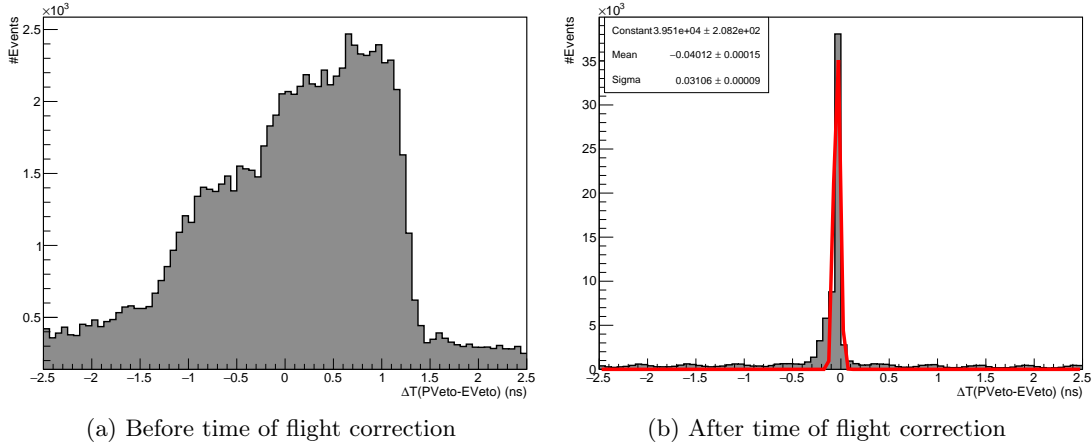


Figure 6.20: Difference in time of arrival of clusters in Veto detectors in full Geant4 Monte Carlo sample before and after applying the time of flight correction, as calculated in Equations (6.2) to (6.3), for clusters in geometrical selection.

Figure 6.21 shows the effect of applying this correction to the data. Here it can be seen that, although the distribution is better centred on zero and the peak is thinner after the correction is applied, the improvement is much more modest in the data than in the Monte Carlo of Figure 6.20.

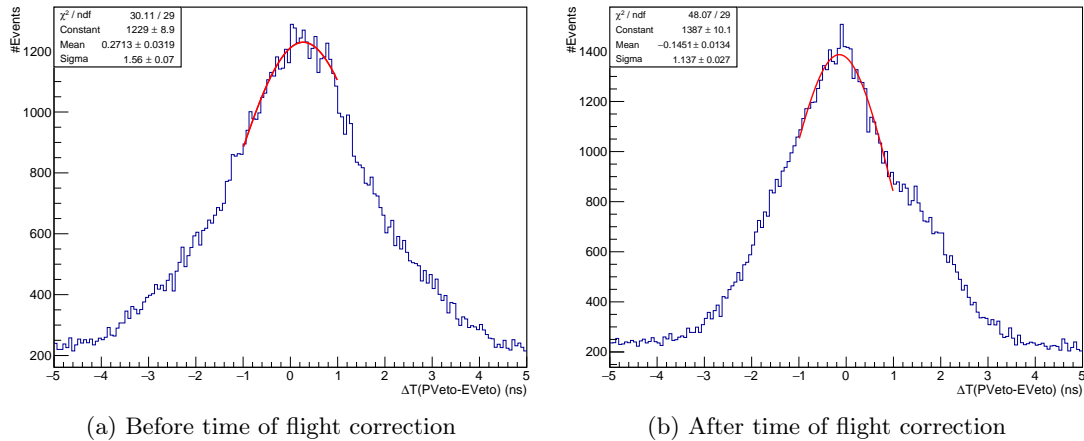


Figure 6.21: Difference in time of arrival of clusters in Veto detectors in Run 30660 before and after applying the time of flight correction, as calculated in Equations (6.2) to (6.3).

The difference here between data and Monte Carlo comes from the following three effects which exist in the data but are not modelled in the Monte Carlo:

- The time resolution of the Veto electronics and reconstruction method. This is of order ~ 0.5 ns, as seen in Figure 4.22;
- The time of propagation of scintillating light from point of emission to the silicon photomultiplier (SiPM). Since the Veto bars are readout from only one end, at the bottom of the bar, light emitted at the top must travel 178 mm through the wavelength shifting fibre, which has a refractive index of 1.6. This gives up to 0.95 ns delay between particles emitted at opposite ends of the bar;
- The decay time of re-emission of light in the wavelength shifting fibre, approximately 2.7 ns [101].

With regards to the second point, it should be noted that, as has been seen in Figure 6.1d and discussed previously, both final state particles from Bremsstrahlung are emitted at very small angles to the beam. This means that Bremsstrahlung positrons enter the magnetic field with very little transverse momentum and therefore arrive in the centre of the PVeto bar. Therefore, the time that scintillation light from Bremsstrahlung positrons takes from the point of impact to the SiPM is relatively constant and is included in the correction for the cables/reconstruction effects discussed in Section 4.2.5. In the case of Bhabha scattering, the accepted particles are emitted with larger angles to the beam, as shown in Figure 6.16. This transverse momentum means that the magnetic field causes a deflection in Y, which may cause a delay in arrival time of the scintillation light produced. This effect is demonstrated in Figure 6.22, which shows the position in Y of particles entering the Vetoes, studied using the Monte Carlo swimmer. The distribution in Y of positrons coming from Bremsstrahlung events is strongly peaked in the centre of the bar, while Bhabha events are mostly distributed at the edges of the bars. The fact that the Bhabha distributions do not have a sharp peak also means that this effect cannot be corrected for a posteriori, since the Y position can be neither measured or assumed.

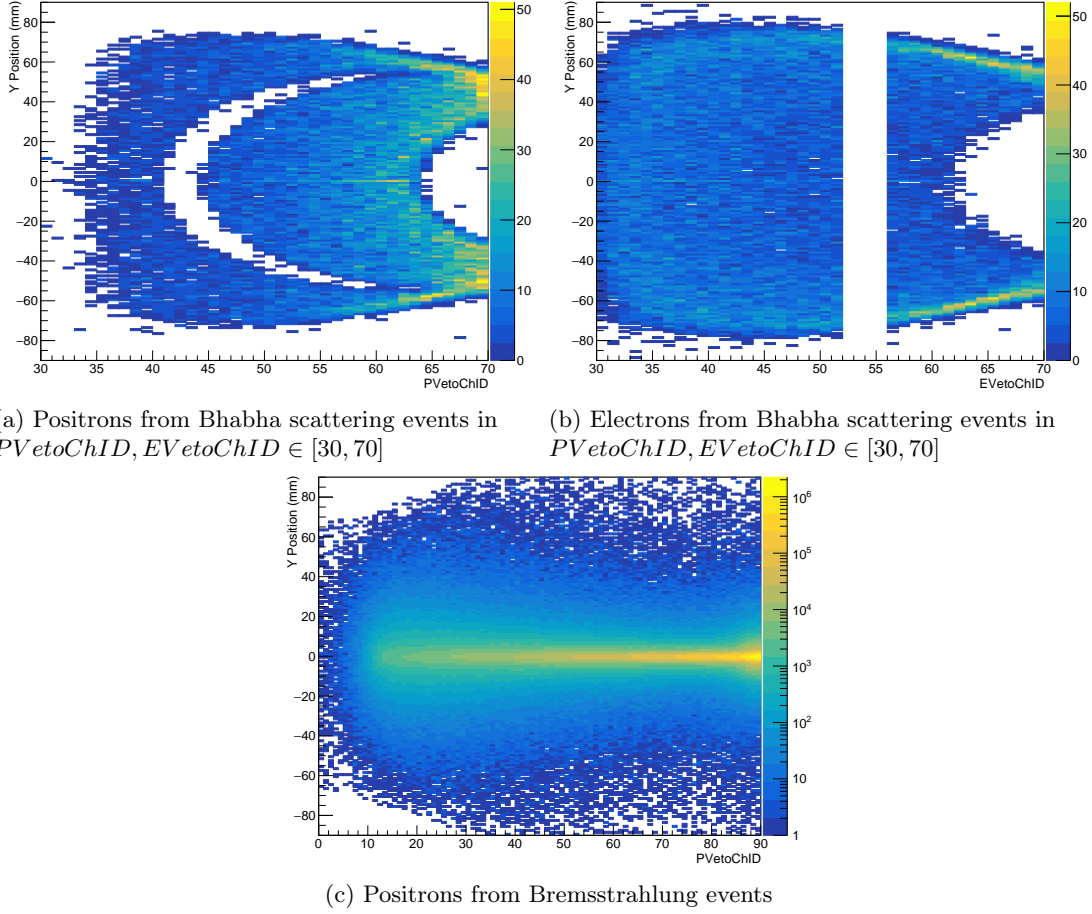


Figure 6.22: Y position, given by MC swimmer, of positrons entering the PVeto (Figure 6.22a) and electrons entering the EVeto (Figure 6.22b) from Bhabha events which enter the geometrical acceptance $PVetoChID, EVetoChID \in [30, 70]$, and of positrons entering the PVeto from Bremsstrahlung events (Figure 6.22c).

The third point in the list above creates a difference between Bremsstrahlung and Bhabha scattering not only due to the fact that using two Vetoes means introducing this uncertainty twice, but also due to the topology of the two processes: Bremsstrahlung has very highly boosted positrons which are deflected relatively little by the magnetic field, which therefore enter the PVeto at much shallower angles, passing through more scintillating bars before leaving the detector. In Bhabha scattering, the angular distribution of the electron that enters the detector does not peak at small angles, as seen in Figure 6.1a, meaning that it enters the magnetic field at a higher angle to the beamline than a positron from Bremsstrahlung. This means that the particle enters the Veto at a sharper angle and hits fewer bars, creating shorter clusters. Since the cluster time is the average of the times of the individual hits, the variation in emission time is lower in Bremsstrahlung than in Bhabha scattering.

These effects are summarised in Figures 6.23 and 6.24, made using a toy Monte Carlo to estimate the impact of each effect individually. The toy Monte Carlo simulated the difference in time between particles observed in the PVeto, EVeto and the SAC, due only to the resolution of each detector. The SAC resolution was simulated as $\sim \text{Gaus}(0, 0.15)$ ns, while the Vetoes had three components simulated: $\text{Gaus}(0, 0.4)$ ns for the electronics resolution, $U(-1, 1)$ ns for the relative distances from the SiPM and $\exp(-1/2.7)$ ns for the time of emission of the fibre. Figure 6.23 shows the resolution of Bremsstrahlung events from this toy assuming only one PVeto scintillating bar was hit (blue) and assuming a cluster of two scintillating bars in the PVeto. Figure 6.24 shows the effect of only the wavelength shifting fibre in events with one bar

hit in each Veto (red) and the combination of this effect with the resolution of the electronics and the distance to the SiPMs (blue).

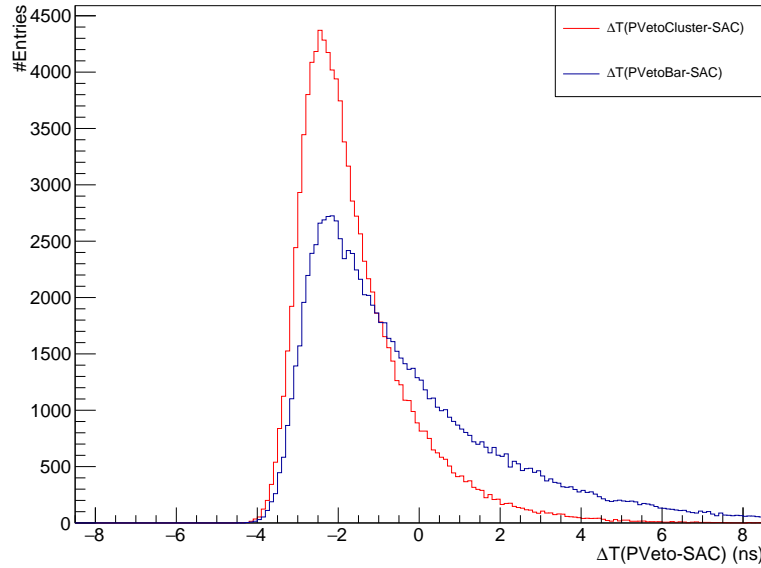


Figure 6.23: Difference in time between PVeto and SAC assuming only detector resolutions. The SAC resolution is given by $\text{Gaus}(0,0.15)$ ns, whereas the PVeto resolution comes from a $\text{Gaus}(0,0.4)$ ns summed with an exponential $\exp(-1/2.7)$ ns to represent the time of emission of the fibre. Blue is assuming a single scintillating bar, red is assuming two scintillating bars.

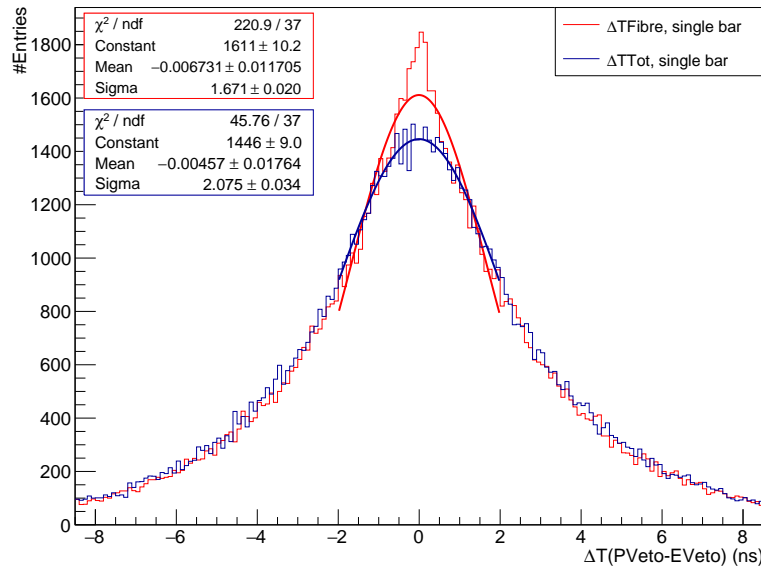


Figure 6.24: Difference in time between PVeto and EVeto assuming only detector resolutions. Red shows the difference only due to the fibre while blue shows the effect of the fibre combined with the distance from the SiPM and an intrinsic 0.4 ns Gaussian resolution.

The combination of the difference in time with the topology of final states at PADME gave rise to the distinctive, three-pronged “trident” distribution seen in Figure 6.25, while the exponential decay time of the fibre smears the distribution and worsens the resolution, leading to the wide and non-Gaussian shape of Figure 6.21b.

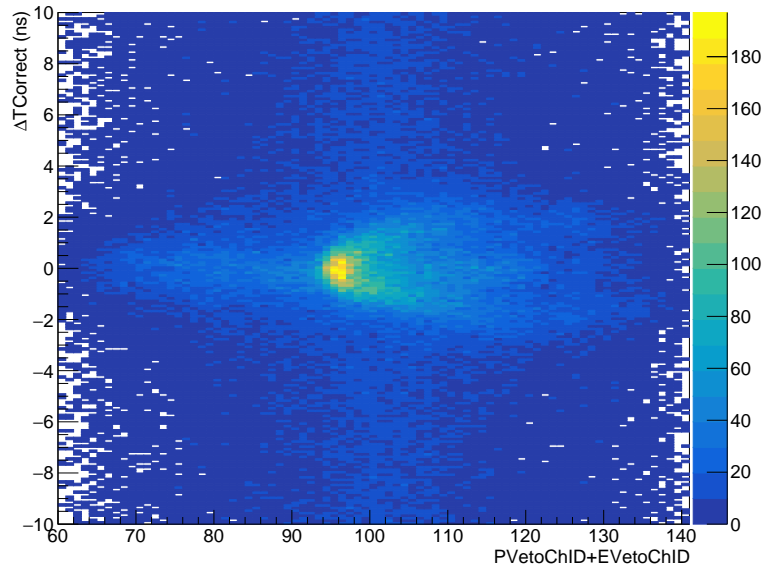


Figure 6.25: Sum of channels $PVetoChID + EVetoChID$ vs corrected time difference for clusters in data.

Since the experimental acceptance for Bhabha scattering was calculated using the Monte Carlo, it is extremely important that any cuts applied to the data have a well reproduced impact on the Monte Carlo as well. Since the distributions outside of the peak in Figure 6.21b are relatively flat, it was considered that background subtraction would be relatively straightforward and would introduce less systematic uncertainty than a poorly controlled cut in the centre of the peak. Therefore, the cut on $\Delta T(PVeto - EVeto)$ was kept as wide as was reasonably possible and events were selected which had a cluster in each Veto arriving in the range $PVetoChID, EVetoChID \in [30, 70]$ within 5 ns of each other.

The distribution of these events in channel sum is given in Figure 6.26. Compared to the swimming of Monte Carlo events shown in Figure 6.14, the large tail on the left hand side demonstrates that there's still a significant background component to this measurement. The background sources are listed in Section 6.5, and their treatment is discussed in depth in Section 6.6.

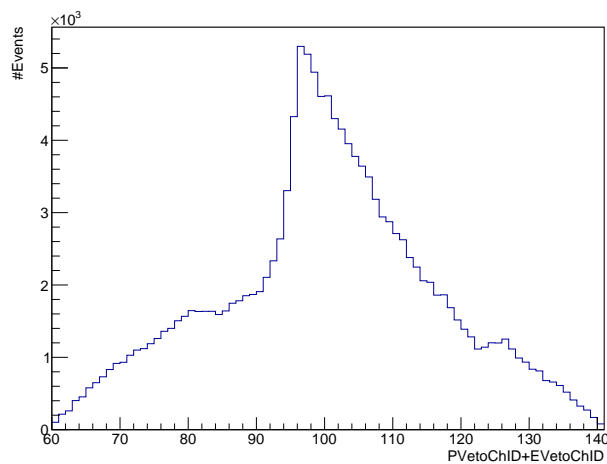


Figure 6.26: Channel sum $PVetoChID + EVetoChID$ for events in Run 30660 with $|\Delta T(PVeto - EVeto)| < 5$ ns.

6.4 NPoT and Data Quality

PADME was designed to use the active diamond Target as a luminosity monitor. The development, characterisation and reconstruction of this detector were the subject of Federica Oliva's 2021 PhD thesis [90] and are beyond the scope of this work. It is important to note, however, that since the experiment was designed to operate between 27k–28k PoT/bunch, most of the reconstruction efforts were focussed around this level of multiplicity. This means that, while in the $e^+e^- \rightarrow \gamma\gamma$ measurement the total uncertainty on the total number of positrons on Target (NPoT) was 4% [102], in the analysis presented in this chapter the uncertainty is expected to be higher, not least due to a lower ratio of signal to noise in the graphite strips of the Target.

The Target calibration was performed using special data sets which had varying multiplicities, as measured by the BTF Calorimeter. The results of these runs can be seen in Figure 6.27 for two different conditions: when the beam hit only one X strip of the target and when the target was positioned so that the beam hit between two strips. Since at the time of writing it's not clear exactly what the conditions were in the data set used for this analysis (Run 30660), the uncertainty on the total charge collected in the X view is taken to be the relative difference between the measurements shown in green and yellow respectively. At 4.5k PoT/bunch it can be seen that this value is of order 10%. Since the Target reconstruction used in this analysis relied on the average of the charge collected on the X and Y views of the Target, this difference produces a systematic uncertainty on NPoT which translates into a systematic uncertainty on the cross section. This difference should be reducible by calibrating NPoT using the beam monitoring system introduced in Run 3, since the beam conditions in Run 3 were very similar to those in the data sample used in this analysis.

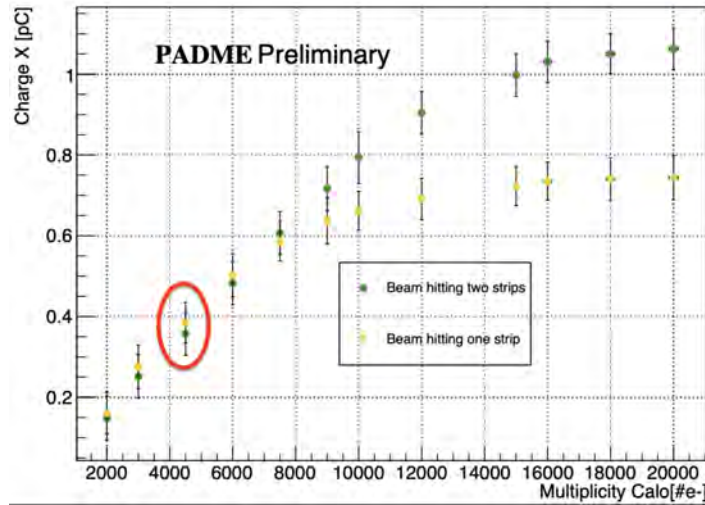


Figure 6.27: Total charge reconstructed by Target as a function of NPoT from [90]

The distribution of NPoT/bunch over the full run in Run 30660 given by the current Target reconstruction is shown in Figure 6.28a. The data taken at PADME is split into 5 streams, and data files are saved into one of these five streams every 1000 bunches. Taking just one of these streams gives a fifth of the data set across the whole run where the file number of the data file is an easy way to access the time ordering of the events. As can be seen in Figure 6.28, using the whole run or only using one fifth, the mean and sigma remain stable, validating the use of only the one stream for beam stability and data quality studies.

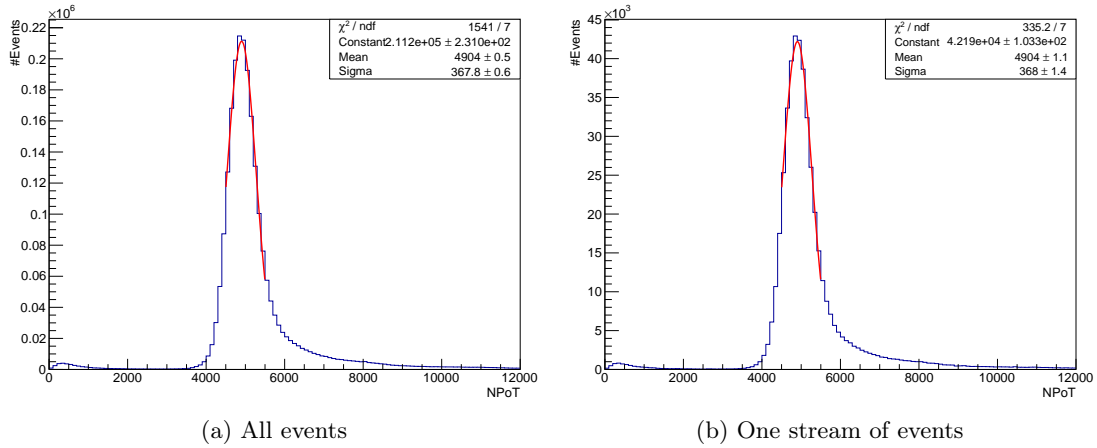


Figure 6.28: NPoT per bunch in all events of Run 30660 and in the single stream considered for the data quality and beam stability studies.

In Figure 6.28 there is a second peak around zero, leading to the conclusion that the pedestal was not being subtracted correctly. This peak was fitted, as shown in Figure 6.29, and the resulting MPV of 369 (± 11) was then subtracted from NPoT a posteriori, giving the distribution seen in Figure 6.30.

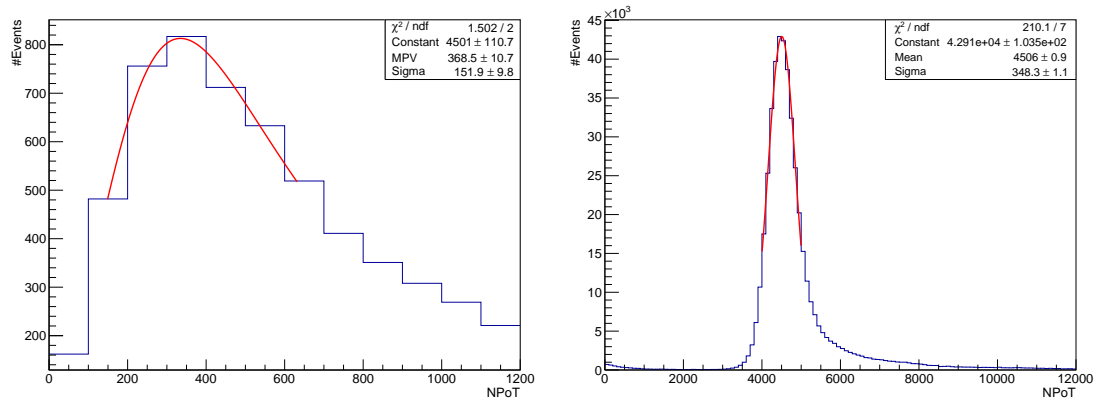


Figure 6.29: Pedestal of NPoT in Run 30660 Figure 6.30: NPoT in one stream of events of Run 30660, with pedestal subtracted

Taking the most probable value of NPoT per 1000 events and subtracting 369, the beam stability can be seen in Figure 6.31. It's clear to see here that all but 14 files have a modal NPoT between 4.0k and 5.0k, shown by the red bands. This shows that the beam staff were able to keep the multiplicity of the beam very stable over the whole course of the run.

Bunches with $<3k$ PoT were considered to have no beam and were not considered in this analysis.

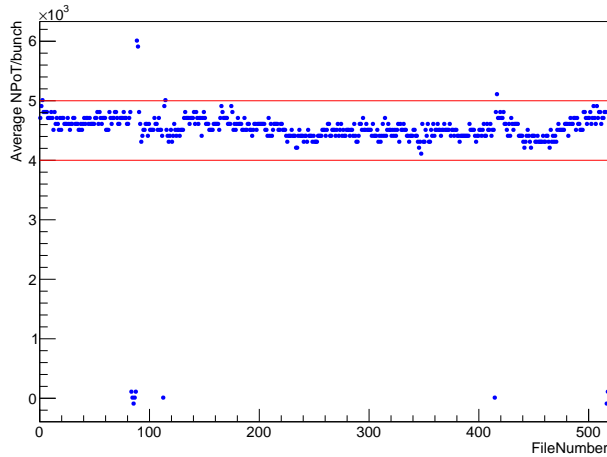


Figure 6.31: Average NPoT per 1000 events of Run 30660, with pedestal subtracted.

As has already been noted, the Bhabha scattering acceptance is highly dependent on the angle with which the particle enters the magnetic field. If the beam were off-axis in the data, particles would enter the magnetic field with an angle which would be poorly controlled between data and MC, resulting in a poorly estimated acceptance. This means that the stability of the beam angle and its reproducibility between data and Monte Carlo are important indications of data quality.

This angle can be measured by studying the weighted centre of two annihilation photons, known as the ‘‘Centre of Gravity’’ (CoG), given by Equation (6.4)

$$CoG_x = \frac{x_{\gamma_1} E_{\gamma_1} + x_{\gamma_2} E_{\gamma_2}}{E_{\gamma_1} + E_{\gamma_2}} \quad (6.4)$$

where $x_{\gamma_{1(2)}}$ is the position of each photon in the ECal, and $E_{\gamma_{1(2)}}$ is the photon energy. Information about the validation of this technique and the commissioning of the ECal can be found in [103]. The CoG in data and Monte Carlo is shown in Figure 6.32, where it is clear to see that the centre of the distribution is in the same position, although the resolution is significantly better in the data. This is probably due to the fact that the Monte Carlo was simulated using nominal beam conditions, except the multiplicity, while in the data it is likely that the collimating slits were closed to produce the reduction in multiplicity from 28k PoT/bunch to 4.5k PoT/bunch. This results in a wider range of beam energies being accepted at the Target in the Monte Carlo than in the data, however as discussed in Section 6.9, the uncertainty on the beam energy and on its spread has minimal impact on the final cross-section. Therefore the energy spread in the Monte Carlo wasn’t reduced.

The fact that the peaks of the distributions are in the same place demonstrates that the beam angle is consistent between data and Monte Carlo, validating the use of the acceptance found in MC for the measurement on the data.

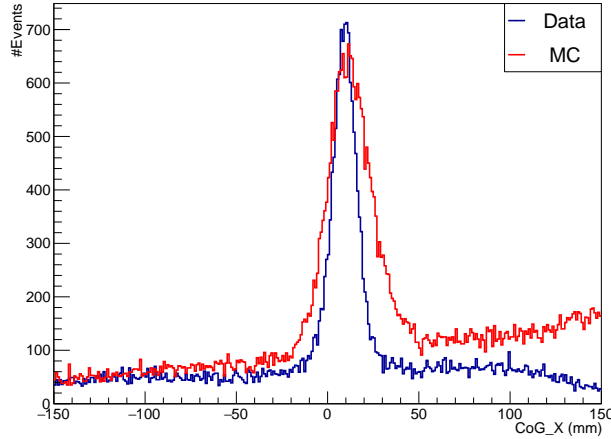


Figure 6.32: CoG in Data (blue) and in MC (red), as defined in Equation (6.4)

6.5 Backgrounds at PADME

Any process which produces a cluster in the PVeto in time with a cluster in the EVeto is a potential source of background to the Bhabha scattering measurement at PADME. The main background sources identified and studied in this work are:

- Photon background: if photons produced in $e^+e^- \rightarrow \gamma\gamma$ annihilation end up in the Vetoes, and convert to charged particles they could resemble the Bhabha signal. The discussion of this study is in Section 6.5.1.
- Beam background: off-trajectory beam particles which hit the beam pipe or particles resulting from beam interactions with the Mylar window (Figure 3.3), both of which can cause particles to enter the Vetoes. This is discussed in detail in Section 6.5.2.
- Bremsstrahlung: if a Bremsstrahlung positron is in time with an incidental cluster in the EVeto, it could have the same signature as Bhabha scattering. This is treated in Section 6.5.3.

The importance of each of these sources of background was studied using the Monte Carlo, however all eventual background subtraction was done entirely using data-driven techniques.

6.5.1 Photon annihilation background

If two photons from $e^+e^- \rightarrow \gamma\gamma$ annihilation arrived in the Vetoes, converted to charged particles and created clusters, this could potentially create a source of background for the Bhabha signal. To check the potential acceptance in the Vetoes of any photons coming from this process, a Monte Carlo simulation was created with 5×10^5 $e^+e^- \rightarrow \gamma\gamma$ annihilation events. None of the generated events created a cluster in the EVeto, therefore the contribution to the background of this source is at least two orders of magnitude below the acceptance of the Bhabha scattering signal as found in Figure 6.12. Combined with the fact that the cross section for $e^+e^- \rightarrow \gamma\gamma$ annihilation is more than 20×10^3 smaller than that of Bhabha scattering, this background is therefore considered negligible.

6.5.2 Beam background

The background to the selection coming from particles which interact outside of the Target was studied using a special “no Target” run, Run 30654. This run was taken at 28×10^3 PoT, and had the Target inserted into and removed from the beam line several times using remote controlled step motors. The extraction is a slow process and if data taking is not stopped while

it is ongoing, a significant number of beam particles can hit the Target structure while it is in an intermediate position. This risks creating additional pile-up if the beam particles hit the Target support materials and create showers.

The repeated insertion and extraction of the Target resulted in a continuous distribution of the number of positrons on Target per bunch (NPoT) which was difficult to cut on, as seen in Figure 6.33. For this reason, it was decided to cut on the number of clusters in the SAC (NClusSAC), since this number is strongly correlated with Bremsstrahlung, the most frequent physics process in the Target. This gave a much better net separation between events with and events without the Target, as shown in Figure 6.34. Given the large number of events in this sample, purity was valued over retaining more data. Therefore, it was decided to cut away events with $N_{\text{ClusSAC}} > 10$, giving the distribution of NPoT seen in Figure 6.35. It can be seen from Figure 6.35 that applying the cut on the number of clusters in the SAC removes the peak in NPoT at 28k, implying that the data taken with the Target fully or partially in the beamline have been removed successfully.

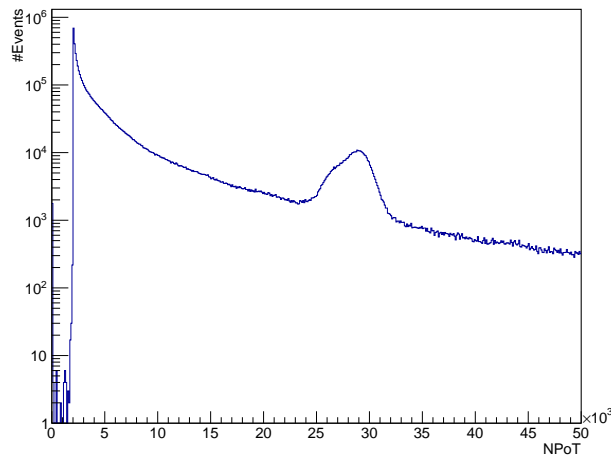


Figure 6.33: Number of positrons on target per bunch (NPoT) in “No-Target” Run 30654.

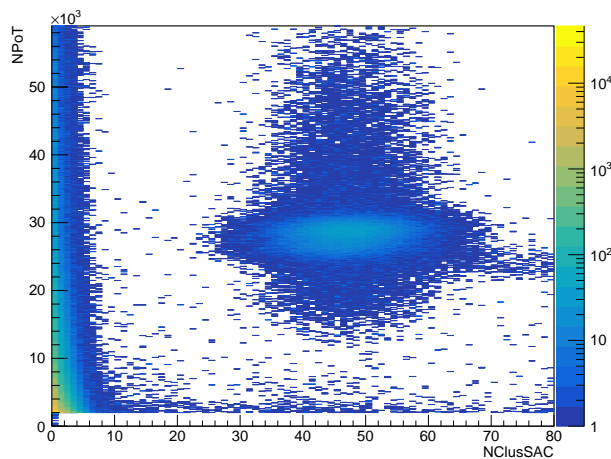


Figure 6.34: Number of clusters in SAC vs number of positrons on target per bunch (NPoT) in “No-Target” Run 30654.

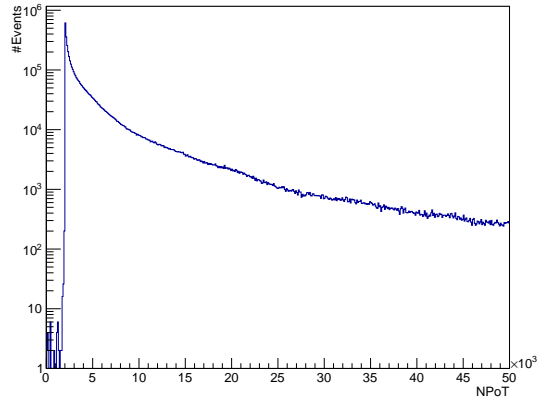


Figure 6.35: Number of positrons on target per bunch (NPoT) in “No-Target” Run 30654 after cutting events with $N_{\text{clusSAC}} > 10$.

Since the full data sample used in this analysis was taken at 5k PoT/bunch, the use of a run taken at 28k PoT/bunch to study the beam background was validated using the Monte Carlo. A Monte Carlo sample with 5k PoT/bunch was generated and compared to the no-Target Monte Carlo sample eventually used for the analysis which was taken with a beam multiplicity of 28k PoT/bunch. As can be seen in Figure 6.36, the two samples showed excellent agreement in the shape of the distribution of clusters per channel throughout the entire region of interest. This gave confidence that Run 30654 which had a multiplicity of 28k PoT/bunch could be linearly scaled to the low intensity conditions $\sim 5\text{k PoT/bunch}$ in Run 30660, used in this analysis.

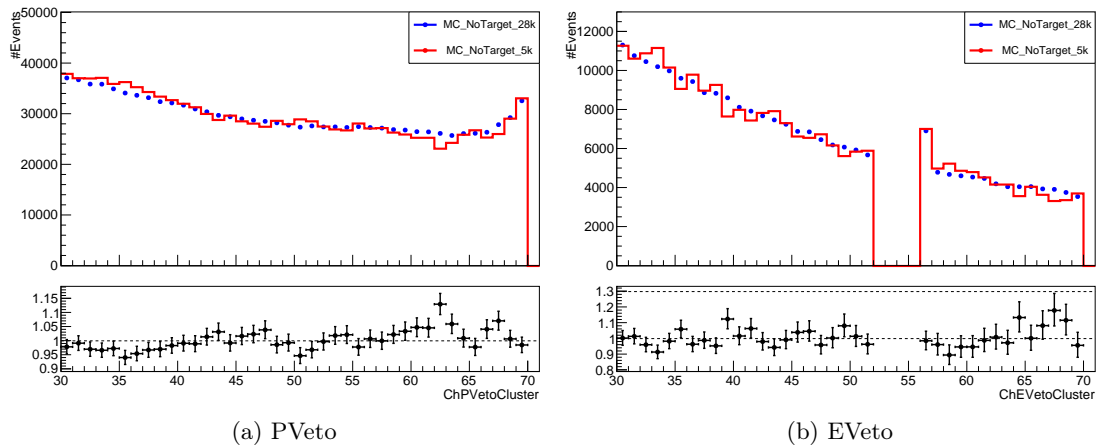


Figure 6.36: Veto occupancy in MC samples without target with 5k PoT/bunch multiplicity (red) and 28k PoT/bunch (blue). The 5k poT/bunch sample is normalised to the integral of the 28k PoT sample: a factor of 24 for the PVeto and a factor of 25 for the EVeto.

As discussed in Section 6.6, the treatment of the beam background in the full Bhabha scattering analysis normalised the number of events found in the no-Target run to the full run. This means that how the absolute scale of the beam background sample varies with NPoT/bunch has no effect on the final background subtraction.

6.5.3 Bremsstrahlung background

With a high flux of particles in both Vetoes, the probability of a positron from Bremsstrahlung being in time, by chance, with a cluster in the EVeto is not negligible. Although Run 30660, the run used in this analysis, had a multiplicity of $\sim 5\text{k PoT/bunch}$, much lower than the

nominal value of 27–28k PoT/bunch, selecting events which have a cluster in the PVeto and a cluster in the EVeto in time within 5 ns did not completely reduce the background coming from Bremsstrahlung. This can be seen in Figure 6.37 which shows the distribution of the difference in time $\Delta T(PVeto - SAC)$ between clusters in the PVeto and clusters in the SAC plotted against the sum of energies of positrons entering the PVeto and clusters in the SAC, for PVeto clusters which have already been selected using the Bhabha scattering selection.

Both the time difference between the detectors and the energy of the positron were reconstructed assuming the positron came from Bremsstrahlung, that is:

- ΔT was corrected for the time of flight of Bremsstrahlung positrons given in Figure 4.21;
- $EPos$ is the energy of the presumed Bremsstrahlung positron, reconstructed as a function of the channel of impact by the relation found in Section 4.4;
- $ESAC$ is the energy of the SAC cluster under consideration

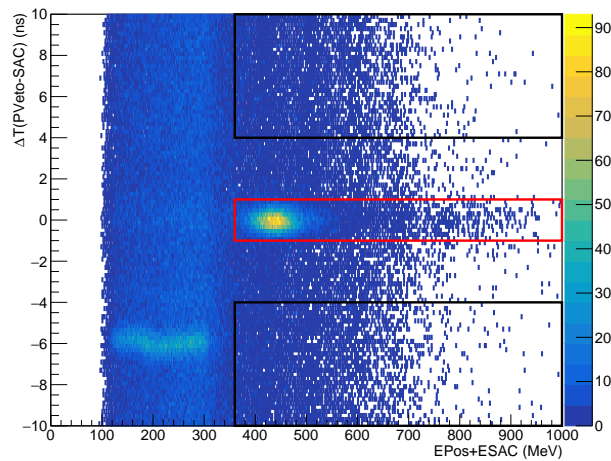


Figure 6.37: $\Delta T(PVeto - SAC)$ corrected using Bremsstrahlung trajectory vs energy sum $EPos + ESAC$ of presumed Bremsstrahlung positrons and SAC clusters, for positrons which have an in time cluster in the EVeto within 5 ns. The red box shows the “in-time” selection while the black boxes were used for the “out-of-time” selection.

The distribution shows a clear peak in the region $\Delta T = 0$ and $EPos + ESAC = 430$ MeV where Bremsstrahlung events are expected to be found. Selecting the region $|\Delta T(PVeto - SAC)| < 1$ ns and $360 \text{ MeV} < E_{PVeto} + E_{SAC} < 1000$ MeV, outlined in red in Figure 6.37, it can be seen that the distribution of the channel sum $PVetoChID + EVetoChID$ peaks in the same region as that considered for the Bhabha scattering signal and would therefore pose a significant background if not subtracted. This can be seen in Figure 6.38.

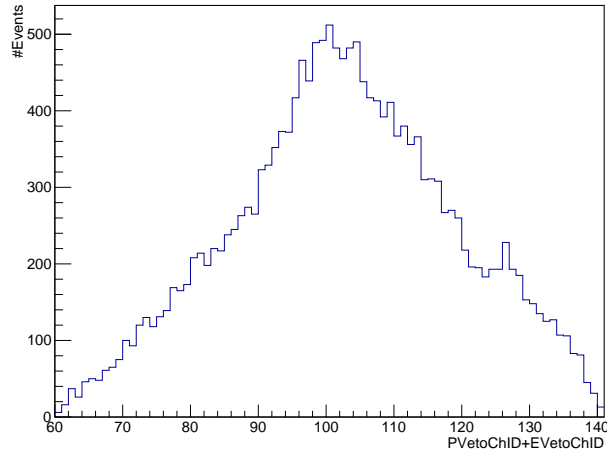


Figure 6.38: Channel sum $PVetoChID + EVetoChID$ for events which satisfy both the Bhabha time condition and the Bremsstrahlung time and energy conditions.

This selection is affected by beam background, since particles which interact outside of the Target will cause pileup in all three of the detectors used here. If the beam background to Bremsstrahlung is not subtracted before the subtraction of the Bremsstrahlung contribution itself is performed, this component of background will be subtracted twice, resulting in an over-compensation for the problem. However, when the Target is not in the beamline, the rate of Bremsstrahlung is very low meaning that the no-Target run is not a good candidate to study the beam background to the Bremsstrahlung component of the Bhabha selection. Instead, the time side-bands were used to estimate this background, specifically studying the regions with $360 \text{ MeV} < E_{PVeto} + E_{SAC} < 1000 \text{ MeV}$ and $-10 \text{ ns} < \Delta T(PVeto - SAC) < -4 \text{ ns}$ and $4 \text{ ns} < \Delta T(PVeto - SAC) < 10 \text{ ns}$ respectively, indicated in black in Figure 6.37.

Studying the distribution in channel sum of events which pass this selection, and scaling the distribution by a factor of $1/6$ to compensate for the difference in width of the time-windows considered, the resulting distribution can be seen in Figure 6.39. It is interesting to observe here that the peak at around channel 95 in this distribution strongly resembles the Bhabha signal shape. This suggests that while Bremsstrahlung creates a background to the Bhabha scattering measurement, Bhabha scattering is also present in the Bremsstrahlung selection. This reinforces the importance of separating this distribution from the Bremsstrahlung distribution in order to avoid subtracting signal events from the selection. For this reason, Figure 6.39 was first subtracted from the Bremsstrahlung distribution (Figure 6.38), giving the channel sum distribution seen in Figure 6.40, before this final “pure Bremsstrahlung” distribution was subtracted, along with the beam background distribution from the no-Target run, from the original Bhabha distribution in shown in Figure 6.26.

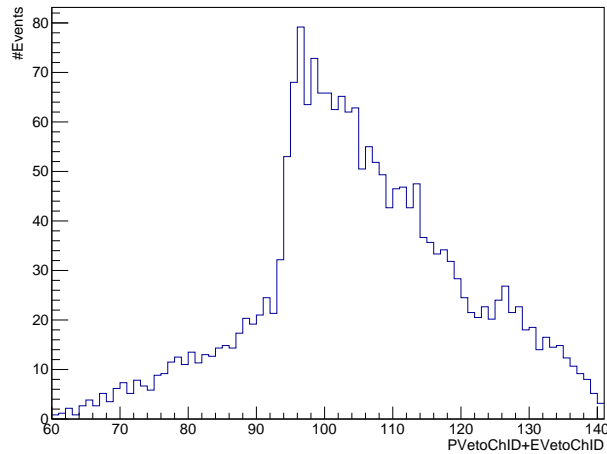


Figure 6.39: Channel sum $PVetoChID + EVetoChID$ for events which satisfy both the Bhabha time condition and have a positron out of time with a SAC cluster. Plot scaled by a factor of $1/6$.

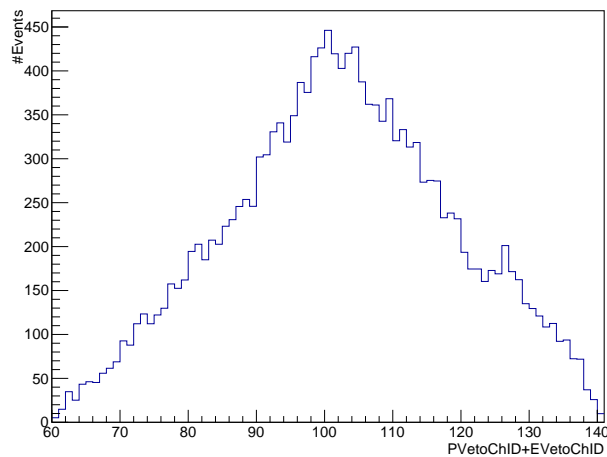


Figure 6.40: Channel sum $PVetoChID + EVetoChID$ for “pure Bremsstrahlung”: events which satisfy both the Bhabha time condition and the Bremsstrahlung time and energy conditions, with the background from the Bremsstrahlung time side bands subtracted.

6.6 Background subtraction

As discussed in the previous sections, the final measurement of the number of Bhabha scattering events was taken from the integral of the channel sum in the region $PVetoChID + EVetoChID \geq 90$, after subtracting the backgrounds.

The four distributions used in this analysis are shown in Figure 6.41. Here, all four samples used in the analysis (Data and MC both with and without Target) have been scaled to the number of positrons on target (NPoT) in the full Target sample.

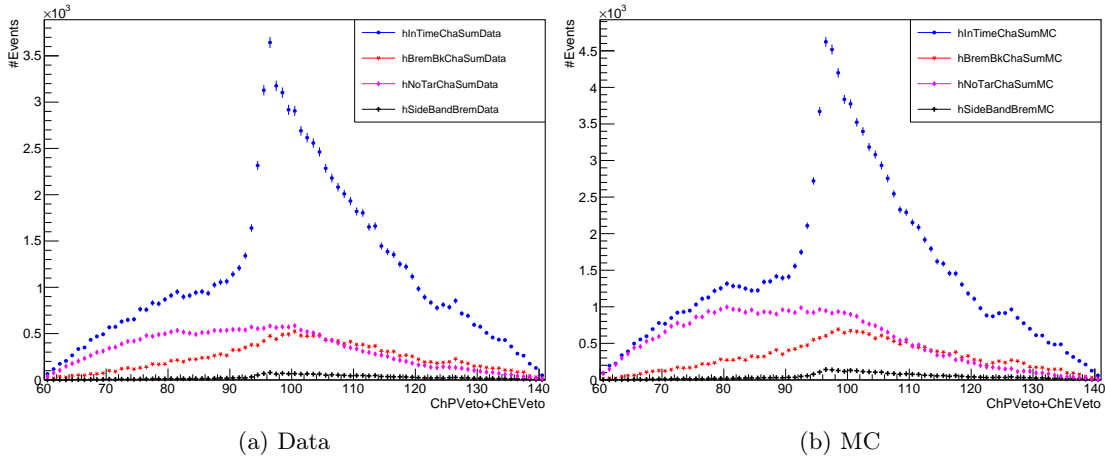


Figure 6.41: Channel sum $PVetoChID + EVetoChID$ for the distribution containing the signal and the distributions considered in the background subtraction. All samples have been scaled to NPoT in the full Target Data sample.

The background subtraction is performed in the following way:

- First, the Bremsstrahlung side band distribution (" $hSideBandBremData$ ", black crosses in Figure 6.41) is subtracted from the full Bremsstrahlung distribution (" $hBremBkChaSum$ ", red stars);
- Then, the beam background (" $hNoTarChaSum$ ", pink diamonds) and the resulting "pure Bremsstrahlung" distribution are subtracted from the full data distribution from the full Target run (" $hInTimeChaSum$ ", blue points)

The second step of this process comes with the difficulty that, while the Bremsstrahlung distributions (red and black) are sub-samples of the full Target distribution and therefore are automatically normalised to the full Bhabha signal distribution (blue), the beam background from the no Target run (pink) comes from a data sample which, by definition, has no Target to act as a luminosity monitor. This means that it is very difficult to know with precision how many particles there were per bunch for every bunch in this sample. Since the physics trigger used by PADME is provided by the arrival of the beam, with no information from the target it is difficult to know whether at any point the LINAC stopped sending bunches to PADME without removing the trigger. Both of these factors cause significant uncertainties in the number of positrons being sent to PADME in the no-Target run and therefore exactly what the normalisation constant for this run should be.

This is obviously not the case in the Monte Carlo, and leads to the background subtraction being much more efficient in the Monte Carlo than in the data as seen in the distribution in Figure 6.42, for channel sum < 90 .

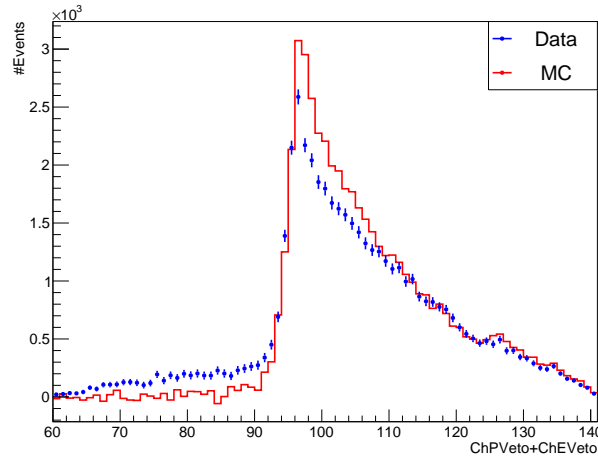


Figure 6.42: Channel sum $PVetoChID + EVetoChID$ with background distributions subtracted after being scaled to the number of PoT considered in each sample in data (blue) and MC (red).

This led to a more refined strategy for scaling the no Target background distributions which used the integral of the first 10 bins of the blue and pink distributions in Figure 6.43, where the blue is the resulting distribution from the pure Bremsstrahlung subtraction of the full blue distribution in Figure 6.42 and the pink is again the no Target background distribution, however with no scaling factor applied.

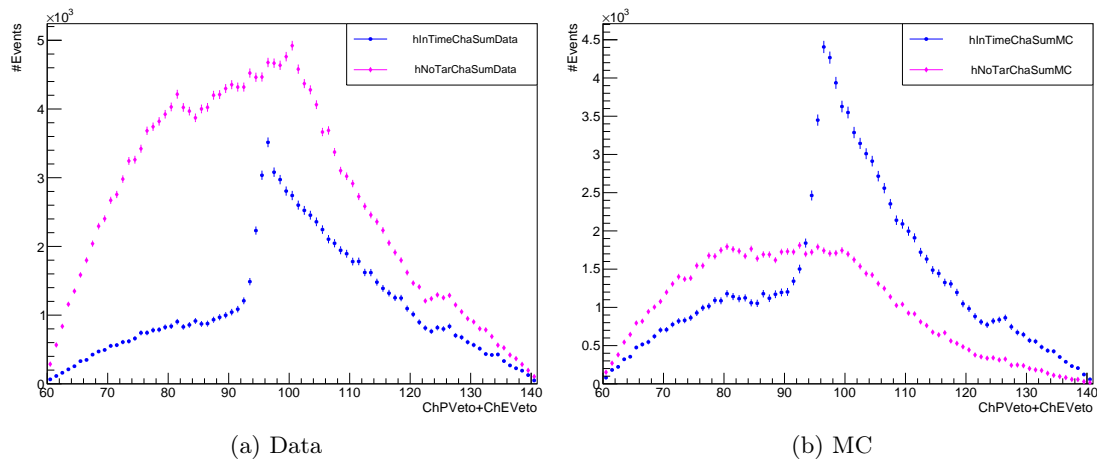


Figure 6.43: Channel sum $PVetoChID + EVetoChID$ for the Bremsstrahlung-subtracted full target distribution (blue) and the no target distribution (pink), with no scale factors applied.

This new normalisation strategy relies on the fact that, as seen in Sections 6.1.1 to 6.1.3, the number of events expected to the left of the peak in channel sum is expected to be essentially zero. Therefore, once the Bremsstrahlung background component has been subtracted, the beam background component must be scaled so that it makes the integral of bins to the left of the peak zero. Here, only the first 10 bins ($60 \leq PVetoChID + EVetoChID \leq 69$) were used to carry out this process. If the strategy is successful, the other bins between the 10th and the peak should also go to zero automatically.

Figure 6.44 shows the signal histogram with Bremsstrahlung already subtracted and the beam background histogram scaled to the integral of the first 10 bins of the signal histogram, scale constants of 0.20 ± 0.004 and 0.61 ± 0.012 in data and MC respectively. It can be seen here that in both cases, the left hand side of the distribution is reproduced very well, not

only in the first 10 bins but also in the following 10 to 15, in values of channel sum between $70 \leq PVetoChID + EVetoChID \leq 79$ to 85.

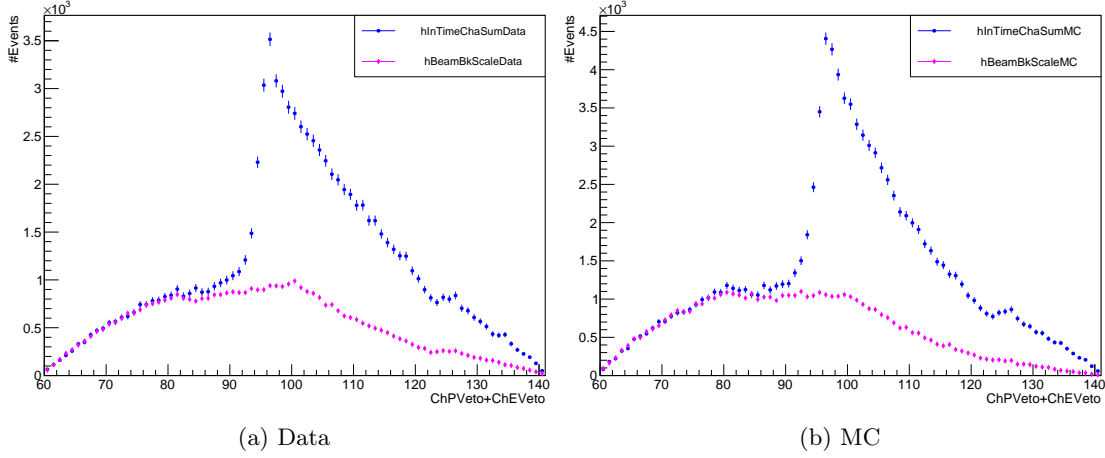


Figure 6.44: Channel sum $PVetoChID + EVetoChID$ for the Bremsstrahlung-subtracted full target distribution (blue) and the no target distribution (pink), with no Target run scaled to the integral of the first 10 bins of the signal histogram ($60 \leq PVetoChID + EVetoChID \leq 69$).

6.7 Results and cross checks

The background subtraction process described in the previous section gives the comparison between data and MC shown in Figure 6.45.

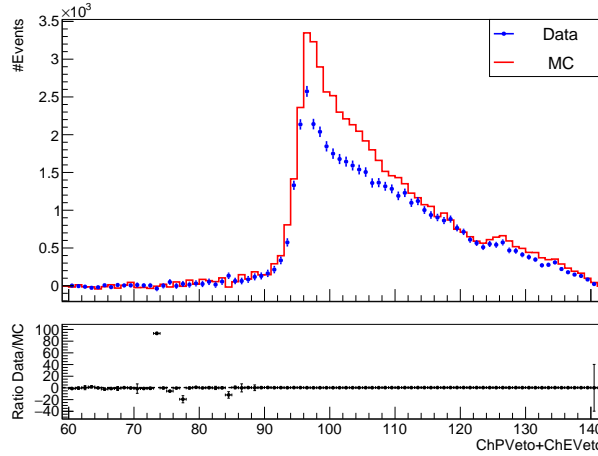


Figure 6.45: Channel sum $PVetoChID + EVetoChID$ with background distributions subtracted after being scaled using integral of left hand sides of distributions.

To evaluate the error on the ratio, each of the four samples used in this analysis was split into eight and the background subtraction was performed on each of the eight sub-samples. The ratio between data and Monte Carlo was then calculated for each sub-sample and the standard deviation was used as the error on the ratio shown at the bottom of Figure 6.45.

It can be seen here that the height of the peak is different in data and MC. This difference can be seen more clearly in Figure 6.46 which shows the background-subtracted distribution in data and MC, zoomed to $PVetoChID + EVetoChID \geq 90$.

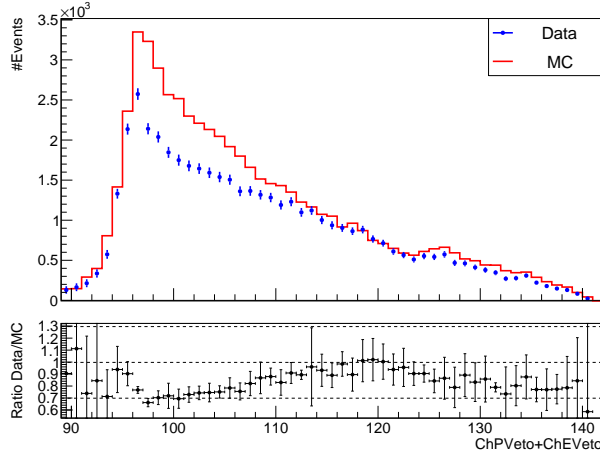


Figure 6.46: Channel sum $PVetoChID + EVetoChID$ with background distributions subtracted, zoomed to $PVetoChID + EVetoChID \geq 90$.

Integrating the signal distributions in the range $PVetoChID + EVetoChID \geq 90$ gives 46,148 Bhabha signals found in the data and 56,934 signals found in the MC when scaled to NPoT in the data. This gives a ratio of 0.81.

This difference could come from several sources, including:

- too many Bhabha scattering processes being simulated by Geant4 which, as discussed in Section 2.1, only contains tree-level calculations;
- too many Bhabha scattering processes simulated due to the Target density in the MC being that of pure diamond, instead of the mix of diamond and graphite used in the data, leading to a 3% overestimate of the number of electrons in the Target;
- the Bhabha scattering acceptance being artificially high when not considering radiative corrections, as in the case of Geant4;
- NPoT in the data being overestimated, leading to the MC distribution being scaled by a value of $NPoT_{Data}/NPoT_{MC}$ which is too high.

Studying the number of Bremsstrahlung signals being subtracted from the Bhabha acceptance gives a good indication of the analysis strategy since the two distributions will be affected in exactly the same way by uncertainties on the NPoT. This means that taking the ratio of these measurements will result in a comparison which is free from this uncertainty.

The numbers of events of these two processes and the ratio of their rates in data compared to MC are presented in Table 6.2

Table 6.2: Number of presumed Bhabha events found in Data and MC and number of presumed Bremsstrahlung events found within Bhabha selection in Data and MC, and ratio of Data to MC and ratio of Bhabha events to Bremsstrahlung events in Data and MC, and ratio of these ratios. Errors are statistical.

	Data	MC	Ratio
Bhabha	$46,148 \pm 354$	$56,934 \pm 402$	0.811 ± 0.0082
Bremsstrahlung	$60,376 \pm 161$	$77,644 \pm 181$	0.778 ± 0.0028
Ratio	0.764 ± 0.0062	0.733 ± 0.0054	1.04 ± 0.011

This shows that the while the rates of Bhabha scattering and Bremsstrahlung within the Bhabha acceptance differ between data and MC by between 20-25%, the relative rates of these

processes differ only by $\sim 4\%$ between data and MC. This leads to the inference that the analysis process is being applied consistently between data and MC, and therefore the difference between them is due to a problem with normalisation.

6.8 Cross-section calculation

The number of signal candidates observed (N_{Obs}) can be transformed into a cross section σ according to Equation (6.5)

$$\sigma = \frac{N_{Obs}}{N_{PoT}} \frac{1}{Acc} \frac{A_C}{N_A Z_C \rho d} \times 10^{36} \quad (6.5)$$

Where:

- $N_{PoT} = 1.03188 \times 10^{10}$ is the total number of positrons on target acquired in the sample under study
- Acc , evaluated below, is the experimental acceptance, defined as the number of Bhabha scattering candidates in the MC sample divided by the total number of Bhabha scattering events produced
- $A_C = 12$ is the atomic mass of the ^{12}C used in the Target
- $N_A = 6.022 \times 10^{23}$ is Avogadro's number
- $Z_C = 6$ is the atomic number of the ^{12}C used in the Target
- $\rho = 3.2$ is the effective density of the Target in g/cm^3
- $d = 0.0097$ is the thickness of the Target in cm
- 10^{36} is a factor which converts between cm^2 and pb

Given that the full target MC sample is scaled by 0.99 times to have the same number of NPoT as the full target data sample, Acc is:

$$Acc = \frac{56,934}{4.48911 \times 10^7 \times 0.99} = 0.0013$$

Applying this equation to the number of signal candidates observed, the final Bhabha cross-section $\sigma(e^+e^- \rightarrow e^+e^-)$ measured in PADME Run 2 is:

$$\sigma(e^+e^- \rightarrow e^+e^-) = (3.90 \pm 0.030_{stat} \pm 0.39_{sys}) \times 10^{11} \text{ pb}$$

compared to that found in the Geant4 simulation of

$$\sigma(e^+e^- \rightarrow e^+e^-)_{G4} = (4.078 \pm 0.0288_{stat}) \times 10^{11} \text{ pb}$$

The full treatment of the systematic errors is shown in the following section.

6.9 Systematic uncertainties

As discussed in Section 6.4, the uncertainty on NPoT is currently approximately 10%. This was expected to be the dominant source of systematic error, however other potential sources are discussed here.

Varying the value of the $PVetoChID + EVetoChID$ above which the integral is calculated between 84-94, gives a systematic variation on the final measurement of the cross section of order $O(0.1\%)$, lower than the statistical error on the point at $PVetoChID + EVetoChID = 90$, as seen in Figure 6.47.

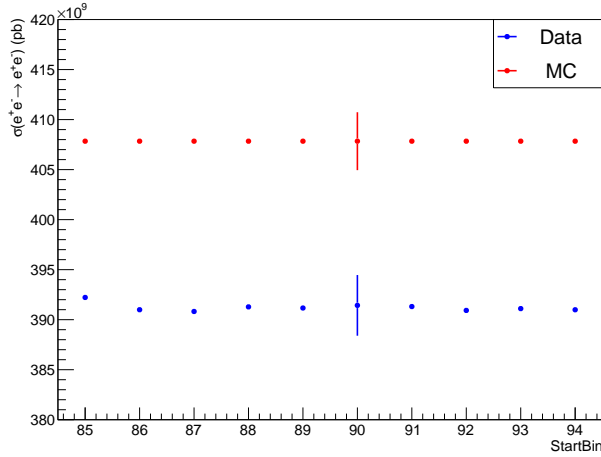


Figure 6.47: Cross section measurement as a function of the minimum value of $PVetoChID + EVetoChID$ considered in the acceptance in data (blue) and MC (red). The error bar is the statistical error on the cross section evaluated integrating over $PVetoChID + EVetoChID \geq 90$.

The effect on the final cross-section of the cut in the difference in time $\Delta T(PVeto - EVeto)$ was also studied. Halving this from 5 ns to 2.5 ns implies a higher level of confidence that the events passing the selection came from the same event at the Target. The resulting distribution of the channel sum can be seen in Figure 6.48.

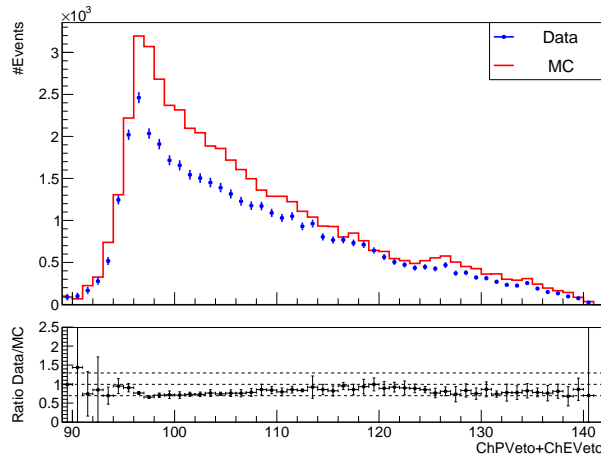


Figure 6.48: $PVetoChID + EVetoChID$ for events with $|\Delta T(PVeto - EVeto)| < 2.5$ ns in data (blue) and MC (red).

Taking the integral of events with $PVetoChID + EVetoChID$ with the more stringent cut gives a cross section $\sigma(e^+e^- \rightarrow e^+e^-)$ of:

$$\sigma(e^+e^- \rightarrow e^+e^-) = (3.83 \pm 0.028_{stat} \pm 0.38_{sys}) \times 10^{11} \text{ pb}$$

a difference of 2% compared to the result with the more permissive cut in $\Delta T(PVeto - EVeto)$.

It should also be noted that the thickness of the Target is 97 μm on average across its entire surface, however the surface is only smooth to the level of $\sim 1\mu\text{m}$. This produces a systematic error in the thickness of the Target (d in Equation (6.5)) at the point of impact in this analysis of O(1%). Moreover, as described in Section 3.2.1, the Target has graphitised strips on both sides. The exact thickness of these strips is in the range 5-10 μm per side, making 10-20 μm total. The analysis presented here used the average of this range at 7.5 μm per side, reducing

the Target density from the density of diamond (3.515 g/cm^3) to the average value of 3.2 g/cm^3 used in Equation (6.5). The uncertainty on the thickness of the graphite strips translates into a systematic error on the cross section of 2%.

The last source of systematic error considered here is the true beam energy, which would produce an uncertainty on the theoretically expected value of the cross section. The beam energy spread in Run 2 was known with a precision of approximately 1 MeV [89]. For this analysis, the effect of a 4 MeV difference in beam energy was studied with CalcHEP. From 432 MeV to 436 MeV, the difference in the cross-section is less than 0.5%.

All sources of systematic error are summarised in Table 6.3.

Table 6.3: Systematic errors

Source	Percentage error
Stat	0.77 %
NPoT	10 %
$\Delta T(PVeto - EVeto)$	2 %
Target density	2 %
Target thickness	1 %
PVetoChID+EVetoChID cut	0.5 %
Beam energy	< 0.5%

Combining the systematic errors gives a final systematic error of 10.4%.

Chapter 7

Dark sector interpretations of Bhabha scattering

As discussed in Chapter 2, the observed $e^+e^- \rightarrow e^+e^-$ scattering cross-section can be reinterpreted as a limit on the parameters of mass and coupling of a potential new massive vector particle which is produced in e^+e^- annihilation and decays to e^+e^- . The work discussed in this chapter is very preliminary, but it is intended to show the type of limit that might be possible, if the systematic error on the cross-section is reduced from 10% to around 5%.

As discussed in Chapter 6, the main source of systematic error is the total number of positrons on Target (NPoT). Since at present this is a problem of the Target reconstruction software, and since in the conditions where this software has been optimised the error is of order 5%, it is believed that 5% is a reasonable goal for the conditions of the run used in this analysis as well.

The new physics model studied in this chapter starts from the work done for PADME Run 3 [98]. The model predicts a new vector boson which is produced in resonant e^+e^- annihilation and decays to e^+e^- . Since the centre of mass energy \sqrt{s} in Run 3 was ~ 17 MeV, the Standard Model kinematic processes available to any new particle would be identical to those available at $\sqrt{s}=21$ MeV, the case in this analysis of data from PADME Run 2, and the relative cross-sections of these processes are expected to be very similar. For this reason, it was considered that the results obtained for PADME Run 3 can be reused for Run 2, changing only the absolute energy scale. The model maps very well onto the dark photon A' model, as well as more complex scenarios involving dark sectors. These scenarios include the protophobic models proposed in [41], as well as more general leptophilic dark sectors.

As stated in [98], the production rate of a new particle of mass $M_{A'} = 21$ MeV produced on resonance is given by:

$$\mathcal{N}_{A'} = N_{PoT} \frac{g_{Ve}^2}{2m_e} \frac{N_A d \rho Z}{A} f(E_{res}, E_+), \quad (7.1)$$

where $\mathcal{N}_{A'}$ is the number of new particles expected to be produced, N_{PoT} is the total number of positrons on Target, g_{Ve} is the coupling of the electron to the new boson, N_A is Avogadro's number, and d , ρ , Z and A are, respectively, the thickness, the density, the atomic number and the atomic mass of the Target. The function $f(E_{res}, E_+)$ is defined as:

$$f(E_{res}, E_+) = \frac{1}{\sqrt{2\pi}\sigma_E} \exp\left\{-\frac{(E_{res} - E_+)^2}{2\sigma_E^2}\right\}$$

where σ_E is the energy spread of the beam (~ 1.5 MeV)[89], $E_+ \sim 430$ MeV is the energy of the beam positron and E_{res} is the resonant energy, defined as $E_{res} = \frac{M_{A'}^2}{2m_e}$, with $M_{A'}$ being the mass of the new particle.

This function assumes that the width of the resonance of the new particle is negligible compared to the energy spread of the beam, since the expected coupling of the new particle is very

small. For the region in mass and coupling of interest to this measurement, the width of the resonance Γ is expected to be of order of a fraction of an electronvolt.

In this field it is common to quantify the coupling of the new particle to Standard Model fermions, g_{Ve} , as a fraction of the coupling of the electron to the Standard Model photon. In this way, g_{Ve} can be interpreted as the charge which would be given to the electron under the new force mediated by the vector boson A' .

At 90% confidence level, if the systematic error is reduced to 5%, the maximum possible number of events from new physics which end up in the PADME acceptance ($\mathcal{N}_{A'}^{Acc}$) that would still lead to a result compatible with the number of accepted e^+e^- events predicted by the Standard Model (\mathcal{N}_{ee}^{Acc}) will be given by:

$$\mathcal{N}_{A'}^{Acc} \leq 1.35 \times 0.05 \times \mathcal{N}_{ee}^{Acc}$$

The total number of A' produced at the experiment $\mathcal{N}_{A'}^{Tot}$ which gives $\mathcal{N}_{A'}^{Acc}$ entering the acceptance is given by:

$$\mathcal{N}_{A'}^{Tot} = \frac{\mathcal{N}_{A'}^{Acc}}{Acc}$$

where Acc is the acceptance of the A' , assumed to be identical to that of S-Channel Bhabha scattering as discussed in Chapter 2. For a 1.5 MeV energy spread at PADME Run 2 this gives the distribution shown in Figure 7.1. From this, the maximum allowable value of the coupling g_{ve} can be obtained from Equation (7.1) assuming that $\mathcal{N}_{A'} = \mathcal{N}_{A'}^{Tot}$ is the total number of A' produced.

Assuming no excess with respect to the Standard Model, this gives the expected 90% exclusion limit on the mass and the coupling shown in Figure 7.2. The solid red line indicates the limit expected from the analysis on Run 2 data, while the dashed green line shows the expected limit using the Run 3 setup. This shows clearly the improvements made to the sensitivity by changing setup.

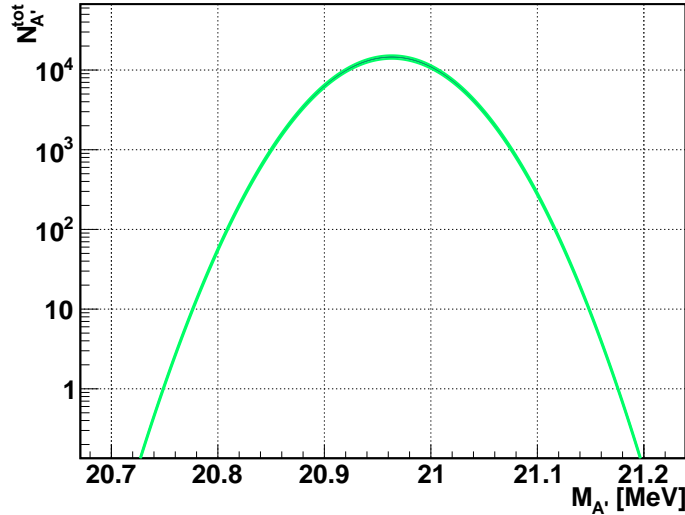


Figure 7.1: The maximum number of A' events $\mathcal{N}_{A'}^{Tot}$ which can be produced and still give a cross-section compatible with the Standard Model within 5%, as a function of the mass of the particle $M_{A'}$.

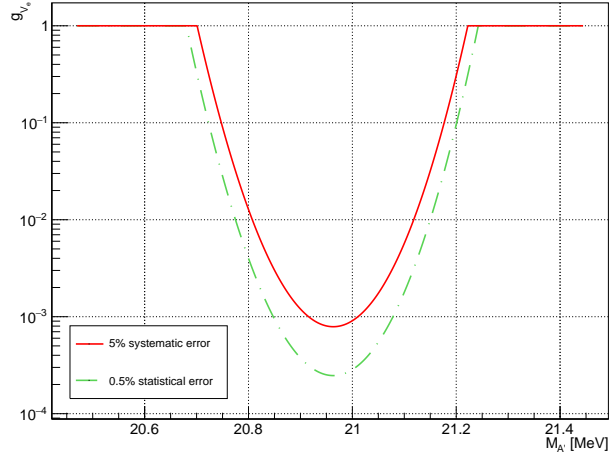


Figure 7.2: 90% exclusion limit for a vector boson of mass M'_A and electron coupling g_{V_e} which decays to e^+e^- , from a measurement of Bhabha scattering in agreement with the Standard Model within a 5% systematic error (red), or a 0.5% statistical error (green)

This result can be seen in context with other experiments in this range in Figure 7.3.

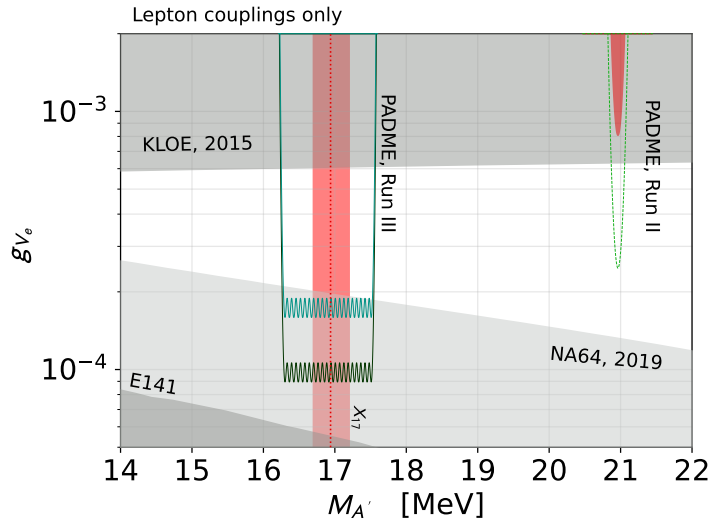


Figure 7.3: Current exclusion limits for new vector bosons with mass M'_A and electron coupling g_{V_e} from visible decay measurements. The preliminary result from this work is indicated by “PADME, Run 2” and shows in red the result assuming a 5% systematic error and in green the result assuming only a 0.5% statistical error. The expected reach for PADME Run 3 is also indicated in turquoise. The Run 3 result comes from the analysis in [98]

This work must be considered extremely preliminary, but it serves to give an impression of the type of limit that could potentially be achieved in the Run 2 data at PADME if the 10% systematic error can be reduced to 5%. It can also be seen how changing experimental strategy in Run 3 leads to a very marked improvement in predicted reach. The Run 3 strategy is described briefly in Chapter 8 and in detail in [98].

The final range of parameter space excluded by this measurement will depend on the reduction in systematic error achieved.

Chapter 8

Conclusion

This thesis has presented the measurement of the absolute cross-section of Bhabha scattering $\sigma(e^+e^- \rightarrow e^+e^-)$ at centre of mass energy $\sqrt{s} = 21$ MeV in PADME Run 2 data. The measurement is obtained as an absolute cross-section value, normalised to the number of positrons on target. This normalisation is determined independently using ionisation in the PADME target. The result obtained for the cross-section was:

$$\sigma(e^+e^- \rightarrow e^+e^-) = (3.90 \pm 0.030_{stat} \pm 0.39_{sys}) \times 10^{11} \text{ pb}$$

As far as the author of this thesis is aware, this represents the only measurement of the Bhabha scattering cross-section at $\sqrt{s} \sim \mathcal{O}(10)$ MeV since the 1950s [82], as discussed in the literature review presented in this thesis. All other, more modern measurements found in the review of the literature were performed at much higher energies and were normalised to small-angle Bhabha scattering, used as a measurement of luminosity. As such they can't be considered to be absolute cross-section measurements.

The measurement presented here is in agreement within errors with the cross-section found from the Geant4 simulation. No radiative corrections are included in the Geant4 calculation of the Bhabha scattering cross-section, which could change the calculated value of the cross-section significantly. However, it is far from trivial to understand how the radiative corrections will impact the experimental acceptance of Bhabha scattering, and the two effects may cancel. Moreover, with an error of approximately 10% on the measurement in the data, it is unlikely that the next-to-leading-order cross-section will be different enough from that at leading order to create a significant disagreement between experiment and theory.

The main source of systematic error in this analysis, as discussed in Chapter 6, is the number of positrons impinging on the Target (NPoT). This is partly due to the fact that, since the current Target reconstruction has not been optimised for this luminosity range, the data-taking conditions of the Target in the data used in this analysis are unknown. Therefore, in order to improve this measurement and reduce the systematic error, the Target reconstruction must be improved. Other sources of systematic error are at least 5 times lower and are either of the same order or smaller than that on the thickness of the Target, which may be irreducible.

Measuring the ratio of the number of observed events of Bhabha scattering to that of Bremsstrahlung, this ratio is also in agreement with the Geant4 simulation to within 4%. This measurement is independent of the systematic error on NPoT, and implies that the analysis strategy has been sufficiently well reproduced between data and Monte Carlo – crucial for the measurement of the experimental acceptance of Bhabha scattering. Since the systematic error on NPoT is the largest source of systematic error in the analysis, the result of the Bhabha/Bremsstrahlung ratio supports the hypothesis that if the error on NPoT can be reduced to $\sim 5\%$, the total systematic error on the Bhabha scattering cross section will also be reduced to this level.

To reduce the systematic errors on the Bhabha scattering cross section, the Target reconstruction software will need to be optimised for the low luminosity data sample used in the

analysis. The normalisation of the beam background in the no Target run will also need to be performed, using the SAC as a luminosity monitor, and the effects of radiative corrections to the cross section on both the total value of the cross section and to the signal acceptance will have to be undertaken.

An important implication of this work on dark sector studies at PADME is that, due to the opening angle of the two Bhabha scattering final state particles, it is very difficult to measure the cross-section of this process with $\sim 1\%$ precision using the PADME Vetoes detectors. Without being able to constrain the invariant mass of the e^+e^- pair, rejecting incidental pairs of particles is extremely difficult and therefore the background subtraction processes has to be treated purely statistically, as in this analysis.

The understanding of this experimental limitation was of fundamental importance to the experimental setup used in Run 3 which focussed on searching for the hypothetical X17 boson, proposed as an explanation for the anomalous e^+e^- spectra seen in the recent ATOMKI experiments [40–45, 98]. Having seen the difficulty of reconstructing the final state without information on the energy of the two final-state particles, it was decided that Run 3 would not use the Vetoes, but would have the magnetic field turned off and all particles sent straight down the beamline to be detected by the calorimeter system.

During Run 3, the collaboration performed a scan over the range of invariant mass of the X17, as indicated by the ATOMKI experiments. This technique had the advantage of being independent of the systematic error on the absolute scale of NPoT.

More information about PADME Run 3 can be found in [98, 104]

As discussed in Chapter 7, this work could be interpreted as a limit on the mass and coupling of a potential new vector boson which decays to e^+e^- . The final exclusion limit set will depend on the systematic error, which it is hoped will be reducible to around 5%, and on the precise value of the next-to-leading order Bhabha scattering cross-section, which is not calculable with the tools currently at the disposal of the PADME collaboration.

Bibliography

- [1] W. T. Kelvin, *Baltimore lectures on molecular dynamics and the wave theory of light*. London, Baltimore: C.J. Clay and Sons; Publication agency of the Johns Hopkins University, 1904, xxi, [1], 703 p. [Online]. Available: [//catalog.hathitrust.org/Record/011929196](https://catalog.hathitrust.org/Record/011929196).
- [2] F. Zwicky, ‘On the Masses of Nebulae and of Clusters of Nebulae,’ *The Astrophysical Journal*, vol. 86, p. 217, Oct. 1937. DOI: 10.1086/143864.
- [3] H. W. Babcock, ‘The rotation of the Andromeda Nebula,’ *Lick Observatory Bulletin*, vol. 498, pp. 41–51, Jan. 1939. DOI: 10.5479/ADS/bib/1939LicOB.19.41B.
- [4] V. C. Rubin and J. Ford W. Kent, ‘Rotation of the Andromeda Nebula from a Spectroscopic Survey of Emission Regions,’ *The Astrophysical Journal*, vol. 159, p. 379, Feb. 1970. DOI: 10.1086/150317.
- [5] V. C. Rubin, J. Ford W. K. and N. Thonnard, ‘Rotational properties of 21 SC galaxies with a large range of luminosities and radii, from NGC 4605 (R=4kpc) to UGC 2885 (R=122kpc).,’ *The Astrophysical Journal*, vol. 238, pp. 471–487, Jun. 1980. DOI: 10.1086/158003.
- [6] M. S. Roberts, ‘A High-Resolution 21-CM Hydrogen-Line Survey of the Andromeda Nebula,’ *The Astrophysical Journal*, vol. 144, p. 639, May 1966. DOI: 10.1086/148645.
- [7] D. H. Rogstad and G. S. Shostak, ‘Gross properties of five scd galaxies as determined from 21-centimeter observations,’ *The Astrophysical Journal*, vol. 176, p. 315, Sep. 1972. DOI: 10.1086/151636.
- [8] M. S. Roberts and R. N. Whitehurst, ‘The rotation curve and geometry of M31 at large galactocentric distances.,’ *The Astrophysical Journal*, vol. 201, pp. 327–346, Oct. 1975. DOI: 10.1086/153889.
- [9] R. Massey, T. Kitching and J. Richard, ‘The dark matter of gravitational lensing,’ *Reports on Progress in Physics*, vol. 73, no. 8, p. 086 901, Jul. 2010. DOI: 10.1088/0034-4885/73/8/086901. [Online]. Available: <https://doi.org/10.1088%5C%2F0034-4885%5C%2F73%5C%2F8%5C%2F086901>.
- [10] M. Markevitch, ‘Chandra observation of the most interesting cluster in the universe,’ *ESA Spec. Publ.*, vol. 604, p. 723, 2006. arXiv: astro-ph/0511345.
- [11] M. Markevitch *et al.*, ‘Direct constraints on the dark matter self-interaction cross-section from the merging galaxy cluster 1E0657-56,’ *Astrophys. J.*, vol. 606, pp. 819–824, 2004. DOI: 10.1086/383178. arXiv: astro-ph/0309303.
- [12] R. Durrer, *Cosmology II: The CMB, dark matter and dark energy*, <https://indico.cern.ch/event/634061/attachments/1476161/2333296/lesson2.pdf>, (Accessed on 29/01/2023), Jul. 17.
- [13] ESA and the Planck Collaboration, *Power spectrum of temperature fluctuations in the cosmic microwave background*, <https://sci.esa.int/s/wRVmdjw>, (Accessed on 29/01/2023), Mar. 13.
- [14] C. Giuri, ‘VERITAS dark matter search in dwarf Spheroidal galaxies: an extended source analysis,’ *PoS*, vol. ICRC2021, p. 515, 2021. DOI: 10.22323/1.395.0515. arXiv: 2108.06083 [astro-ph.HE].

- [15] T. Miener, D. Nieto, V. Gammaldi, D. Kerszberg and J. Rico, ‘Combined search in dwarf spheroidal galaxies for branon dark matter annihilation signatures with the MAGIC Telescopes,’ Nov. 2022. arXiv: 2211.07979 [hep-ph].
- [16] M. Ackermann *et al.*, ‘Search for Gamma-ray Spectral Lines with the Fermi Large Area Telescope and Dark Matter Implications,’ *Phys. Rev. D*, vol. 88, p. 082002, 2013. DOI: 10.1103/PhysRevD.88.082002. arXiv: 1305.5597 [astro-ph.HE].
- [17] H. Abdalla *et al.*, ‘Search for Dark Matter Annihilation Signals in the H.E.S.S. Inner Galaxy Survey,’ *Phys. Rev. Lett.*, vol. 129, no. 11, p. 111101, 2022. DOI: 10.1103/PhysRevLett.129.111101. arXiv: 2207.10471 [astro-ph.HE].
- [18] N. Anđelić, S. Baressi Šegota, M. Glučina and Z. Car, ‘Estimation of Interaction Locations in Super Cryogenic Dark Matter Search Detectors Using Genetic Programming-Symbolic Regression Method,’ *Appl. Sciences*, vol. 13, no. 4, p. 2059, 2023. DOI: 10.3390/app13042059.
- [19] H. Kluck *et al.*, ‘Search for low-mass Dark Matter with the CRESST Experiment,’ in *13th Patras Workshop on Axions, WIMPs and WISPs*, 2018, pp. 130–133. DOI: 10.3204/DESY-PROC-2017-02/kluck_holger. arXiv: 1711.01285 [astro-ph.IM].
- [20] V. Iyer, ‘Large-Mass Single-Electron Resolution Detector for Dark Matter and Coherent Neutrino–Nucleus Elastic Interaction Searches,’ *Springer Proc. Phys.*, vol. 277, pp. 893–897, 2022. DOI: 10.1007/978-981-19-2354-8_160.
- [21] C. E. Aalseth *et al.*, ‘CoGeNT: A Search for Low-Mass Dark Matter using p-type Point Contact Germanium Detectors,’ *Phys. Rev. D*, vol. 88, p. 012002, 2013. DOI: 10.1103/PhysRevD.88.012002. arXiv: 1208.5737 [astro-ph.CO].
- [22] H. Lattaud, ‘Sub-GeV Dark Matter Searches with EDELWEISS: New results and prospects,’ in *14th International Workshop on the Identification of Dark Matter 2022*, Nov. 2022. arXiv: 2211.04176 [astro-ph.GA].
- [23] J. R. Angevaare, ‘First WIMP results of XENONnT and its signal reconstruction,’ Ph.D. dissertation, Amsterdam U., 2023.
- [24] N. Parveen, ‘The LUX-ZEPLIN dark matter experiment,’ *Astron. Nachr.*, vol. 342, no. 1-2, C. A. Zen Vasconcellos *et al.*, Eds., pp. 423–430, 2021. DOI: 10.1002/asna.202113945.
- [25] M. Kuźniak *et al.*, ‘Deap-3600 dark matter search,’ *Nuclear and Particle Physics Proceedings*, vol. 273-275, pp. 340–346, 2016, 37th International Conference on High Energy Physics (ICHEP), ISSN: 2405-6014. DOI: <https://doi.org/10.1016/j.nuclphysbps.2015.09.048>. [Online]. Available: <https://www.sciencedirect.com/science/article/pii/S2405601415005374>.
- [26] P. Agnes, ‘Direct Detection of Dark Matter with DarkSide-20k,’ *EPJ Web Conf.*, vol. 280, p. 06003, 2023. DOI: 10.1051/epjconf/202328006003.
- [27] R. Bernabei *et al.*, ‘Dark Matter: DAMA/LIBRA and its perspectives,’ in *14th International Workshop on the Identification of Dark Matter 2022*, Sep. 2022. arXiv: 2209.00882 [hep-ex].
- [28] I. Coarasa *et al.*, ‘ANAIS-112 sensitivity in the search for dark matter annual modulation,’ *Eur. Phys. J. C*, vol. 79, no. 3, p. 233, 2019. DOI: 10.1140/epjc/s10052-019-6733-4. arXiv: 1812.02000 [astro-ph.IM].
- [29] N. Iovine, ‘Dark matter searches in the centre of the Milky Way with IceCube,’ *PoS*, vol. ICHEP2022, p. 311, 2022. DOI: 10.22323/1.414.0311.
- [30] S. Giagu, ‘Wimp dark matter searches with the atlas detector at the lhc,’ *Frontiers in Physics*, vol. 7, 2019, ISSN: 2296-424X. DOI: 10.3389/fphy.2019.00075. [Online]. Available: <https://www.frontiersin.org/articles/10.3389/fphy.2019.00075>.
- [31] A. S. Chou *et al.*, ‘Snowmass Cosmic Frontier Report,’ in *2022 Snowmass Summer Study*, Nov. 2022. arXiv: 2211.09978 [hep-ex].

- [32] R. D. Peccei and H. R. Quinn, ‘Constraints imposed by CP conservation in the presence of pseudoparticles,’ *Phys. Rev. D*, vol. 16, pp. 1791–1797, 6 Sep. 1977. DOI: 10.1103/PhysRevD.16.1791. [Online]. Available: <https://link.aps.org/doi/10.1103/PhysRevD.16.1791>.
- [33] R. D. Peccei and H. R. Quinn, ‘CP Conservation in the presence of pseudoparticles,’ *Phys. Rev. Lett.*, vol. 38, pp. 1440–1443, 25 Jun. 1977. DOI: 10.1103/PhysRevLett.38.1440. [Online]. Available: <https://link.aps.org/doi/10.1103/PhysRevLett.38.1440>.
- [34] S. Weinberg, ‘A new light boson?’ *Phys. Rev. Lett.*, vol. 40, pp. 223–226, 4 Jan. 1978. DOI: 10.1103/PhysRevLett.40.223. [Online]. Available: <https://link.aps.org/doi/10.1103/PhysRevLett.40.223>.
- [35] F. Wilczek, ‘Problem of strong P and T invariance in the presence of instantons,’ *Phys. Rev. Lett.*, vol. 40, pp. 279–282, 5 Jan. 1978. DOI: 10.1103/PhysRevLett.40.279. [Online]. Available: <https://link.aps.org/doi/10.1103/PhysRevLett.40.279>.
- [36] A. Ringwald, ‘Axions and Axion-Like Particles,’ in *49th Rencontres de Moriond on Electroweak Interactions and Unified Theories*, 2014, pp. 223–230. arXiv: 1407.0546 [hep-ph].
- [37] D. J. Marsh, ‘Axion cosmology,’ *Physics Reports*, vol. 643, pp. 1–79, 2016, Axion cosmology, ISSN: 0370-1573. DOI: <https://doi.org/10.1016/j.physrep.2016.06.005>. [Online]. Available: <https://www.sciencedirect.com/science/article/pii/S0370157316301557>.
- [38] M. Narain *et al.*, ‘The Future of US Particle Physics - The Snowmass 2021 Energy Frontier Report,’ Nov. 2022. arXiv: 2211.11084 [hep-ex].
- [39] M. Fabbrichesi, E. Gabrielli and G. Lanfranchi, *The Dark Photon*. May 2020. DOI: 10.1007/978-3-030-62519-1. arXiv: 2005.01515 [hep-ph].
- [40] A. J. Krasznahorkay *et al.*, ‘Observation of Anomalous Internal Pair Creation in Be8 : A Possible Indication of a Light, Neutral Boson,’ *Phys. Rev. Lett.*, vol. 116, no. 4, p. 042501, 2016. DOI: 10.1103/PhysRevLett.116.042501. arXiv: 1504.01527 [nucl-ex].
- [41] J. L. Feng *et al.*, ‘Protophobic fifth-force interpretation of the observed anomaly in ^8Be nuclear transitions,’ *Phys. Rev. Lett.*, vol. 117, p. 071803, 7 Aug. 2016. DOI: 10.1103/PhysRevLett.117.071803. [Online]. Available: <https://link.aps.org/doi/10.1103/PhysRevLett.117.071803>.
- [42] A. J. Krasznahorkay *et al.*, ‘New results on the ^8Be anomaly,’ *J. Phys. Conf. Ser.*, vol. 1056, no. 1, p. 012028, 2018. DOI: 10.1088/1742-6596/1056/1/012028.
- [43] A. J. Krasznahorkay *et al.*, ‘New anomaly observed in ^4He supports the existence of the hypothetical x17 particle,’ *Phys. Rev. C*, vol. 104, p. 044003, 4 Oct. 2021. DOI: 10.1103/PhysRevC.104.044003. [Online]. Available: <https://link.aps.org/doi/10.1103/PhysRevC.104.044003>.
- [44] A. J. Krasznahorkay *et al.*, ‘New anomaly observed in ^{12}C supports the existence and the vector character of the hypothetical x17 boson,’ *Phys. Rev. C*, vol. 106, p. L061601, 6 Dec. 2022. DOI: 10.1103/PhysRevC.106.L061601. [Online]. Available: <https://link.aps.org/doi/10.1103/PhysRevC.106.L061601>.
- [45] N. J. Sas *et al.*, ‘Observation of the X17 anomaly in the $^7\text{Li}(p,e^+e^-)^8\text{Be}$ direct proton-capture reaction,’ May 2022. arXiv: 2205.07744 [nucl-ex].
- [46] D. S. M. Alves *et al.*, ‘Shedding light on X17: community report,’ *Eur. Phys. J. C*, vol. 83, no. 3, p. 230, 2023. DOI: 10.1140/epjc/s10052-023-11271-x.
- [47] C. Fruguele, E. Fuchs, G. Perez and M. Schlaffer, ‘Constraining New Physics Models with Isotope Shift Spectroscopy,’ *Phys. Rev. D*, vol. 96, no. 1, p. 015011, 2017. DOI: 10.1103/PhysRevD.96.015011. arXiv: 1602.04822 [hep-ph].
- [48] P. Ilten, Y. Soreq, M. Williams and W. Xue, ‘Serendipity in dark photon searches,’ *JHEP*, vol. 06, p. 004, 2018. DOI: 10.1007/JHEP06(2018)004. arXiv: 1801.04847 [hep-ph].

- [49] J. L. Feng *et al.*, ‘Particle physics models for the 17 meV anomaly in beryllium nuclear decays,’ *Phys. Rev. D*, vol. 95, p. 035017, 3 Feb. 2017. DOI: 10.1103/PhysRevD.95.035017. [Online]. Available: <https://link.aps.org/doi/10.1103/PhysRevD.95.035017>.
- [50] J. R. Batley *et al.*, ‘Search for the dark photon in π^0 decays,’ *Phys. Lett. B*, vol. 746, pp. 178–185, 2015. DOI: 10.1016/j.physletb.2015.04.068. arXiv: 1504.00607 [hep-ex].
- [51] N. C. Alexander Pukhov Alexander Belyaev, *Calchep*. [Online]. Available: <https://theory.sinp.msu.ru/~pukhov/calchep.html>.
- [52] *G4eionisation class reference*. [Online]. Available: <https://apc.u-paris.fr/~franco/g4doxy/html/classG4eIonisation.html>.
- [53] *G4eionisation standard libraries*. [Online]. Available: https://geant4.web.cern.ch/collaboration/working_groups/electromagnetic/.
- [54] *Geant4 livermore library*. [Online]. Available: <https://twiki.cern.ch/twiki/bin/view/Geant4/LoweMigratedLivermore>.
- [55] *Geant4 penelope library*. [Online]. Available: <https://geant4-userdoc.web.cern.ch/UsersGuides/PhysicsListGuide/html/electromagnetic/Pen.html>.
- [56] D. E. Cullen, S. T. Perkins and J. A. Rathkopf, ‘The 1989 livermore evaluated photon data library (epdl),’ Mar. 1990. DOI: 10.2172/6935054. [Online]. Available: <https://www.osti.gov/biblio/6935054>.
- [57] G. Cirrone, G. Cuttone, F. Di Rosa, L. Pandola, F. Romano and Q. Zhang, ‘Validation of the geant4 electromagnetic photon cross-sections for elements and compounds,’ *Nuclear Instruments and Methods in Physics Research Section A: Accelerators, Spectrometers, Detectors and Associated Equipment*, vol. 618, no. 1, pp. 315–322, 2010, ISSN: 0168-9002. DOI: <https://doi.org/10.1016/j.nima.2010.02.112>. [Online]. Available: <https://www.sciencedirect.com/science/article/pii/S0168900210003682>.
- [58] *Geant4 extended electromagnetic examples*. [Online]. Available: https://geant4.web.cern.ch/collaboration/working_groups/electromagnetic/examples.html.
- [59] C. M. Carloni Calame, G. Montagna, O. Nicrosini and F. Piccinini, ‘The BABAYAGA event generator,’ *Nucl. Phys. B Proc. Suppl.*, vol. 131, M. Incagli and G. Venanzoni, Eds., pp. 48–55, 2004. DOI: 10.1016/j.nuclphysbps.2004.02.008. arXiv: hep-ph/0312014.
- [60] C. M. Carloni Calame, C. Lunardini, G. Montagna, O. Nicrosini and F. Piccinini, ‘Large angle Bhabha scattering and luminosity at flavor factories,’ *Nucl. Phys. B*, vol. 584, pp. 459–479, 2000. DOI: 10.1016/S0550-3213(00)00356-4. arXiv: hep-ph/0003268.
- [61] M. N. Achasov and A. S. Kupich, ‘Separation of electrons and pions in the SND detector calorimeter,’ *Phys. Part. Nucl.*, vol. 49, no. 1, pp. 64–66, 2018. DOI: 10.1134/S1063779618010021.
- [62] M. Althoff *et al.*, ‘An Improved Measurement of Electroweak Couplings From $e^+e^- \rightarrow e^+e^-$ and $e^+e^- \rightarrow \mu^+\mu^-$,’ *Z. Phys. C*, vol. 22, p. 13, 1984. DOI: 10.1007/BF01577559.
- [63] F. Ambrosino *et al.*, ‘Measurement of the DAFNE luminosity with the KLOE detector using large angle Bhabha scattering,’ *Eur. Phys. J. C*, vol. 47, pp. 589–596, 2006. DOI: 10.1140/epjc/s2006-02617-4. arXiv: hep-ex/0604048.
- [64] B. Borgia *et al.*, ‘Test of quantum electrodynamics by Bhabha scattering in the GeV region,’ *Phys. Lett. B*, vol. 35, pp. 340–344, 1971. DOI: 10.1016/0370-2693(71)90274-7.
- [65] A. Scherdin, J. Reinhardt, W. Greiner and B. Muller, ‘Low energy e^+e^- scattering,’ *Reports on Progress in Physics*, vol. 54, no. 1, p. 1, Jan. 1991. DOI: 10.1088/0034-4885/54/1/001. [Online]. Available: <https://dx.doi.org/10.1088/0034-4885/54/1/001>.

- [66] A. Ashkin, L. A. Page and W. M. Woodward, ‘Electron-electron and positron-electron scattering measurements,’ *Phys. Rev.*, vol. 94, pp. 357–362, 2 Apr. 1954. DOI: 10.1103/PhysRev.94.357. [Online]. Available: <https://link.aps.org/doi/10.1103/PhysRev.94.357>.
- [67] K. Danzmann *et al.*, ‘180°-correlated equal-energy photons from 5.9-mev/nucleon u + th collisions,’ *Phys. Rev. Lett.*, vol. 59, pp. 1885–1888, 17 Oct. 1987. DOI: 10.1103/PhysRevLett.59.1885. [Online]. Available: <https://link.aps.org/doi/10.1103/PhysRevLett.59.1885>.
- [68] T. Cowan *et al.*, ‘Observation of correlated narrow-peak structures in positron and electron spectra from superheavy collision systems,’ *Phys. Rev. Lett.*, vol. 56, pp. 444–447, 5 Feb. 1986. DOI: 10.1103/PhysRevLett.56.444. [Online]. Available: <https://link.aps.org/doi/10.1103/PhysRevLett.56.444>.
- [69] T. Cowan *et al.*, ‘Anomalous positron peaks from supercritical collision systems,’ *Phys. Rev. Lett.*, vol. 54, pp. 1761–1764, 16 Apr. 1985. DOI: 10.1103/PhysRevLett.54.1761. [Online]. Available: <https://link.aps.org/doi/10.1103/PhysRevLett.54.1761>.
- [70] J. Schweppe *et al.*, ‘Observation of a peak structure in positron spectra from u+cm collisions,’ *Phys. Rev. Lett.*, vol. 51, pp. 2261–2264, 25 Dec. 1983. DOI: 10.1103/PhysRevLett.51.2261. [Online]. Available: <https://link.aps.org/doi/10.1103/PhysRevLett.51.2261>.
- [71] J. Reinhardt, A. Scherdin, B. Müller and W. Greiner, ‘Resonant bhabha scattering at MeV energies,’ *"Zeitschrift für Physik A Atomic Nuclei"*, vol. 327, no. 4, pp. 367–381, 1987.
- [72] E. Lorenz, G. Mageras, U. Stiegler and I. Huszar, ‘Search for Narrow Resonance Production in Bhabha Scattering at Center-of-mass Energies Near 1.8-MeV,’ *Phys. Lett. B*, vol. 214, pp. 10–13, 1988. DOI: 10.1016/0370-2693(88)90443-1.
- [73] H. Tsertos, C. Kozhuharov, P. Armbruster, P. Kienle, B. Krusche and K. Schreckenbach, ‘Sensitive search for neutral resonances around 1.8-MeV/c**2 in Bhabha scattering,’ *Phys. Lett. B*, vol. 207, pp. 273–277, 1988. DOI: 10.1016/0370-2693(88)90574-6.
- [74] J. v. Klinken, W. J. Meiring, F. W. N. d. Boer and S. J. Schaafsma, ‘Search for Resonant Bhabha Scattering around an Invariant Mass of 1.8 MeV,’ *Phys. Lett. B*, vol. 205, pp. 223–227, 1988. DOI: 10.1016/0370-2693(88)91654-1.
- [75] A. P. Mills and J. Levy, ‘Search for a Bhabha Scattering Resonance Near 1.8-MeV/c**2,’ *Phys. Rev. D*, vol. 36, pp. 707–712, 1987. DOI: 10.1103/PhysRevD.36.707.
- [76] S. D. Henderson *et al.*, ‘Search in s channel for production of 1-MeV/c**2 to 2-MeV/c**2 longlived e+ e- resonances,’ *Phys. Rev. Lett.*, vol. 69, pp. 1733–1736, 1992. DOI: 10.1103/PhysRevLett.69.1733.
- [77] X. Y. Wu *et al.*, ‘Search for low mass states in elastic e+ e- scattering,’ *Phys. Rev. Lett.*, vol. 69, pp. 1729–1732, 1992. DOI: 10.1103/PhysRevLett.69.1729.
- [78] A. L. Hallin, F. P. Calaprice, R. A. McPherson and E. R. J. Saettler, ‘Sensitive search for resonances in low-energy e+ e- scattering,’ *Phys. Rev. D*, vol. 45, pp. 3955–3960, 1992. DOI: 10.1103/PhysRevD.45.3955.
- [79] H. Tsertos, P. Kienle, S. M. Judge and K. Schreckenbach, ‘Experimental exclusion of neutral resonances in Bhabha scattering at MeV energies,’ *Phys. Lett. B*, vol. 266, pp. 259–263, 1991. DOI: 10.1016/0370-2693(91)91036-U.
- [80] S. M. Judge, B. Krusche, K. Schreckenbach, H. Tsertos and P. Kienle, ‘Search for Longlived Neutral Resonances in Bhabha Scattering Around 1.8-MeV/c²,’ *Phys. Rev. Lett.*, vol. 65, pp. 972–975, 1990. DOI: 10.1103/PhysRevLett.65.972.
- [81] J. Maddox, ‘Another red herring leads nowhere,’ *Nature*, vol. 339, no. 6222, pp. 253–253, 1989.

- [82] J. A. Poirier, D. M. Bernstein and J. Pine, ‘Scattering of 200-Mev Positrons by Electrons,’ *Phys. Rev.*, vol. 117, pp. 557–565, 2 Jan. 1960. DOI: 10.1103/PhysRev.117.557. [Online]. Available: <https://link.aps.org/doi/10.1103/PhysRev.117.557>.
- [83] M. Acciarri *et al.*, ‘Measurement of radiative Bhabha and quasireal Compton scattering,’ *Phys. Lett. B*, vol. 439, pp. 183–196, 1998. DOI: 10.1016/S0370-2693(98)01173-3.
- [84] I. C. Brock *et al.*, ‘Luminosity Measurement in the L3 Detector at LEP,’ *Nucl. Instrum. Meth. A*, vol. 381, pp. 236–266, 1996. DOI: 10.1016/S0168-9002(96)00734-6.
- [85] H. J. Behrend *et al.*, ‘A Search for substructure of leptons and quarks with the CELLO detector,’ *Z. Phys. C*, vol. 51, pp. 149–156, 1991. DOI: 10.1007/BF01475784.
- [86] I. Adachi *et al.*, ‘Measurement of the Processes $e^+e^- \rightarrow e^+e^-$ and $e^+e^- \rightarrow \gamma\gamma$ at $\sqrt{s} = 52$ -GeV,’ *Phys. Lett. B*, vol. 200, pp. 391–396, 1988. DOI: 10.1016/0370-2693(88)90793-9.
- [87] M. Raggi and V. Kozhuharov, ‘Proposal to Search for a Dark Photon in Positron on Target Collisions at DAΦNE Linac,’ *Adv. High Energy Phys.*, vol. 2014, p. 959 802, 2014. DOI: 10.1155/2014/959802. arXiv: 1403.3041 [physics.ins-det].
- [88] G. Mazzitelli, A. Ghigo, F. Sannibale, P. Valente and G. Vignola, ‘Commissioning of the daΦne beam test facility,’ *Nuclear Instruments and Methods in Physics Research Section A: Accelerators, Spectrometers, Detectors and Associated Equipment*, vol. 515, no. 3, pp. 524–542, 2003, ISSN: 0168-9002. DOI: <https://doi.org/10.1016/j.nima.2003.07.017>. [Online]. Available: <https://www.sciencedirect.com/science/article/pii/S0168900203023416>.
- [89] F. Bossi *et al.*, ‘The PADME beam line Monte Carlo simulation,’ *JHEP*, vol. 09, p. 233, 2022. DOI: 10.1007/JHEP09(2022)233. arXiv: 2204.05616 [hep-ex].
- [90] F. Oliva, ‘The PADME Active Diamond Target and Positron Bremsstrahlung Analysis,’ PhD Thesis, Università di Salento, 2020. [Online]. Available: http://www.le.infn.it/~chiodini/allow_listing/PhDThesis_FedericaOliva_FinalVersion.pdf.
- [91] P. Albicocco *et al.*, ‘Characterisation and performance of the PADME electromagnetic calorimeter,’ *Journal of Instrumentation*, vol. 15, no. 10, T10003–T10003, Oct. 2020. DOI: 10.1088/1748-0221/15/10/t10003. [Online]. Available: <https://doi.org/10.1088/1748-0221/15/10/t10003>.
- [92] A. Frankenthal *et al.*, ‘Characterization and performance of padme’s cherenkov-based small-angle calorimeter,’ *Nuclear Instruments and Methods in Physics Research Section A: Accelerators, Spectrometers, Detectors and Associated Equipment*, vol. 919, pp. 89–97, Mar. 2019, ISSN: 0168-9002. DOI: 10.1016/j.nima.2018.12.035. [Online]. Available: <http://dx.doi.org/10.1016/j.nima.2018.12.035>.
- [93] ‘The PADME Experiment Technical Proposal,’ *LNF Note INFN-16-15/LNF*,
- [94] A. J. Krasznahorkay *et al.*, ‘A new anomaly observed in ^4He supporting the existence of the hypothetical X17 particle,’ *J. Phys. Conf. Ser.*, vol. 1643, no. 1, p. 012 001, 2020. DOI: 10.1088/1742-6596/1643/1/012001.
- [95] P. Albicocco *et al.*, ‘Commissioning of the padme experiment with a positron beam,’ *Journal of Instrumentation*, vol. 17, 2022.
- [96] A. Krasznahorkai, *Status of experiments on 8be and 4he*, <https://agenda.infn.it/event/26303/contributions/135193/>, (Accessed on 30/01/2023), Sep. 21.
- [97] A. J. Krasznahorkay *et al.*, ‘New anomaly observed in C12 supports the existence and the vector character of the hypothetical X17 boson,’ *Phys. Rev. C*, vol. 106, no. 6, p. L061601, 2022. DOI: 10.1103/PhysRevC.106.L061601. arXiv: 2209.10795 [nucl-ex].
- [98] L. Darmé, M. Mancini, E. Nardi and M. Raggi, ‘Resonant search for the x17 boson at padme,’ *Phys. Rev. D*, vol. 106, p. 115 036, 11 Dec. 2022. DOI: 10.1103/PhysRevD.106.115036. [Online]. Available: <https://link.aps.org/doi/10.1103/PhysRevD.106.115036>.

- [99] *TSpectrum class reference*. [Online]. Available: <https://root.cern.ch/doc/master/classTSpectrum.html>.
- [100] V. I. Daren Sawkey, *G4mollerbhabhamodel*. [Online]. Available: <https://gitlab.cern.ch/geant4/geant4/-/blob/master/source/processes/electromagnetic/standard/src/G4MollerBhabhaModel.cc>.
- [101] *Fibers — crystals.saint-gobain.com*, <https://www.crystals.saint-gobain.com/radiation-detection-scintillators/fibers>, [Accessed 29-Jun-2023].
- [102] F. Bossi *et al.*, ‘Cross-section measurement of two-photon in-flight annihilation of positrons at $s=20$ MeV with the PADME detector,’ *Phys. Rev. D*, vol. 107, no. 1, p. 012008, 2023. DOI: 10.1103/PhysRevD.107.012008. arXiv: 2210.14603 [hep-ex].
- [103] I. Oceano, ‘Searching for the dark photon with padme and measurement of the $e^+e^- \rightarrow \gamma\gamma$ cross section at $\sqrt{s} = 21$ mev,’ PhD Thesis, Università di Salento, 2021. [Online]. Available: http://www.le.infn.it/~isabella/allow_listing/PhDThesisImage/mainThesis.pdf.
- [104] S. Bertelli *et al.*, ‘Status and Prospects of PADME,’ in *57th Rencontres de Moriond on Electroweak Interactions and Unified Theories*, May 2023. arXiv: 2305.08684 [hep-ex].